New Approaches to the Interpretation of 3D-Polarized Light Imaging Signals for an Advanced Extraction of Fiber Orientation

Julia Reckfort

Dissertation
zur Erlangung des Doktorgrades
(Dr. rer. nat.)

im Fachbereich C - Mathematik und
Naturwissenschaften an der Bergischen Universität
Wuppertal

30.03.2015

Die Dissertation kann wie folgt zitiert werden:

urn:nbn:de:hbz:468-20150826-120130-1
[http://nbn-resolving.de/urn/resolver.pl?urn=urn%3Anbn%3Ade%3Ahbz%3A468-20150826-120130-1]

Abstract

The neuroimaging technique 3D-polarized light imaging (3D-PLI) has opened up new avenues to study the complex nerve fiber architecture of the human brain at sub-millimeter spatial resolution. This polarimetry technique is applicable to histological sections of postmortem brains utilizing the birefringence of nerve fibers caused by the regular arrangement of lipids and proteins in the myelin sheaths surrounding axons. 3D-PLI provides a three-dimensional description of the anatomical wiring scheme defined by the in-section direction angle and the out-of-section inclination angle. To date, 3D-PLI is the only available method that allows bridging the microscopic and the macroscopic description of the fiber architecture of the human brain. In this thesis the possibility of a multiscale analysis of the architecture of single and bundles nerve fibers with 3D-PLI is established. The employed polarimetric setups are characterized and optimized, enabling further developments of the analysis of the data obtained with the setups. The influence of the system properties regarding the measured signals are compensated, realizing a multiscale analysis of the nerve fiber architecture. Further, a method to enable the tracing of fibers from the main fiber bundle to their terminal layer in the gray matter is provided. The introduced corrections of the signal interpretation are evaluated and compared to the results obtained with the standard analysis.

Kurzzusammenfassung

Die bildgebende Technik 3D-PLI, basierend auf polarisierten Licht, hat neue Wege zur Untersuchung der komplexen Nervenfaserarchitektur des menschlichen Gehirns im sub-Milimeter Bereich geebnet. Diese Technik ist unter Nutzung der doppelbrechenden Eigenschaften der Nervenfaserbahnen auf histologische Schnitte von postmortem Gehirnen anwendbar. Die doppelbrechenden Eigenschaften werden durch die regelmässige Anordnung von Lipiden und Proteinen in den faserumgebenden Myelinscheiden hervorgerufen. Mit Hilfe von 3D-PLI können die anatomischen Nervenfaserverbindungen durch einen Direktionswinkel in der Schnittebene und einem Steigungswinkel, der aus der Ebene herauszeigt, beschrieben werden. Bis heute ist 3D - PLI die einzige Methode, die den Brückenschlag zwischen der mikroskopischen und makroskopischen Beschreibung der Faserarchitektur des menschlichen Gehirns ermöglicht.
In dieser Arbeit wird die Möglichkeit einer Multiskalenanalyse von einzelnen und gebündelten Nervenfasern mit Hilfe von 3D PLI etabliert. Die verwendeten polarimetrischen Aufbauten werden charakterisiert, optimiert und der Einfluss der Systemeigenschaften auf die gemessenen Signale untersucht. Die Kompensation dieser Einflsse ermöglicht die Realisierung einer Multiskalenanalyse der Nervenfaserarchitektur. Ferner wird ein Zusammenhang zwischen dem Myelingehalt und dem Transmittanzsignal untersucht und die Standardanalyse um diesen erweitert. Dies ermöglicht eine simultane Detektion von Nervenfasern in der weien und grauen Substanz. Die vorgestellten Korrekturen der Signalinterpretation werden beurteilt und mit den Ergebnissen, die man mit der aktuellen Standardanalyse erhält verglichen.

Contents

Chapter 1

Introduction

Decoding the human brain is the major challenge addressed by neuroscientists around the world. Within the last two decades, large initatives such as the Human Brain Project in Europe [1] and the BRAIN Initiative (Brain Research through Advancing Innovative Neurotechnologies) [2] in the USA were launched. The decoding of the human brain offers the possibility to infer new diagnostics and treatments for brain disorders such as Alzheimer's disease, Parkisons's disease or Schizophrenia. Research results are based on structural and functional high resolution studies. The knowledge about the structure of the brain might aid to develop new, highly efficient computer architectures depicting basic principles of the human brain organization [1]. If seeking to understand the function of the human brain, it is indispensable to study its underlying structure, i.e. , the organization of neurons and their intricate connections. These connections are provided by means of association, commissural and projection fiber tracts. The association tracts span from a few micrometer (short range) to several hundred millimeter (long range) and connect different areas within the same brain hemisphere. The commiussural tracts are long-ranged, connecting areas of the two hemispheres. The either long- or short-range projection fibers connect the cortex with subcortical regions [3].
The investigation of the fiber architecture poses specific challenges that have been tackled by various imaging techniques developed over the last decades. The exploration of the nerve fiber architecture of the human brain is a multiscale challenge as the size of the structures range a few nanometer for neurofilaments to several centimeters for long range inter-hemispheric con-

nections (cp. Fig. 1.1). Furthermore, the fibers originate and terminate in the gray matter regions of the brain. The density of the fibers decreases significantly over a distance of 2 - 4 mm towards the brain surface [4]. The variation of the fiber density is especially challenging for neuroimaging techniques where the fiber density directly or indirectly influences the strength of the measured signal. Thus, it is difficult to trace the course of fibers from their points of origin to their terminal axons. Another challenging aspect is the spatial arrangement of fibers. The crossing and intermingling of fibers complicate the evaluation of nerve fiber orientation for imaging techniques providing a coarser resolution than $1\mu m$ (diameter of a nerve fiber). Multiple fiber orientations measured in a single volume element (voxel) can hardly be differentiated in this case.

To investigate the nerve fiber connections, several imaging techniques, such as electron microscopy, dissection, light microscopy and techniques based on magnetic resonance (MR) were developed. Each technique covers a different scale of the nerve fiber architecture, i.e. from single fibers via small fiber networks to fiber pathways composed of thousands of fibers (Fig. 1.1). This

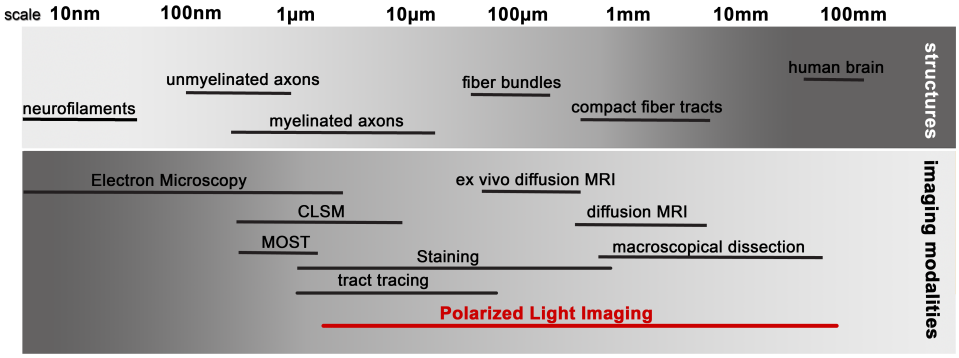

Figure 1.1: The structures of the human brain range from a few nanometer to several centimeter. A broad variety of imaging techniques exist to cover this range. (CLSM - Confocal Laser Scanning Microscopy, MRI - Magnetic Resonance tomography, MOST - Micro-Optical Sectioning Tomography).

thesis focuses on the challenges the investigation of the fiber architecture poses to 3D Polarized Light Imaging (3D-PLI), a neuroimaging technique based on polarimetric principles applied to postmortem brain tissue.

Employing electron microscopy, cell structures below 1 µm can be resolved, enabling the visualization of single axons [5]. It is also possible to visualize single axons with confocal laser scanning microscopy (CLSM) [6] or

micro-optical sectioning tomography (MOST) [7]. The traditional method for investigating the nerve fiber architecture is the staining of histological sections. The stained sections are imaged with microscopes, resulting in a slightly coarser resolution than electron microscopy, but enabling the mapping of single nerve fibers and fiber bundles [8, 9]. The staining procedure relies on the accumulation of dye particles in the myelin sheaths that surround the nerve fibers. It is only possible to visualize the presence and differences in densities of fiber and it is not possible to reconstruct the 3D orientation of nerve fibers in the brain.

Another microscopical technique to investigate the fiber architecture in postmortem brains is tract tracing. It is a reliable method to map the course of individual fiber tracts. For this purpose, tracers are injected into the brain and transported through the fibers [10]. The tracers are best transported in the living brain, but have to be investigated post-mortem. This technique is therefore not applicable to humans. Furthermore, only short range connections can be mapped due to the slow transport mechanism of the tracers opposing the long range of fibers [11, 12].

Dissection [13] or MR based techniques [14, 15] are used to investigate the fiber architecture as they allow the observation of major fiber tracts. Employing these methods, the major fiber tracts are observed [16, 17]. Klinger introduced the dissection method, which is based on the freezing and controlled breaking of the brains along the major fiber tracts [13]. Clearly, the dissection of fiber tracts in one brain only enables the investigation of a limited number of fiber tracts.

Most methods are only applicable to postmortem tissue. To date, diffusion MRI (dMRI) is the only technique available for the assessment of nerve fibers in vivo [18]. It is based on the observation that the diffusion of water molecules is restricted by macroscopical structures such as nerve fibers. Due to the pulsing of the brain higher resolutions for in vivo studies are not feasible. However, higher resolutions can be achieved in postmortem studies with higher magnetic fields and longer scanning times [19] than the resolution possible in vivo.

Each of the mentioned techniques has specific strengths and benefits, but also limitations. Data volume and measurement time increase substantially with increase in resolution. More critical is the limited feasibility of microscopical techniques for large volumes. For example, employing an electron

microscope enables the imaging of single axons, but imaging all axons of a human brain is not possible. In contrast, with dMRI it is possible to image the main fiber bundles in a human brain within a few minutes, but only with a coarse resolution compared to the diameter of a single fiber.
3D-PLI offers the possibility to investigate the fiber tracts micro- and mesoscopically, depending on the chosen optical setup. It is possible to map fiber pathways including fiber bundles as well as single nerve fibers in human post-mortem brains. This investigation of the organization of the brain across multiple scales will be referred to as "multiscale approach". Due to this the gap between the highly resolved microscopical techniques and the coarse resolution obtainable with dMRI can be closed. The possibility to investigate nerve fibers by means of polarimetry is known for almost a century [20–23]. But only the recent technological progress has enabled the systematic investigation of the 3D orientation of nerve fibers. 3D-PLI has the potential to overcome the multiscale challenge, which has its origin in the complexity of the nerve fiber architecture, and to enable the tracing of nerve fibers from the gray into the white matter.

In our laboratory, two different polarimetric setups exist to tackle the task of imaging the nerve fiber architecture on different scales. The large-area polarimeter (LAP) is an in-house development that enables the investigation of long range connections and large fiber bundles. In contrast, the so-called polarizing microscope (PM) was custom-build for high resolved imaging of brain fibers. Both setups are complementary, state-of-the-art polarimeters based on 3D-PLI. Even though they share a similar basic setup, the measured fiber orientations are not immediately comparable, preventing any multiscale attempt. The systems are expected to differ in their system properties, resulting in different system responses to the same sample. Thus, characterization and optimization of the setups are crucial. Furthermore, the knowledge gained has to be used to compensate for the influence of the system properties on the measurements.
This presented work aims to enable the investigation of the nerve fiber architecture with 3D-PLI on different scales as well as the tracing of fibers to their terminals. First, the basic principles and analysis concepts of 3D-PLI are introduced in Chapter 2. In order to pursue the exploration of the nerve fiber architecture across different scales, the comparability of the mea-

surements obtained with the LAP and the PM must be ensured. For this purpose, both systems are thoroughly characterized and optimized. The crucial system properties such as the illumination, polarization effects, image resolution and systems sensitivities are measured and analyzed. The knowledge gained about the differences are used to derive correction factors to compensate for the influence of the differing system properties. The necessity and validity of the correction factors are assessed in Chapter 4. In Chapter 5, the possibility to employ the information of the transmitted light to solve the signal ambiguity of fiber density and orientation is explored. In the final Chapter 6, a conclusion and outlook is given. The progress that this work has achieved is emphasized and the challenges for the future are discussed.

Chapter 2

Basics of 3D Polarized Light Imaging

Understanding the fundamental principles of birefringence is important to grasp the idea of 3D-PLI. This imaging method is based on the interaction of polarized light with brain tissue, more specifically with the birefringent myelin sheaths surrounding the nerve fibers. Within this chapter, the relevant optical properties of brain tissue are introduced and then the tissue preparation and the image acquisition procedure are explained. Subsequently, the physical background to understand the analysis of 3D-PLI is provided and the calculation of the nerve fiber orientation on the basis of the described measurement is derived.

2.1 Optical Properties of Brain Tissue

The brain consists mostly of nerve cells (neurons) which are connected through nerve fibers (axons, dendrites, and synapses) as shown in Figure 2.1 B. The nerve cells process and transmit information, while the nerve fibers conduct information in form of electrical impulses from one nerve cell to the other. Most fibers are surrounded by a myelin sheath, which is an insulating layer composed of lipid bilayers that enables a fast conduction speed of electrico-chemical impulses. The myelin sheaths are tightly packed, multilayered stacks of cell membranes which are wrapped around the axon up to 160 times (see Fig. 2.1 C) [24]. The myelinated nerve fibers, which constitute the white matter in the brain appear bright in backscattered imaging

due to the strongly scattering lipid content of the myelin. In contrast, the cell bodies accumulated in the gray matter appear dark. The gray matter surrounds in most cases the white matter as can be seen in Figure 2.1 A.

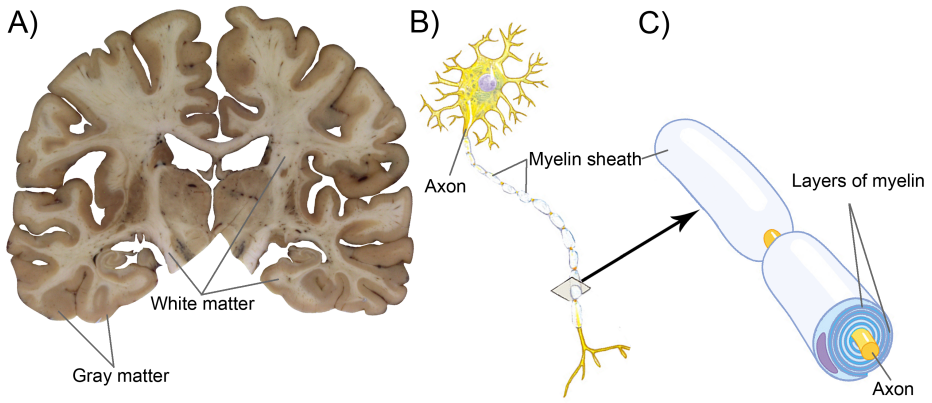

Figure 2.1: Cross section of a human brain and schematic nerve fibers. (A) Backscattered image of a sectioned brain highlighting the gray and white matter. The nerve fibers (B) constituting the white matter are wrapped with layers of myelin (C) (after Campbell-Reece [25] p. 1227).

Gray and white matter differ in terms of their optical properties due to their diverging composition. Several studies have been reported, which investigated the scattering coefficient, the absorption coefficient, and the anisotropy factor of human brain structures [26–33]. However, for this thesis only the birefringence and the attenuation of light is relevant.

Birefringence. The myelin components (70-85 % lipids, 15-30 % proteins [34]) are responsible for the strong birefringence and for the light attenuation of brain tissue. Apart from the myelin sheaths, microtubuli and neurofilaments are also considered as being birefringent [35]. Their contribution, however, is minimal compared to the birefringence of the myelin sheaths and can therefore be neglected for the presented studies [36]. The alignment and packing of the lipid molecules and proteins cause negative birefringence and a weak positive form birefringence, respectively [23, 34] (for more detail see Sec. 2.4.1). The observed compound birefringence is a negative uniaxial birefringence as the intrinsic birefringence is dominant [37]. The physical fundamentals on birefringence are briefly explained in Section 2.4.1.

Light attenuation. The term light attenuation describes the attenuation of incident light by scattering effects which includes reflection and absorption. Literature values for the attenuation of light in brain tissue differ significantly as the conducted studies are based on differing tissue preparations and varying measuring techniques. However, all studies state consistently that white matter has a higher attenuation coefficient than gray matter. The higher attenuation of light is caused by the scattering properties of myelin [26, 30, 32, 33].

2.2 Tissue Preparation

3D-PLI is based on measurements of transmitted light. Consequently, the brain has to be cut into thin sections. Beforehand the brain tissue needs to be carefully prepared. To minimize the degeneration of the myelin sheaths, the brain has to be removed from the skull within the first 12 h after death and is then placed into a 4 % solution of buffered formaldehyde. Depending on the size of the brain, it is fixated up to six months in order to prevent decay and to provide tissue stability. Furthermore, the brain is immersed in a 20 % solution of glycerin with Dimethyl sulfoxide (DMSO) to prevent the formation of ice crystals during the freezing process. The brain is frozen down to −80 °C and sectioned with a large-scale cryostat microtome (Polycut CM 3500, Leica, Germany) (Fig. 2.2 A). In-house studies proved a section thickness between 50 µm and 100 µm to be optimal for 3D-PLI measurements. Thinner sections become unstable and complicated in handling [38]. Larger

section thicknesses lead to an ambiguity of the measured signal due to the periodic nature of birefringent measurements [39]. During the cutting procedure, a (so-called blockface) image of the surface of the brain is captured to enable a registration of the cut sections which is necessary to provide a 3D-reconstruction of the tissue (Fig. 2.2 B) [40]. Each section is mounted on a glass slide, embedded in a glycerin solution, covered with a thin glass sheet, and sealed with lacquer.
Depending on the size of the brain, the cutting direction, and the slice thickness the total amount of sections usually varies between 1500 and 3000 for a whole human brain (Fig. 2.2 C).

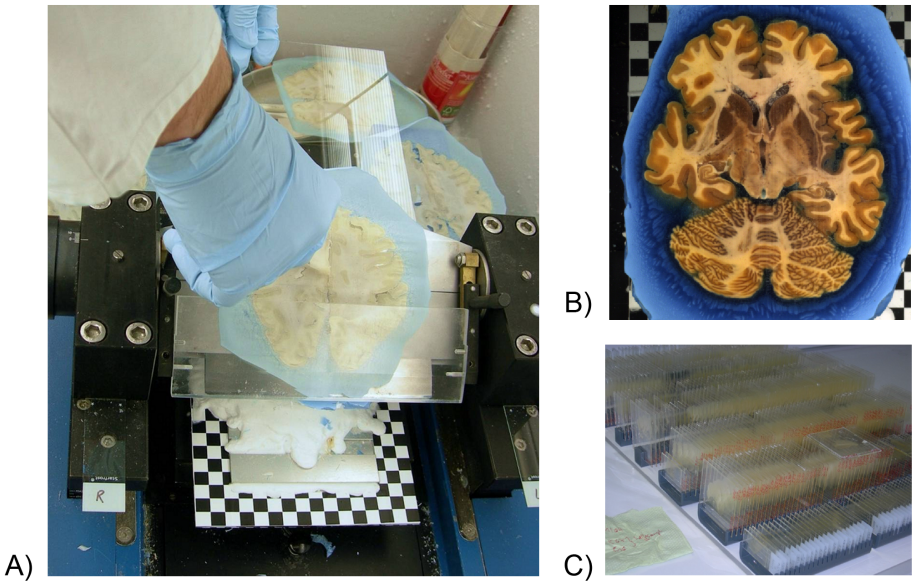

Figure 2.2: Illustration of the tissue preparation. A) The brain is sectioned with a cryostat microtome. B) During the sectioning process, an image of the surface of the frozen block (blockface image) is captured. C) Series of mounted brain sections.

2.3 Image Acquisition

3D-PLI represents an advancement of a technique that has already been described by Wood and Glazer in 1980 [41, 42]. Currently, two different polarimetric setups are used in our laboratory. The systems differ slightly in the arrangements of the components, but in both cases a pair of crossed linear polarizers and a quarter-wave retarder are implemented. For reasons

of simplicity, within this chapter the description and calculations will be exemplary conducted for the LAP. The description and calculation of the PM are equivalent and can be found in Appendix A.1. The exact setup of the LAP is depicted in Figure 2.3. Further details about the two employed polarimeters are described in Chapter 3. For the measurements regarding the orientation of nerve fibers in a given brain section, all three filters are rotated simultaneously. The filters are rotated in 10 °-steps from 0 ° to 170 °. At every filter position an image is captured. The subsequent analysis is performed pixelwise.

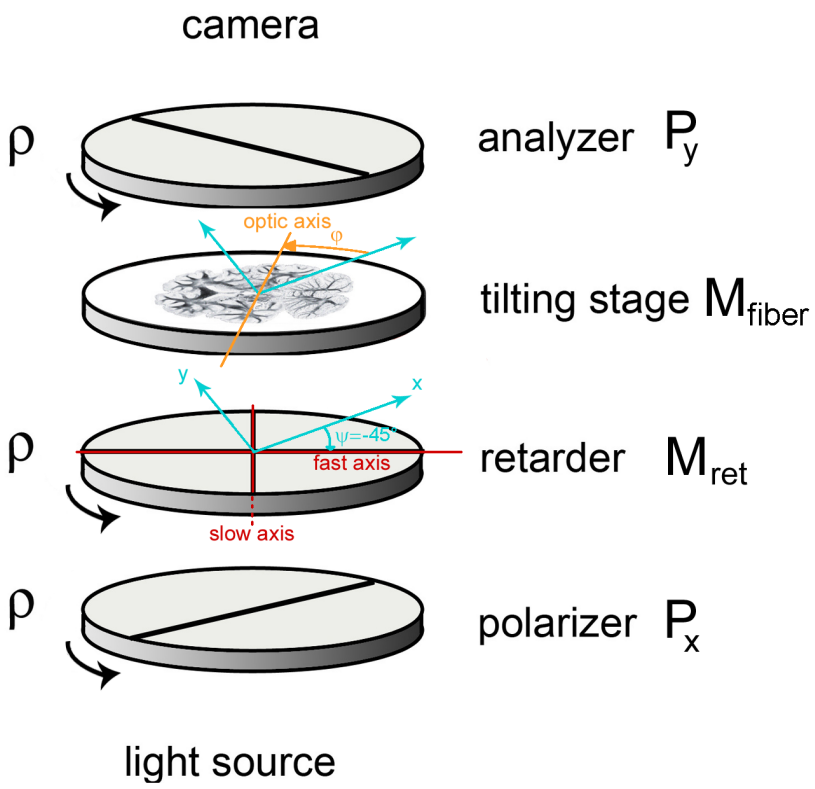

Figure 2.3: Polarimetric setup. The polarizer (P_y) and retarder (M_{ret}) enable the illumination of the tissue (M_{fiber}) with light that has a defined state of polarization. The fast axis of the quarter-wave retarder is oriented at $\psi = -45\,^\circ$ with respect to the first linear polarizer P_x. The induced change of the polarization state by the brain tissue is analyzed by rotating the linear analyzer. The brain tissue is described as an uniaxial birefringent medium with a single optic axis with in-plane direction angle φ. All filters are rotated by the rotation angle ρ.

By analyzing the output polarization state with the rotating analyzer, it is possible to measure the nerve fiber orientation.

2.4 Standard 3D-PLI Analysis

3D-PLI is able to distinguish different states of polarization and draw inferences from them about the local nerve fiber orientation. The standard 3D-PLI analysis is based on the Jones matrix formalism and Fourier analysis (for more detail see Sec. 2.4.2 - 2.4.4). For the theoretical description, the Jones matrix formalism is preferred over the Mueller calculus [43] in accordance with other literature [39, 44, 45]. It is possible to employ the Jones matrix formalism as fully polarized light is used [39].

2.4.1 Polarization Effects

Light can be described as an electromagnetic wave consisting of an electric ($\vec{E}$) and a magnetic ($\vec{M}$) field component that oscillate perpendicular to each other. If isotropic, homogeneous, non-attenuating media are investigated, $\vec{E}$ and $\vec{M}$ will be perpendicular to the wave's direction of propagation. In the following, it is assumed that $\vec{E}$ and $\vec{M}$ oscillate in the x-y-plane and that the light propagates in the z-direction. When describing the polarization state of light, only the electric field vector is considered. For a planar monochromatic wave propagating in z-direction and depending on the time τ, the electric field vector is given by [46]:

$$\vec{E}(z,\tau) = \vec{E_0} \cdot e^{i(kz-\omega\tau+\phi)} \tag{2.1}$$

with $k = 2\pi/\lambda$ and $\omega = 2\pi v/\lambda$.
Here $\vec{E_0}$ is the original electric field vector, k the magnitude of the wave vector, λ the wavelength of the light, ω the angular frequency, v the phase velocity, and ϕ is the phase.

Polarization states. In general, light is considered as being polarized when the electric field vector oscillates in a lawful manner. Depending on the shape that the electric field vector describes in the x-y-plane, the following three states of polarization are discriminated:

- *Linear polarization*: The electric field vector $\vec{E}$ points at all times in the same direction and the two components E_x and E_y oscillate in phase ($\Delta\phi = 0, \pm\pi, \pm 2\pi, \ldots$).
- *Circular polarization*: The electric field vector $\vec{E}$ describes a circle

in the x-y-plane. The amplitude of the two components are equal ($E_x = E_y = |\vec{E}|/\sqrt{2}$) and the phase differs by $\Delta\phi = \frac{\pi}{2} + m \cdot \pi$ (with $m \in \mathbb{N}_o$).
Depending on the direction of rotation it is distinguished between right- and left-handed circular polarization.

- *elliptical polarization*: The electric field vector $\vec{E}$ describes an ellipse in the x-y-plane with $E_x \neq E_y$ or $\Delta\phi \neq \frac{\pi}{2}, \neq m \cdot \pi$ (with $m \in \mathbb{N}_o$).

Birefringence. A birefringent material is optically anisotropic, i. e. the refractive index depends on the state of polarization and on the direction of propagation of the light. The relative permittivity of an anisotropic medium can be described by $\tilde{\epsilon_r}$:

$$\tilde{\epsilon_r} = \begin{pmatrix} \epsilon_{11} & \epsilon_{12} & \epsilon_{13} \\ \epsilon_{21} & \epsilon_{22} & \epsilon_{23} \\ \epsilon_{31} & \epsilon_{32} & \epsilon_{33} \end{pmatrix}.$$

If an appropriate coordinate system is chosen, the tensor $\tilde{\epsilon_r}$ can be written in diagonal form:

$$\tilde{\epsilon_r}' = \begin{pmatrix} \epsilon_{r,1} & 0 & 0 \\ 0 & \epsilon_{r,2} & 0 \\ 0 & 0 & \epsilon_{r,3} \end{pmatrix},$$

with $n_i = \sqrt{\mu_r \cdot \epsilon_{r,i}}$ being the refractive indices along the principal axes, which depend on the relative permeability μ_r and the relative permittivity ϵ_r.
The transformation to principal axes yields:

$$\frac{n_x^2}{n_1^2} + \frac{n_y^2}{n_2^2} + \frac{n_z^2}{n_3^2} = 1. \tag{2.2}$$

Two different types of birefringence can be distinguished. If the length of all three principal axes are different ($n_1 \neq n_2 \neq n_3$), the material is called biaxial birefringent. In contrast, if two of the principal axes have the same length and the third differs ($n_1 = n_2 \neq n_3$), the material is called uniaxial birefringent.
Nerve fibers are considered to be uniaxial birefringent and are described by a refractive index ellipsoid (indicatrix) with two axes of the same length

($n_1 = n_2 = n_o$) and one axis of a different length ($n_3 = n_e$) [20, 21] (cf. Fig. 2.4). The birefringence of a material is defined as the difference between the refractive index of the ordinary wave n_o and the refractive index of the extraordinary wave n_e: $\Delta n \equiv n_e - n_o$. Depending on the relation of the refractive indices, the material is either positive uniaxial birefringent ($\Delta n > 0$) or negative uniaxial birefringent ($\Delta n < 0$).
In case of a uniaxial birefringent medium, the refractive index ellipsoid can be described by a rotational ellipsoid (see Fig. 2.4), which is a model to depict the interaction of light with a uniaxial birefringent medium. In case of the rotational ellipsoid, the optic axis corresponds to the extraordinary refractive index $n_e(\theta = 90\,^\circ)$.

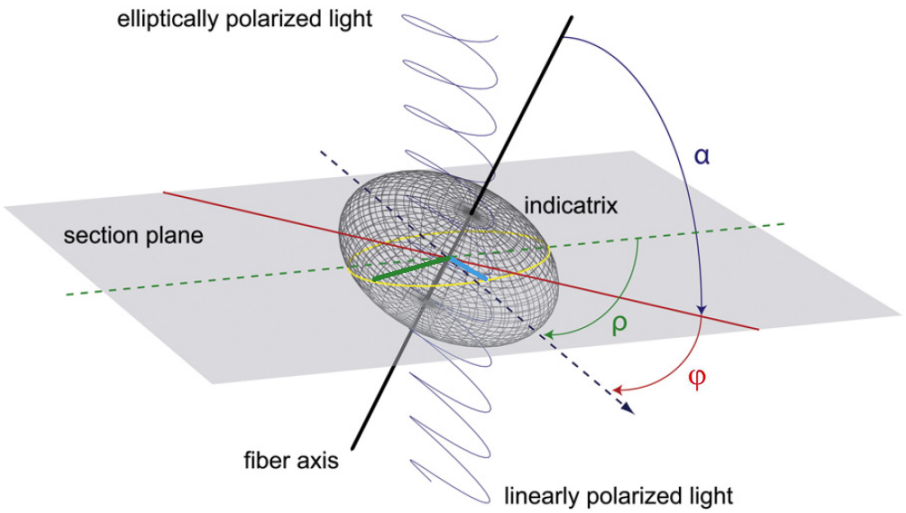

Figure 2.4: Indicatrix of an ideal nerve fiber. It represents the visualization of the employed optical fiber model. The fiber orientation coincides with the main axis of the ellipsoid. The ellipsoid is characterized by two different principal indices (green, cyan). Due to the heterogeneous refractive index (yellow ellipse), the incident light is split into two rays which propagate at different velocities, inducing a phase shift between them. The fiber orientation is described by the in-section direction angle φ and the out-of-section inclination angle α. The angle $-\rho$ describes the mathematical rotation of the tissue.

When light passes through brain tissue, it is split into two waves with orthogonal linear polarization states, the ordinary and extraordinary wave. The green and light blue line in Fig. 2.4, indicate the refractive index of the medium for the ordinary and extraordinary wave. The ordinary wave propagates in direction of the principal axis and perpendicular to the op-

tic axis of the material, where the velocity is independent of the direction of propagation. It obeys Snell's law of refraction for isotropic media. The extraordinary wave oscillates parallel to the optic axis and experiences a different refractive index.
Due to the different refractive indices, both waves have different velocities, leading to a phase shift between them. The phase shift of the extraordinary wave with respect to the ordinary wave, also referred to as optical retardation, depends on the thickness of the medium t, the light wavelength λ and the incidence angle θ:

$$\Delta\phi(\theta) = \phi_e(\theta) - \phi_o = \frac{2\pi t}{\lambda}(n_e(\theta) - n_o), \tag{2.3}$$

with

$$n_e(\theta) = \frac{1}{\sqrt{\frac{\cos^2(\theta)}{n_o^2} + \frac{\sin^2(\theta)}{n_E^2}}}.$$

The angle θ is defined as the angle between the wave vector $\vec{k}$ and the optic axis of the medium and n_E corresponds to the extraordinary refractive index for $\theta = 90°$.
As shown by Larsen et al. [44] $n_e(\theta) - n_o$ can be approximated by:

$$n_e(\theta) - n_o \sim \Delta n \cdot \cos^2(\theta).$$

And with $\alpha = 90° - \theta$ Equation (2.3) can be expressed as:

$$\Delta\phi \sim \frac{2\pi t}{\lambda}\Delta n \cos^2(\alpha). \tag{2.4}$$

Thus, when light passes through brain tissue the extraordinary wave is retarded and experiences a phase shift with respect to the ordinary wave, depending on the material thickness t, the incident wavelength λ, the difference of refractive indices Δn, and the fiber inclination angle α. If the light passes parallel to the optic axis, the light will not be split up or retarded and the original state of polarization will be preserved. The phase shift that the extraordinary ray experiences depends on the angle between the principal axis and the optic axis of the material. The induced phase shift and the composition of amplitudes are influenced by the spatial orientation of the fiber with respect to the direction of the electric field vector of the light.

The fiber orientation is described by the in-plane direction angle φ and the out-of-section inclination angle α.

2.4.2 Introduction of the Jones Calculus

For 3D-PLI a set of linear polarizers and a wave retarder are employed. The optical setup can be described using the Jones matrix formalism [44,47,48]. The Jones matrix formalism represents an elegant method to describe the polarization states of light as well as the optical elements influencing them [47]. The Jones formalism uses the mathematical description of the phase and the amplitude of the light wave and assumes that the light is completely polarized. The polarization state of light is represented by a 2×1-vector (Jones vector) and the optical elements by 2×2-matrices (Jones matrices). The Jones vector only describes completely polarized light and is defined as:

$$\vec{J} = \frac{1}{|\vec{E}|} \cdot \begin{pmatrix} E_x e^{i\phi_x} \\ E_y e^{i\phi_y} \end{pmatrix},$$

where E_x and E_y are the amplitudes and ϕ_x and ϕ_y are the phases of the x- and y-component, respectively. The sum of the squares of the absolute values of the two components of the Jones vector is proportional to the light intensity: $I \sim E_x E_x^* + E_y E_y^*$.
The Jones vector of linearly polarized light is given by:

$$\begin{pmatrix} \cos(\psi) \\ \sin(\psi) \end{pmatrix},$$

where ψ is the angle between the polarization vector $\vec{E}$ and the x-axis. The angle ψ is defined in the counter-clockwise direction.
The linear polarizers convert unpolarized light into linearly polarized light. Only electric field vectors oscillating in a certain direction (corresponding to the axis of the polarizer) are transmitted. The Jones matrices for an ideal linear horizontal polarizer (P_x) and an ideal linear vertical polarizer (P_y) are given by:

$$P_x = \begin{pmatrix} 1 & 0 \\ 0 & 0 \end{pmatrix}, \tag{2.5}$$

$$P_y = \begin{pmatrix} 0 & 0 \\ 0 & 1 \end{pmatrix}. \tag{2.6}$$

The employed wave retarder is uniaxial birefringent and introduces a phase shift between the ordinary and extraordinary ray, changing the state of polarization. The induced phase shift (or retardance of the extraordinary ray) depends on the material thickness t, the light wavelength λ and the refractive indices of the filter Δn:

$$\delta = \frac{2\pi}{\lambda}\Delta n t. \tag{2.7}$$

For wave retarders a particular wave retardance $\gamma = \delta/2$ is specified for a certain wavelength. A wave retarder which introduces a phase shift $\delta/2$ along the fast axis (=x-axis) and $-\delta/2$ along the slow axis (=y-axis) can be described by the following Jones matrix:

$$M_{\mathrm{ret}}(\delta) = \begin{pmatrix} e^{\mathrm{i}\frac{\delta}{2}} & 0 \\ 0 & e^{-\mathrm{i}\frac{\delta}{2}} \end{pmatrix}. \tag{2.8}$$

A rotation in counter-clockwise direction by an angle ψ is described by the rotation matrix:

$$R(\psi) = \begin{pmatrix} \cos(\psi) & -\sin(\psi) \\ \sin(\psi) & \cos(\psi) \end{pmatrix} \tag{2.9}$$

2.4.3 Application of the Jones Calculus

The used employed polarimetric setups differ slightly in their arrangement of the optical components. However, due to the reversibility of the optical path the theoretical mathematical descriptions using the Jones matrix formalism yields the same results. Within this section the Jones matrix formalism will be employed to describe the setup of the large-area polarimeter. The theoretical description employing the Jones matrix formalism for the PM is given in Appendix A.1.

As described in Section 2.3, the standard setup consists of a pair of crossed linear polarizers (P_x and P_y) and a quarter-wave retarder ($\mathrm{M}_{\mathrm{ret}}(\pi/2)$). The fast axis of the quarter-wave retarder is rotated by $\psi = -45°$ with respect to the axis of the first linear polarizer (see Fig. 2.3).

The quarter-wave retarder with $\delta = \pi/2$ and $\psi = -\pi/4$ is described by:

$$\begin{aligned} M'_{\text{ret}}(\delta = \pi/2, \psi = -\pi/4) &\overset{(2.8),(2.9)}{=} R(-\pi/4) \cdot M_{\text{ret}}(\pi/2) \cdot R(\pi/4) \\ &= \begin{pmatrix} \cos(-\pi/4) & -\sin(-\pi/4) \\ \sin(-\pi/4) & \cos(-\pi/4) \end{pmatrix} \cdot \begin{pmatrix} e^{\mathrm{i}\frac{\pi}{4}} & 0 \\ 0 & e^{-\mathrm{i}\frac{\pi}{4}} \end{pmatrix} \cdot \begin{pmatrix} \cos(\pi/4) & -\sin(\pi/4) \\ \sin(\pi/4) & \cos(\pi/4) \end{pmatrix} \\ &= \frac{1}{\sqrt{2}} \begin{pmatrix} 1 & -\mathrm{i} \\ -\mathrm{i} & 1 \end{pmatrix}. \end{aligned} \tag{2.10}$$

When employing the Jones calculus to analyze the 3D-PLI signal, the brain tissue can be described as a single wave retarder [44]. The fast axis is defined to be in direction of the optic axis of the fiber. Thus, the tissue can be described by: $M_{\text{fiber}}(\varphi) = R(\varphi) \cdot M_{\text{ret}}(\delta) \cdot R(-\varphi)$.
The simultaneous rotation of all implemented polarization filters with the rotation angle ρ with respect to the in-plane fiber direction φ is mathematically equivalent to a rotation of the tissue in the opposite direction $(-\rho)$, while keeping the polarization filters fixed. Therefore, the rotation of the tissue is described by $\beta = \varphi - \rho$:

$$\begin{aligned} M_{\text{fiber}}(\delta, \beta) &\overset{(2.8),(2.9)}{=} R(\beta) \cdot M_{\text{ret}}(\delta) \cdot R(-\beta) \\ &= \begin{pmatrix} \cos(\beta) & -\sin(\beta) \\ \sin(\beta) & \cos(\beta) \end{pmatrix} \cdot \begin{pmatrix} e^{\frac{i}{2}\delta} & 0 \\ 0 & e^{-\frac{i}{2}\delta} \end{pmatrix} \cdot \begin{pmatrix} \cos(\beta) & \sin(\beta) \\ -\sin(\beta) & \cos(\beta) \end{pmatrix} \\ &= \begin{pmatrix} \cos(\frac{\delta}{2}) + \mathrm{i}\sin(\frac{\delta}{2})\cos(2\beta) & \mathrm{i}\sin(\frac{\delta}{2})\sin(2\beta) \\ \mathrm{i}\sin(\frac{\delta}{2})\sin(2\beta) & \cos(\frac{\delta}{2}) - \mathrm{i}\sin(\frac{\delta}{2})\cos(2\beta) \end{pmatrix} \end{aligned} \tag{2.11}$$

The light emitted by the employed light source is unpolarized. After the transmission through the first linear polarizer the light is horizontally polarized (P_x cp. Fig. 2.3). As it is not possible to describe unpolarized light with the Jones matrix calculus, the Jones vector $\vec{E_x}$ will be used to describe the polarized light after the first linear polarizer.

$$\vec{E_x} = P_x \cdot \vec{E}_{unpol} = \begin{pmatrix} E_x \\ 0 \end{pmatrix}. \tag{2.12}$$

Hence, using the Jones matrix formalism the mathematical description of

the 3D-PLI measurements is as follows:

$$\begin{aligned}
\vec{E_T} =& P_y \cdot M_{\text{fiber}}(\delta,\beta) \cdot M'_{\text{ret}}\left(\frac{\pi}{2}\right) \cdot \vec{E_x} \\
\overset{(2.6),(2.10),(2.11),(2.12)}{=}& \begin{pmatrix} 0 & 0 \\ 0 & 1 \end{pmatrix} \cdot M_{\text{fiber}}(\delta,\beta) \cdot \frac{1}{\sqrt{2}} \begin{pmatrix} 1 & -\mathrm{i} \\ -\mathrm{i} & 1 \end{pmatrix} \cdot \begin{pmatrix} E_x \\ 0 \end{pmatrix} \\
=& \frac{E_x}{\sqrt{2}} \left[\mathrm{i} \sin\left(\frac{\delta}{2}\right) \sin(2\beta) - \mathrm{i} \cos\left(\frac{\delta}{2}\right) - \sin\left(\frac{\delta}{2}\right) \cos(2\beta) \right] \vec{e_y} \\
=& \frac{E_x}{\sqrt{2}} \Bigg[\underbrace{-\sin\left(\frac{\delta}{2}\right) \cos(2\beta)}_{\text{Re}} + \mathrm{i} \underbrace{\left(\sin\left(\frac{\delta}{2}\right) \sin(2\beta) - \cos\left(\frac{\delta}{2}\right) \right)}_{\text{Im}} \Bigg] \vec{e_y}
\end{aligned} \tag{2.13}$$

where $\vec{E}_x$ and $\vec{E_T}$ represent the electrical field vector after the first linear polarizer and the electric field vector of the transmitted light, P_y describes the second linear polarizer (also called analyzer), $M'_{\text{ret}}\left(\frac{\pi}{2}\right)$ describes the quarter-wave retarder and $M_{\text{fiber}}(\delta,\beta)$ describes the rotated brain tissue.
The measured light intensity I_T can be described in terms of the in-plane direction angle φ with respect to the filter rotation angle ρ, and the light retardation r:

$$\begin{aligned}
I_T \sim& |\vec{E_T}|^2 = \mathrm{Re}^2(\vec{E_T}) + \mathrm{Im}^2(\vec{E_T}) \\
\overset{(2.13)}{=}& \frac{E_x^2}{2} \left[\sin^2\left(\frac{\delta}{2}\right) \cos^2(2\beta) + \left(\sin\left(\frac{\delta}{2}\right) \sin(2\beta) - \cos\left(\frac{\delta}{2}\right) \right)^2 \right] \\
=& \frac{E_x^2}{2} \Bigg[\sin^2\left(\frac{\delta}{2}\right) \cos^2(2\beta) + \sin^2\left(\frac{\delta}{2}\right) \sin^2(2\beta) - 2\sin\left(\frac{\delta}{2}\right) \\
& \cdot \sin(2\beta) \cos\left(\frac{\delta}{2}\right) + \cos^2\left(\frac{\delta}{2}\right) \Bigg] \\
=& \frac{E_x^2}{2} \left[1 - 2\sin\left(\frac{\delta}{2}\right) \cos\left(\frac{\delta}{2}\right) \sin(2\beta) \right] \\
=& \frac{E_x^2}{2} \left[1 - \sin(\delta) \sin(2\beta) \right] \\
=& \frac{E_x^2}{2} \left[1 - \sin(\delta) \sin(2\varphi - 2\rho) \right] \\
I_T(\rho) \sim& \frac{I_{0T}}{2} \left[1 + \sin(2(\rho - \varphi)) \sin(\delta) \right],
\end{aligned} \tag{2.14}$$

with

$$\delta \overset{(2.4)}{=} 2\pi \frac{t\Delta n}{\lambda} \cos^2(\alpha). \tag{2.15}$$

I_{0T} corresponds to the transmitted light intensity which comprises the attenuation of light by scattering effects and absorption, but not the modification of the light intensity due to birefringent effects.
Equation (2.14) can be rearranged to:

$$I_T(\rho) = I_{0T}\left(\frac{1}{2} + \frac{\sin(\delta)}{2}(\sin(2\rho - 2\varphi))\right). \tag{2.16}$$

The transmitted light intensity measured with the described polarimetric setup describes a sinusoidal signal (Fig. 2.5). The normalized amplitude of the measured signal corresponds to the retardation r and the phase shift to the in-plane direction angle φ (cf. Eq. 2.16). The direction angle corresponds to the rotation angle for which $I = I_{0T}/2$. It is important to note, that only the first $I_{0T}/2$-crossing after the minimum ($I = I_{\min}$) is considered to prevent ambiguousness.

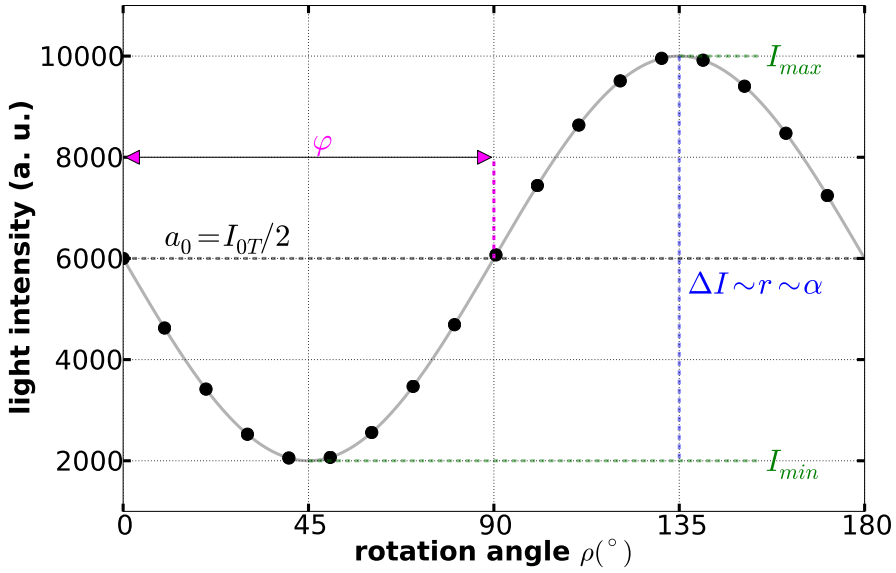

Figure 2.5: Measured signal. Due to the birefringence of nerve fibers and the filter rotation, the measured signal intensity changes in a sinusoidal manner. The intensity I changes depending on the rotation angle of the filters ρ. The phase of the sinusoidal signal correlates with the in-plane direction of the fiber φ. The out-of-plane inclination angle α correlates according to Equation (2.15) to the normalized amplitude ($\Delta I/I_{0T}$) of the sinusoidal signal where ΔI denotes the amplitude of the sinusoidal signal.

2.4.4 Fourier Analysis of the 3D-PLI Signal

The 3D-PLI signal is analyzed by using a discrete harmonic Fourier analysis. The transmitted light intensity $I_T(\rho)$ (Eq. 2.16) can also be expressed by:

$$I_T(\rho) = a_0 + a_1 \sin(2\rho) + b_1 \cos(2\rho), \tag{2.17}$$

with the Fourier coefficients:

$$a_0 = \frac{I_{0T}}{2}, \tag{2.18}$$

$$a_1 = \frac{I_{0T}}{2} \sin(\delta) \cos(2\varphi), \tag{2.19}$$

$$b_1 = -\frac{I_{0T}}{2} \sin(\delta) \sin(2\varphi). \tag{2.20}$$

The used convention of the discrete Fourier analysis is in accordance with to the convention introduced by Axer et al. [39]. The Fourier coefficients can be calculated from the 3D-PLI standard measurement using a discrete approximation. The analysis considers the measurement at each rotation angle $(\rho_1 \dots \rho_N)$. The total number of measurements N is in our case 18.

$$\begin{aligned} a_0 =& \frac{1}{N} \sum_{i=1}^{N} I_T(\rho_i), \\ a_1 =& \frac{2}{N} \sum_{i=1}^{N} \sin(2\rho_i) I_T(\rho_i), \\ b_1 =& \frac{2}{N} \sum_{i=1}^{N} \cos(2\rho_i) I_T(\rho_i). \end{aligned}$$

Using the given Fourier coefficients, the light transmittance I_0, the in-plane fiber orientation φ, and the light retardance $\sin(\delta)$ can be calculated for each pixel according to:

$$I_{0T} = 2a_0, \tag{2.21}$$

$$r \equiv |\sin(\delta)| = |\frac{\sqrt{a_1^2 + b_1^2}}{a_0}|, \tag{2.22}$$

$$\varphi = \frac{\pi}{2} + \frac{1}{2}\text{arctan2}(-b_1, a_1) = \frac{\pi}{2} + \begin{cases} \arctan(b_1/a_1) & a_1 > 0 \\ \arctan(b_1/a_1 + \pi) & b_1 \geq 0, a_1 < 0 \\ \arctan(b_1/a_1 - \pi) & b_1 < 0, a_1 < 0 \\ \pi/2 & b_1 > 0, a_1 = 0 \\ -\pi/2 & b_1 < 0, a_1 = 0 \end{cases} \tag{2.23}$$

r represents the measured amplitude of the signal.
In this case, the Fourier analysis provides the possibility to replace the least square fit of the measured sinusoidal signal with a faster, but still accurate computing procedure.

2.4.5 Calculation of the Inclination Angle

The inclination angle of the nerve fiber can be derived from the measured retardation value according to Equation (2.15) if the section thickness, the birefringence, and the wavelength are known. However, this is generally not the case. Thus, Axer et al. [39] introduced the factor t_{rel} (relative section thickness) to account for the signal variation introduced by different parameter sets. In this case, r can be described by:

$$r = \left| \sin\left(\frac{\pi}{2} t_{\mathrm{rel}} \cos^2(\alpha)\right) \right|, \tag{2.24}$$

with $t_{rel} = \frac{t}{t_{\lambda/4}} = \frac{4t\Delta n}{\lambda}$.
The parameter $t_{\lambda/4}$ represents the section thickness for which the extraordinary wave is retarded by a quarter of a wavelength with respect to the ordinary wave. In this case the measured retardation signal is maximal ($r_{\max} = 1.0$). The value for t_{rel} is determined for each section individually. It is assumed that a whole human brain section contains partially in-plane fibers ($\alpha = 0\,^\circ$) for which the maximal retardation is measured. Employing the histogram of the retardation values, the value for t_{rel} are determined. The in-plane fibers are assumed to be represented in the tail of the histogram. Due to local variations of fiber orientations, myelination, section thickness, and digital noise, the highest retardation value is not representative for in-plane fibers. Thus, the tail of the histogram is fitted with a modified sigmoidal function [39].
However, due to the $\cos^2(\alpha)$ in the retardation formula (see Eq. (2.24)), an ambiguity in the sign of the inclination angle exists, for a single polarimetric measurement. Fibers with an inclination angle of $\pm\alpha$ cannot be distinguished.
This problem can, for example, be tackled by tilting the specimen stage [49, 50]. The tilting of the specimen enables to measure the fibers from different angles of view. By tilting the specimen stage the inclination angle of the fibers are artificially changed, resulting in different retardation values. This change of the retardation value gives information about the sign of the inclination angle. The here described analysis of the measured signal which does not incorporate the tilting of the specimen stage is going to be referred to as the "standard analysis" throughout this thesis.

2.5 Post-processing

The visualization of the extracted 3D fiber orientation of the individual sections is done by means of color coding techniques as shown in Figure 2.6. By default, the RGB color space is used to generate so-called 'Fiber Orientation Maps' (FOMs). This type of color coding is attributed to the color schemes used in diffusion tensor imaging [51].

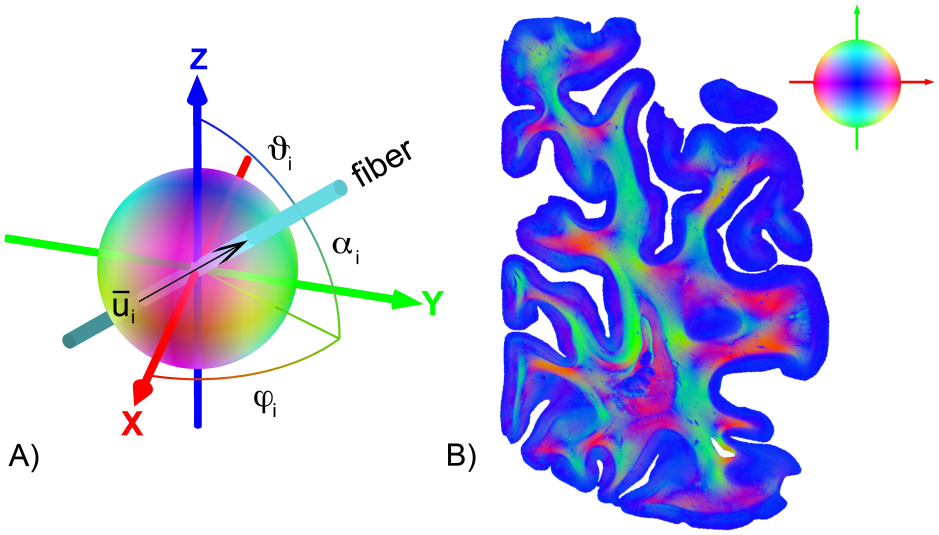

Figure 2.6: Color coding with the RGB colorspace. (A) Employed color code to visualize the orientation of nerve fibers in 3D-space. (B) The fiber orientation of a brain section is encoded according to the scheme visualized with the color bubble. Fibers running parallel to the x-axis are labeled in red, while fibers running parallel to the y-axis are displayed in green, and fibers pointing to the z-axis are colored in blue.

The unit vectors are calculated according to:

$$\text{Red} : x = \cos(\alpha)\cos(\varphi), \tag{2.25}$$

$$\text{Green} : y = \cos(\alpha)\sin(\varphi), \tag{2.26}$$

$$\text{Blue} : z = \sin(\alpha). \tag{2.27}$$

Using this color scheme, the 3D orientation of nerve fibers in a given brain section is easily accessible for the observer.
To enable a 3D reconstruction, blockface images are captured during the cutting procedure. The blockface images of the sectioned brain, are regis-

tered using a marker-based alignment and a non-linear refinement [40]. The alignment of the blockface images is necessary to provide a reference brain without cutting artifacts. Within the images of the same section obtained with the LAP and the blockface images features are extracted and a suited b-spline transformation is applied for alignment.

Chapter 3

Characterization and Optimization of Polarimetric Setups

In this thesis, two polarimeters are employed for the pursuit of a multiscale analysis. The first polarimeter covers a large field of view and is called large-area polarimeter (LAP). It has a mesoscopic resolution, which enables the visualization of long distance, interhemispheric fiber bundles. Imaging one section of a human brain takes about 15 min thus a whole human brain consisting of approximately 2000 sections is measured within 500 h. The second polarimeter, referred to as the polarizing microscope (PM), was custom made by *Taorad GmbH*. It has a high microscopic resolution, but a rather limited field of view. It is possible to map single nerve fibers with the PM, but it would take 16.000 h of data acquisition to measure an entire human brain.

Both polarimeters share a similar basic setup, however, the measured fiber orientations are not directly comparable, inhibiting the intended multiscale approach. The LAP incorporates an LED panel, a set of two rotatable crossed linear polarizers, a rotatable quarter-wave retarder, an object stage, and a digital camera for imaging purposes (cf. Fig. 3.1 A). The quarter-wave retarder is oriented at an angle of 45 ° to the linear polarizer. The ability of the object stage to be tilted into four complementary directions (north (N), east (E), south (S), west (W)), as indicated in Fig. 3.1 A, is only implemented in the LAP and enables the solving of the previously mentioned

sign ambiguity (cf. Sec. 2.4.5) of the standard planar view [45]. The PM contains basically the same type of elements as the LAP (Fig. 3.1 B), but instead of using circularly polarized light, the sample is illuminated with linearly polarized light and the polarization of the sample is analyzed with a combination of a fixed linear polarizer, a fixed quarter-wave retarder, and a rotatable linear polarizer. The quarter-wave plate is as in the LAP adjusted at an angle of 45 ° with respect to the main axes of the linear polarizer. The field of view of the PM is limited, therefore the object stage is moved by motors along the x- and y-axis so that the chosen region of interest (ROI) is scanned systematically. Furthermore, a motor along the z-axis is implemented in order to change the focal position. The focal position is adjusted individually for each measured section. At each position, a standard PLI measurement is performed. The tiles are imaged containing an overlap to the neighbouring tile to enable an automatic stitching of the tiles, using an in-house developed software tool, to create a high-resolution image of the ROI.

In order to ensure the best possible measurements, a correct signal interpretation, and the pursuit of the multiscale approach, both polarimetric systems are thoroughly characterized. The possibility of investigating the individual components of the PM are limited since it was delivered as a closed unit (cf. Fig. 3.1 B). However, in the PM only high-quality, off-the-shelf components are implemented, which are thoroughly characterized by the manufacturers. In contrast, the LAP is an in-house development and components are from different vendors. Due to the large size of the components the quality is limited. A more thorough assessment of the system properties of the LAP is possible as the single components are accessible. Still, wherever feasible, the properties of the PM were also determined.

It is difficult to differentiate the different influences on the system properties. For example, the imaging resolution is not only influenced by the performance of the lens, but also by the detector, the imaging contrast and the other components in the light path, such as the polarization filters. In order to differentiate their impact, the influences of the different components were investigated separately, wherever feasible. Figure 3.2 shows a flow chart of the assumed main influences regarding the investigated system properties.

In the following chapter, first the properties of the illumination, which are

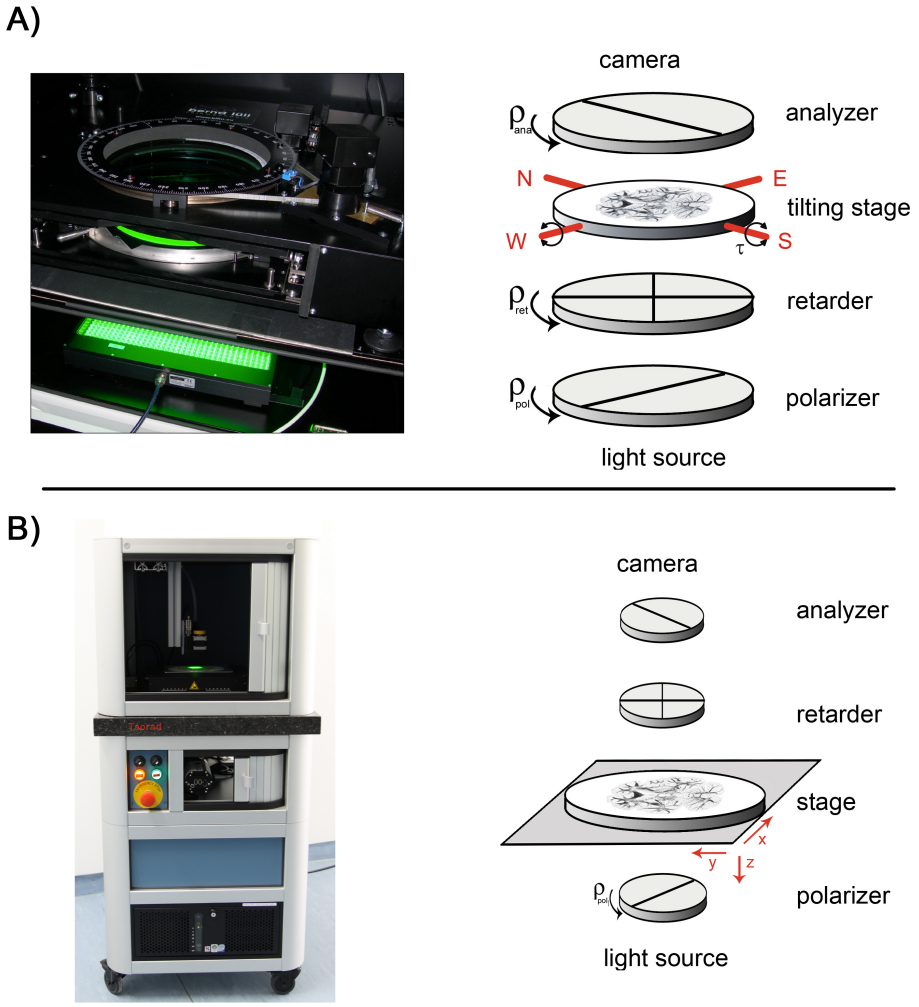

Figure 3.1: Employed polarimetric setups. A) Large-area polarimeter and B) polarizing microscope. The polarization elements alter the polarization state of the light in a defined manner. The large-area polarimeter additionally contains a tilting object stage and the polarizing microscope a moveable object stage to enable a successive scanning of the tissue.

influenced by the light source and the diffusor plate (→ LAP) or Koehler illumination [52] (→ PM) will be investigated (purple lines). Second, the polarization effects of the employed filters and the camera chip will be analyzed (blue line). Third, the impact of the lens, the scanning rate of the camera chip, and the polarization filters will be determined (green line). Finally, the system sensitivity will be investigated (red line).
For a better understanding, each of the described system properties is treated within a separate section containing the relevant theoretical background, the used materials and methods as well as the results and discussion. The materials and methods for the LAP and the PM will be described in the same section. In case a certain measurements was only performed for one setup this is pointed out in the sections labelled LAP specific" or PM specific". The results of the LAP and PM are presented and discussed separately to enable a clearer distinction between the two polarimetric systems. Finally, the measured system properties of both systems are compared and their influence on the measurement of fiber orientations is discussed.

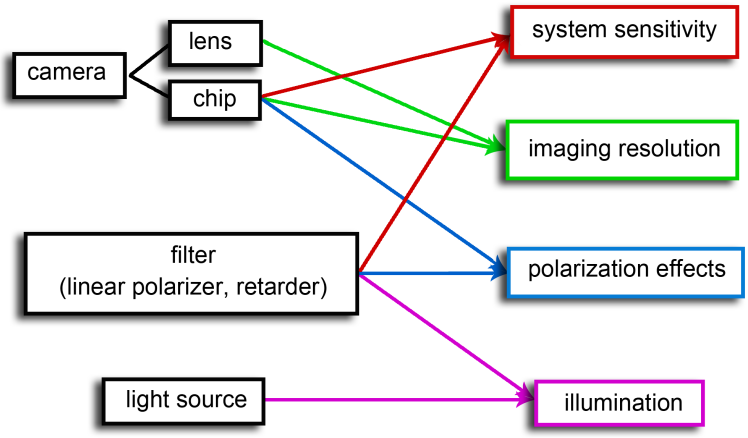

Figure 3.2: System properties. Dependencies between the components of the system and the investigated properties are indicated by colored arrows.

3.1 Stabilization and Homogeneity of Illumination

3.1.1 Materials and Methods

In both systems, LEDs are implemented as an illumination source as they provide a high efficiency, a high reliability, and a short time until the output intensity stabilizes. However, their electrical and optical characteristics are temperature dependent. The output light intensity and the output spectrum depend on the temperature of the p-n junction within an LED. With an increase in junction temperature, the working point is shifted and the luminescence of the LED is decreased. This process is referred to as "thermal stabilization" [53]. It is highly desirable to operate LEDs at a constant temperature to provide a uniform illumination across operation time. In order to provide a uniform illumination across the field of view, the lighting and the employed filters need to be homogeneous. Only then, a position and time independent interpretation of the signal is ensured. The transmitted signals are only conclusive in case of a high degree of homogeneity of the filters. Especially, when rotating the filters inhomogeneous absorptions influence the measured amplitude and phase of the signal, distorting the signal induced by the orientation of nerve fibers.
Thus, by default, a calibration procedure is incorporated in the PLI workflow to compensate for the inhomogeneities of the light source and the polarization filters. For this purpose, 100 empty images for each of the 18 rotation angles are captured. The 100 images per rotation angle are summarized to one image containing the mode values for each individual pixel position, resulting in 18 "mode-images". Afterwards, the mode value of all 1800 images and pixels is calculated and used as a reference value to determine the gain correction factors at each pixel position. These gain correction factors are then used to compensate for the inhomogeneities [54].

Thermal stability. The significance of the temperature dependency of the LEDs in terms of output intensity was investigated in the standard polarimetric setups, using the implemented digital sensors for intensity measurements. Every 60 s an image was captured with the digital camera of the LAP and the mean intensity of a central, circular ROI with a diameter of 1000 pixels was determined. For the LAP, the measurements were performed for the standard and a water-cooled LED. With the camera of the PM, ev-

ery 30 s an image was captured and the complete field of view was used for the evaluation. In total, the measurements lasted up to eight hours. Before every measurement, it was ensured that the LEDs were cooled down to test the reproducibility of the thermal stabilization.

Spectrum. Furthermore, the spectrum and a possible shift of the spectrum during the thermal stabilization were investigated for both illumination sources. Measurements of the spectrum of the illumination were performed by Christoph Zahren (Institut fuer Klima- und Energietechnik, Forschungszentrum Juelich) with a spectrometer (CAS140CT) from *Instrument systems*. The measurements were performed for the water-cooled LED panel of the LAP and the white light LED in the PM every second for a duration of 30 min for a wavelength range of 299 nm$< \lambda <$ 1100 nm in 0.8 nm-steps . Only the change of the peak wavelength was analyzed.

Illumination uniformity. The illumination uniformity incorporates the uniformity of the light source, the homogeneity of the filters as well as the combined influence of filters and light source. For the LAP, a thorough analysis of the homogeneity of each single filter was performed. While for the PM, only an overall performance investigation was possible due to the nature of its encased setup. For both systems, the influence of the image noise (σ) and the illumination inhomogeneities were distinguished. To determine the image noise, 100 images for were captured for $\rho = 0°$, and a "standard deviation image", containing the standard deviation of the mean over all 100 images each single pixel, was calculated. The histogram of the standard deviation image was analyzed.

For the LAP, the investigation of the uniformity of the illumination was executed in several steps. For all investigations, a centralized, circular ROI with a diameter of 1800 pixels was chosen in order to neglect the light decrease towards the image edges. First, all polarization filters were removed from the path of light to measure the output intensity (I_T) of the LED light source. Second, the filters were placed one by one into the light path and the amount of transmitted light was measured. The homogeneity of the filters was analyzed by capturing empty images for each individual filter and normalizing these images with an image of the illumination source. The full width half maximum (FWHM) of the Gaussian distribution of the histogram of these normalized empty images indicated the inhomogeneity level of the filter.

Furthermore, the filters were inserted separately and each filter was rotated in 10°-steps from 0° to 170°. The influence of the non-uniform illumination was eliminated by normalizing the images with the background image (containing only the influence of the LED). Thus, discrepancies caused by the rotation of the filters were revealed.
Additionally to the individual investigations of the filters and the light source, which were only performed with the LAP, a standard PLI measurement with all three filters in the light path and without a specimen was executed. The homogeneity of the overall illumination was measured, analyzing the intensity distribution. As a measure of homogeneity, the FWHM of the measured Gaussian distribution of the histogram was analyzed. The level of homogeneity is expressed as the correlation between the FWHM and the peak intensity: $\frac{\Delta I_{\mathrm{FWHM}}}{I_{\mathrm{peak}}}$.
Furthermore, the efficiency to compensate inhomogeneities with the described calibration procedure was tested by applying it to this data set.

3.1.1.1 LAP specific

For the LAP, two different LED panels (FZJ-SSQ300-ALK-G) custom-made by *iiMAGmeasurement + engineering* (Germany) were investigated. By default, a non-cooled system is used, but considering the temperature dependence the influence of a water-cooled panel was also examined. For the panels, 5 mm-LEDs (NSPG 510S) from *Nichia corporation* are arranged in a 36×36 array, illuminating an area of $300 \times 300\,\mathrm{mm}^2$ and are operated in the constant current mode. The specified central wavelength for an operating temperature of $25\,^{\circ}C$ and a current of 20 mA is $\lambda_{\mathrm{LAP,\,ill}} = 525\,\mathrm{nm}$.
To achieve a uniform illumination, a diffusor plate with a thickness of 6 mm made out of transparent thermoplastic acrylglas (also called PMMA) is inserted above the LED panel.
The employed circular large-area polymer filters with a diameter of 300 mm are manufactured by *Jos. Schneider Optische Werke GmbH*. They are encased between two glass plates for mechanical stabilization.

3.1.1.2 PM specific

In contrast to the LAP, the PM uses only a single white LED whose light is guided by a bundle of optical fibers. The desired wavelength is ex-

tracted with a band-pass filter with a specified central peak wavelength of $\lambda = (550 \pm 5)\,\mathrm{nm}$. To ensure a uniform illumination a Koehler illumination [52] is used. The Koehler illumination ensures a homogeneous illumination of the sample by assuring that the image of the light source is defocused in the sample plane and its conjugate image plane. For this purpose, a collector lens, a field diaphragm, a condenser diaphragm, and a condenser lens are placed between the light source and the sample stage. The implemented LED is an *IntraLED 2020+* operated at 24 W.
The employed filters in the PM are high quality, standard filters for microscopy with a diameter of 1 inch.

3.1.2 Results

3.1.2.1 Results LAP

Thermal stability. The measurements of the standard non-cooled LED panel confirmed that the emitted light intensity of the LEDs depends on the operating temperature. The temperature increased with operation time and consequently the measured light intensity decreases exponentially as shown in Figure 3.3 (magenta graph). Before this study was conducted, as a rule of thumb the first measurements of a day were executed 20 min after activating the LED panel. This study revealed that after activating the LEDs an intensity change of only $\Delta I_{nc}(20\,\mathrm{min}) = 54\,\mathrm{a.u.} \hat{=} 0.6\,\%$ could be observed. However, the output light intensity of the LEDs did not stabilize after 20 min, but tended to decrease even further. After 475 min, the output intensity had dropped down from 7242 a.u. to 6980 a.u. , leading to a total intensity loss of $\Delta I_{\mathrm{nc}}(475\,\mathrm{min}) = 232\,\mathrm{a.u.} \hat{=} 3.22\,\%$. The LED panel reached its operation temperature after 280 min as the intensity then changed only about 0.25 %.
The replacement with a water-cooled LED panel (referred to with the index '*wc*') significantly increased the reliability of the illumination intensity. After 20 min, the intensity had only dropped down about $\Delta I_{\mathrm{wc}}(20\,\mathrm{min}) = 0.5\,\%$ and after 43 min about $\Delta I_{\mathrm{wc}}(43\,\mathrm{min}) = 0.83\,\%$ (Fig. 3.3 in red). In total, the intensity decreased about $\Delta I_{\mathrm{wc}}(475\,\mathrm{min}) = 1.06\,\%$, instead of $\Delta I_{\mathrm{nc}}(475\,\mathrm{min}) = 3.22\,\%$ a.u. for the non-cooled panel. The thermal stability of the water-cooled system was almost reached after 43 min as the further intensity change was below 0.25 %.

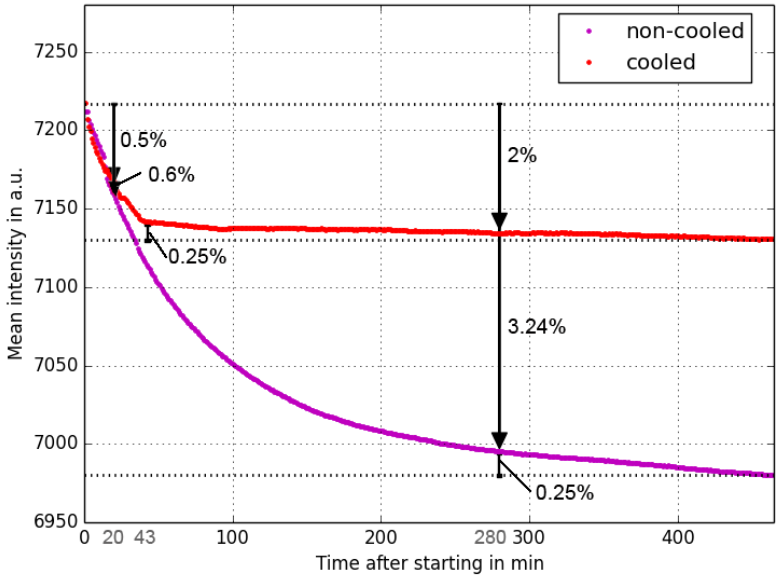

Figure 3.3: Thermal stabilization of the light source of the LAP. Intensity measurements of the LEDs implemented on the panel of the LAP with (red line) and without (magenta line) water-cooling over 475 min.

Spectrum. The spectral measurements revealed no distinct dependence of the spectrum on the operation temperature (cp. Fig. 3.4 B). The value of the peak wavelength oscillated around the peak wavelength of 527 nm. The green LEDs of the cooled LED-panel showed a slightly different peak wavelength of $\lambda_{\mathrm{LAP,ill,wc}} = 529\,\mathrm{nm}$ with an FWHM of 34 nm, than the non-cooled panel which has a peak wavelength of $\lambda_{\mathrm{LAP,ill,nc}} = (527 \pm 31)\,\mathrm{nm}$. The measured peak wavelength of the LEDs in the LAP differed slightly from the one specified by the manufacturer which is $\lambda_{\mathrm{LAP}} = 525\,\mathrm{nm}$.
While the illumination wavelength was $\lambda_{\mathrm{LAP,\,ill}} = 529\,\mathrm{nm}$ for the LAP, the optimal working wavelength for the retarder was specified with $\lambda_{\mathrm{LAP,ret}} = 568\,\mathrm{nm}$. Thus, there is a discrepancy of $\Delta\lambda_{\mathrm{LAP}} = 39\,\mathrm{nm}$.
Illumination uniformity. Despite the implemented diffuser plates, the background illumination of the LAP was not homogeneous (Fig. 3.6 A). The illumination appeared patch-like as if single LEDs were brighter than others. The inhomogeneity level corresponds to $\frac{\Delta I_{\mathrm{FWHM}}}{I_{\mathrm{peak}}} = 9.58\,\%$. The displayed histogram for the illumination of the LAP is asymmetric with more low than high intensities. This was caused by a gradual decrease in intensity towards

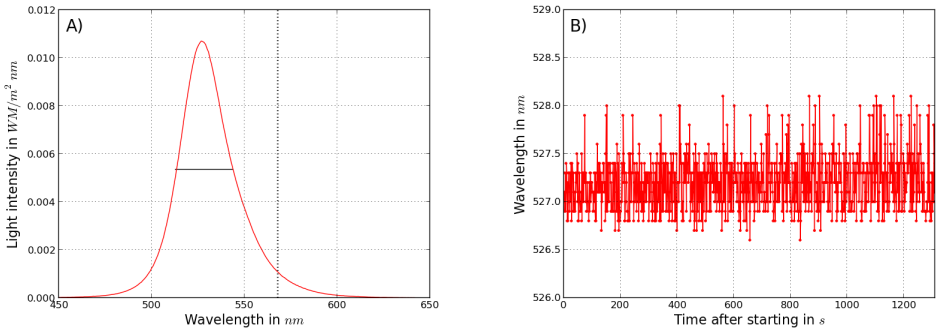

Figure 3.4: Spectrum of the LAP. Wavelength spectrum of the LEDs of the non-cooled LED panel (A) and the change of the peak wavelength over 22 min (B).

the image borders. The level of noise (Fig. 3.5 A, red dots) was much smaller than the inhomogeneity level and influenced the light variation only slightly. The noise caused by light fluctuations and photon detection in the camera (red dots) had an FWHM of 943 a.u. for the LAP (Fig. 3.5 A). The measured SNR is $\sigma_{\mathrm{LAP}} = 58$.

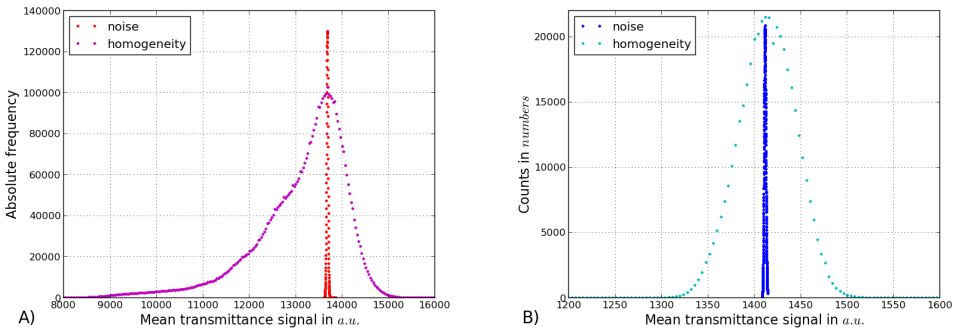

Figure 3.5: Homogeneity of the lighting of the (A) LAP and (B) PM. Histograms of the noise and the homogeneity level.

The quantity of the homogeneity of the filter is related to the transparency of the filter. The attenuation of the light through the center of the filters was not homogeneous and decreased gradually towards the image borders. The two linear polarization filters have a similar level of inhomogeneity with FWHM $\left(\frac{I_{\mathrm{pol}}}{I_T}\right) = 2.2\,\%$ and FWHM $\left(\frac{I_{\mathrm{ana}}}{I_T}\right) = 2.28\,\%$. The difference images of the normalized images with a rotation angle between 10 ° and 170 °

and $\rho = 0\,^\circ$ show grid-like structures for the polarizer (Fig. 3.6 B) and for the analyzer (C). when the polarizer or analyzer was rotated, the orientation of the structures changed depending on the rotation angle of the filter. In contrast, the retarder is more homogeneous with a measured FWHM of $\left(\frac{I_{\mathrm{ret}}}{I_0}\right) = 1.52\,\%$ and does not show a clear structuring of light attenuation (Fig. 3.6 D).

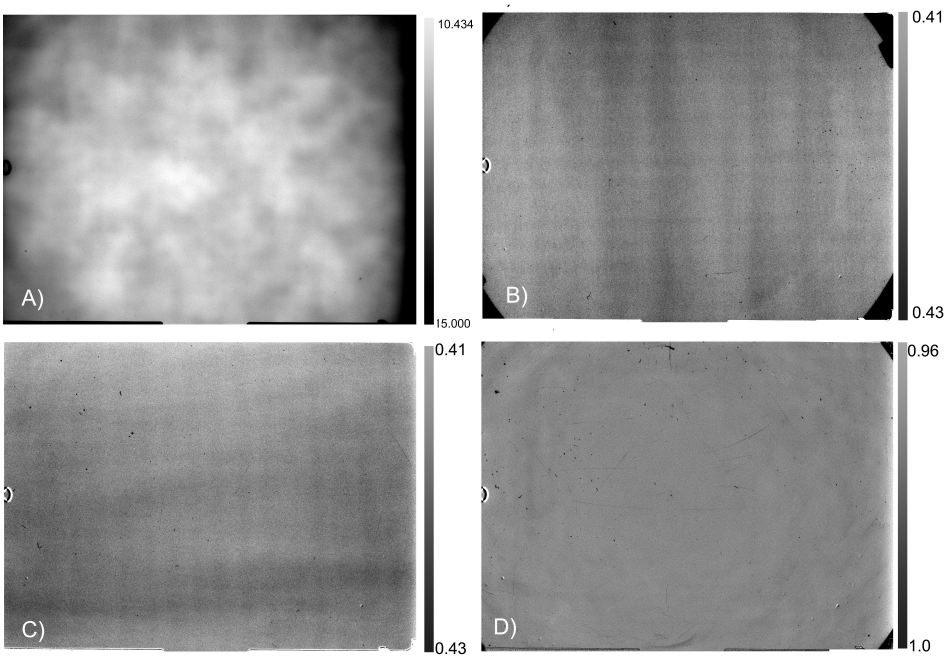

Figure 3.6: Homogeneity of the optical filters employed in the LAP. (A) shows the illumination provided by the LEDs and the diffuser (without any polarization elements in the light path). The normalized transmittance images of the polarizer (B) and analyzer (C) reveal grid-like structures, while the retarder (D) appears to transmit most of the incident light homogeneously, apart from dust particles which are visible as black dots.

The standard measurement with an empty object stage revealed a global sinusoidal modulation of the transmitted signal over all 18 rotation angles (Fig. 3.7, red points). The amplitude of the modulation is 0.95 %. The applied calibration procedure effectively compensates this effect and the mean intensity of the investigated ROI over all 18 rotation angles is homogeneous as shown in Figure 3.7 (magenta points). The values of the calibrated images are lower than the values of the non-calibrated images.

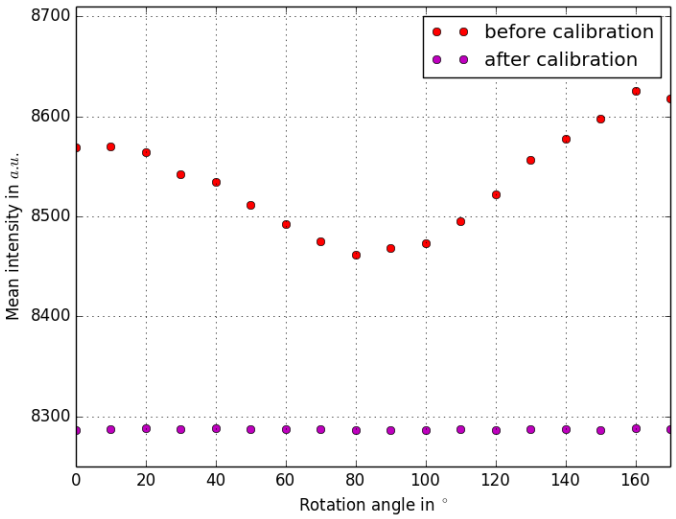

Figure 3.7: Effect of calibration for the LAP. The mean intensity of a centered circular ROI is plotted against the rotation angle before the application of the calibration (red) and after (magenta).

3.1.2.2 Results PM

Thermal stability. The intensity of the white LED of the PM also decreased with operation time. In Figure 3.8 one representative measurement of the tested LED is displayed. The tested LED stabilizes thermally within the first few seconds and even after 240 min of operating time, the intensity only decreases by about 0.25 %.

Spectrum. The spectral measurements of the PM also did not reveal any dependence of the spectrum on the operation temperature as visible in Figure 3.9 B. The samples within the PM are illuminated with a narrow spectrum of $\lambda_{\mathrm{PM,\,ill}} = (550 \pm 4.5)\,\mathrm{nm}$ (Fig. 3.9 B). In total, wavelengths between 540 nm and 560 nm pass the band-pass filter in the PM. The illumination wavelength and the optimal operation wavelength of the retarder just differ about 5 nm and are considered well matched.

Illumination uniformity. In Figure 3.5 B, the results for the analysis of the PM are shown. Even though the homogeneity of the polarization filters, the camera, and the light source were measured simultaneously, the empty images appear to be very homogeneous. The noise level as well as the inhomogeneity level are with $\frac{\Delta I_{\mathrm{FWHM}}}{\hat{I}}(\mathrm{PM}) = 5.4\,\%$ very low. The measured SNR

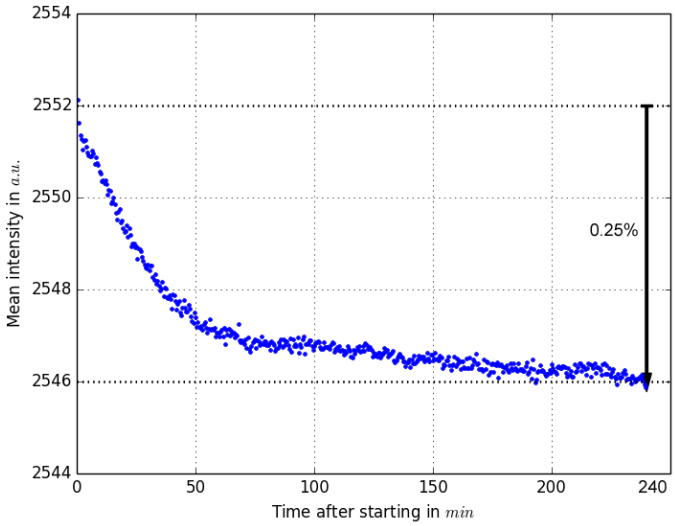

Figure 3.8: Thermal stabilization of PM. Intensity measurement of the LED implemented in the LAP, observed for a measuring time of 240 min.

level is about $\sigma_{PM} = 108$. The noise caused by light fluctuations and photon detection in the camera (blue line) has a small FWHM of 170 a.u. (Fig. 3.5 B, blue graph).
The standard PLI measurements with the PM also showed a sinusoidal dependence of the transmitted light on the rotation angle of the polarizer (Fig. 3.10, dark blue dots). The measured amplitude for such a blank measurement is 3.03 %, which corresponds to a retardation of $r = 0.0303$. The calibration procedure was capable of efficiently compensating for this effect (Fig. 3.10, cyan dots).

3.1.3 Discussion

3.1.3.1 Discussion LAP

The time in which the operating temperature is reached, is considerably longer than originally expected from literature research. Usually in literature the thermal stability of a single LED is described [53]. But in the present case, a panel consisting of 1296 LEDs was investigated. The panel represents a closed unit without an efficient heating dissipation. The temperature within the panel increased logarithmically over several hours, resulting in the observed exponential decrease of the light intensity. This increase in

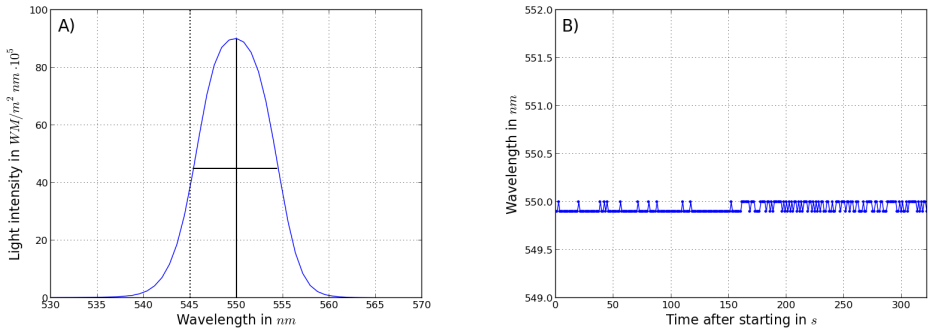

Figure 3.9: Spectrum of the LED in the PM. A) Wavelength spectrum of the illumination provided by the LED and B) the change of the peak wavelength over time.

temperature was efficiently counterbalanced by the implementation of the water-cooling unit into the LED panel, reducing the time for thermal stability by a factor of five. Thus, the water-cooling system depicts a great improvement of the setup.

The measured peak wavelength of the LEDs confirmed, within the margin of error, the specification of the manufacturer and was sufficiently accurate for further analysis.

The implementation of the chosen diffuser plate was not sufficient to provide a homogenous illumination. Thus, a diffuser plate with a higher efficiency with regards to the homogeneity is necessary to physically provide a homogeneous illumination. The resulting decrease of the illumination intensity can be counteracted by increasing the exposure time or by increasing the current of the LEDs. The visible grid-like structures of the linear polarizers as well as the intensity decrease towards the image borders, negatively influenced the homogeneity level of the filters. They originated from the manufacturing process of filters, during which chains of polyvinyl alcohol are stretched, causing the molecules to align in order to create a linear polarizer [55]. With aging, the structure becomes more unstable, causing the filters to become more and more inhomogeneous.

In order to compensate the systematic deviations from non-uniform illumination, the calibration function was applied. The inhomogeneities were successfully corrected and homogeneous blank images for all filter positions were ensured. The mean intensity of the calibrated images is lower than the

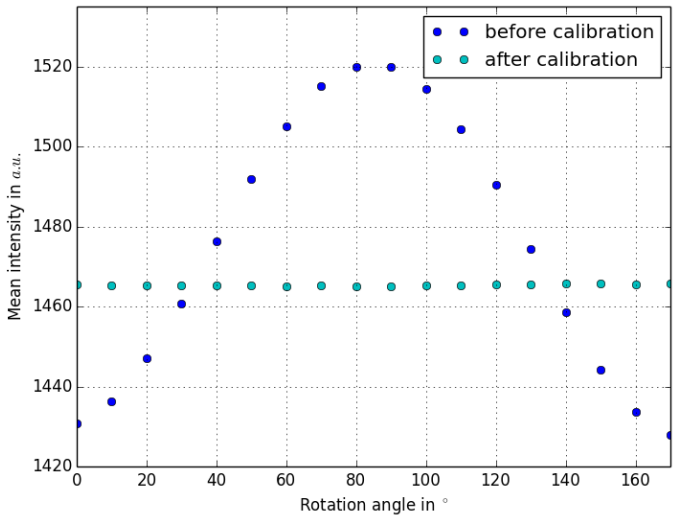

Figure 3.10: Effect of calibration for the PM. The mean intensity is plotted against the rotation angle before (blue) and after (cyan) the application of the calibration.

value of the raw image, as the reference value of the calibration is apparently 8278 a.u. However, the sinusoidal signal change of the mean intensity caused by the rotation of the filters, suggests a polarization effect, which will be investigated in the next section. If the intensity change is caused by polarization effects, it has to be clarified whether the calibration procedure is suited to compensate these effects. In general, it is advisable to minimize the non-desirable effects induced by instruments, instead of compensating them via digital post processing.

3.1.3.2 Discussion PM

The LED of the PM thermally stabilizes within the first few seconds, as described in literature for single LEDs [53]. Thus, the PM is operational within a short period of time.
The spectral measurements perfectly confirmed the specifications of the band-pass filter and no shift of the spectrum during the measured operation time was observed.
The Koehler setup specifically implemented for the purpose of a homogeneous illumination fulfills this task as expected and only a low level of inhomogeneity is measured. The measured change of intensity by rotation of

the filters is successfully compensated by the calibration function. However, regarding the calibration, the same considerations have to be made for the PM as described for the LAP.

3.2 Quality of Polarization Components

The polarizing elements are crucial to systematically control the input and to analyze the output state of polarization. The quality of the polarization elements directly influence the sensitivity of the system and henceforth the smallest signal change that can be detected (also called step size"). Within this section the homogeneity of the filters and their efficiency in polarizing light will be investigated. Furthermore, the possibility that the employed digital camera is sensitive to polarization states will be analyzed as previously described 3D-PLI standard measurements with a blank object stage (Sec. 3.1 indicated that a slight sensitivity of the digital camera to polarization states might exist).

3.2.1 Materials and Methods

The first linear polarization filter (polarizer) allows the control of the input state of polarization, while the second linear polarization filter (analyzer) provides the analysis of the output state of polarization. The quarter-wave retarder is implemented to solve the signal ambiguity of perpendicular directions, which exists if only two crossed polarizers are used [44].
In general, the quality of linear polarization filters is described by the extinction coefficient or rather the polarization efficiency and the level of homogeneity of the polarization efficiency.
In order to assess the quality of a linear polarizer, the incident light has to be linearly polarized with the polarization plane lying perpendicular to the transmission axes of the investigated filter. The amount of light after the filter specifies the efficiency of the modulation of the transmitted optical power of the investigated linear polarizer and is either referred to as Polarization Extinction Ratio (PER), optical density or absorbance of crossed linear polarizers. The polarization extinction coefficient is calculated by the ratio between the transmitted light through parallel (I_p) and through crossed (I_c) linear polarizers [56]:

$$\mathrm{PER} = -\log_{10}\left(\frac{I_c}{I_p}\right). \tag{3.1}$$

Another similarly common measure to evaluate the quality of linear polarizers is the polarization efficiency (η_p). Both measures can be found in

literature and are complementary. The polarization efficiency describes the amount of light that is linearly polarized by the filters [57]:

$$\eta_p = \frac{I_p - I_c}{I_p + I_c}. \tag{3.2}$$

The characterization of a quarter-wave retarder is more complicated. Its most relevant quality for 3D-PLI is the dependency of the light retardance on the illumination wavelength. The employed retarders are polymer waveplates as well as true zero-order waveplates. Thus, the induced phase shift between the ordinary and the extraordinary ray is exactly $\pi/2$ for a quarter-wave retarder. In opposition, the phase shift induced by multi-order waveplates is larger than the required one by an integer multiple of 2π. True-zero order retarders have an excellent performance and maintain the retardance also for slight deviations from their specified wavelength as shown in Figure 3.11 [58]. The exact performance of the employed retardance could not be investigated due to the limited available equipment. The possibility

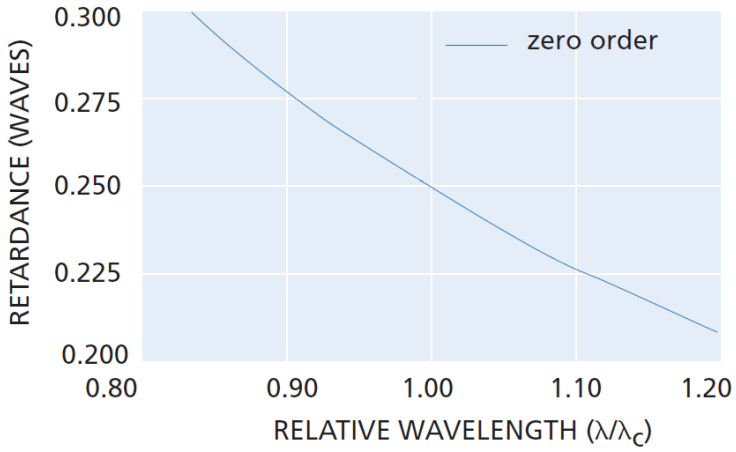

Figure 3.11: Retardance of a quarter-wave retarder for different wavelengths. The retardance of the light depends on the relative wavelength difference between the wavelength the retarder was optimized for and the incident light wavelength [58].

that Charge-coupled device(CCDs) are sensitive to polarization states is described in literature [59] and will be analyzed in the scope of this work.

Polarization efficiency. The actual performance of linear polarizers is described by the polarization efficiency (Eq. (3.1)), which states the amount

of light that is linearly polarized by the filters. For this experiment, the quarter-wave retarder was removed from the optical path. Then, the light transmitted through crossed (I_c) and parallel (I_p) linear polarizers was measured and the extinction ratio was calculated for each pixel.

Polarization sensitivity of camera. The sensitivity of the employed camera to states of polarization was investigated. Previous standard measurements with an empty object stage showed a sinusoidal modulation of the incident light. To clarify whether the camera is sensitive to states of polarization, the retarder was removed from the optic path, the transmission axes of both linear polarizers were aligned parallel, and the orientation of the camera was varied. At all times, the camera was equidistant to the object stage and only its in-plane orientation was changed. The orientation of the camera was varied with respect to the filters in five discrete steps: 0°, 82°, 175°, 292°, and 313°. These steps were chosen due to practical reasons. For each camera position, a standard measurement was performed and the signal change in a circular ROI that was centered around the rotation axis of the filters was measured. The ROI had a diameter of 1844 pixels.
These measurements were only performed for the LAP as it was not possible to change the orientation of the PM camera.

3.2.1.1 LAP specific

The employed filters in the LAP are custom made and are adapted for the intended purpose. No exact specifications were available for the filters, only specifications for similar filters.
The employed linear polarization filters within the LAP are dichromatic polymer sheet filters consisting of long chains of polymer molecules that are oriented in a single direction. The polarizing film is covered on both sides with cellulose acetobutyrate (CAB) and laminated between two glasses for mechanical stabilization. The filters produced by *Jos. Schneider Optische Werke GmbH* are optimized for a broad spectrum of 400 nm to 750 nm with a transmission of 38 % of the incident light. The crossed linear polarizers have a specified polarization extinction ratio of $PER = 3.2$ for $\lambda = 530\,\text{nm}$ and an extinction ratio of up to $10,000 : 1$ for $600\,\text{nm} < \lambda < 660\,\text{nm}$. The quarter-wave retarder is also produced by *Jos. Schneider Optische Werke GmbH* and causes a phase shift of a quarter-wavelength for light with $\lambda_{\text{LAP,ret}} = 568\,\text{nm}$. It consists of a single layer of polycarbonate sheet, which induces a bire-

fringence effect. According to technical reports of the manufacturer, such quarter-wave retarders behave like zero-order retarders [58].
The LAP employs a AxioCamHRc by *Carls Zeiss AG* to capture the intensity changes.

3.2.1.2 PM specific

The described evaluations were only executed for the LAP as the filters of the PM are standard filters which can be ordered by catalog and are thoroughly characterized by the manufacturer. The linear polarizers built-in in the microscope have a polarization efficiency of 99.8 %. The employed quarter-wave retarder is optimized for $\lambda_{\mathrm{PM,ret}} = 545\,\mathrm{nm}$. The quarter-wave retarder is a high quality polymer sheet cased in glass.

3.2.2 Results

Polarization efficiency. The investigation of the polarization qualities of the linear polarizers showed a lower quality than specified by the manufacturer. The measured transmitted light intensity for parallel polarizers is $I_p = 14357\,\mathrm{a.u.}$ and for crossed polarizers it is $I_c = 135\,\mathrm{a.u.}$ Thus, the extinction ratio and the polarization efficiency are: PER=2.2027 and $\eta_p(\mathrm{ana{+}pol}) = (98.1 \pm 0.09)\,\%$.
In Figure 3.12, the resulting image of the polarization efficiency for the LAP shows a decrease of the efficiency towards the borders of the image. The lowest value $\eta_{p,\mathrm{min}}(\mathrm{ana{+}pol}) = 96.9\,\%$ was measured at the right hand border. The polarization efficiency fluctuated in the center of the image between 98 % and 98.2 %.
Instead of the specified optical density of approximately PER=3.2 for $\lambda = 530\,\mathrm{nm}$ only an extinction coefficient of PER=2.2027 for $\lambda = 529 \pm 17\,\mathrm{nm}$, was measured with the current setup.
Polarization sensitivity of camera. The change of intensity observed for standard measurements with an empty object stage (shown in Fig. 3.7, red points) is related to the employed digital camera. The systematic variation of the orientation of the camera influences the phase of the measured sinusoidal signal (cf. Fig. 3.13). The rotation of the camera by 82 ° (Fig. 3.13 in red) induces a phase shift of roughly 45 ° when compared to the signal measured for a camera position of 0 °(blue line). Thus, a rotation (ρ_{cam}) of the

Figure 3.12: Polarization efficiency. Contrast enhanced image of the polarization efficiency of the employed linear polarizers of the LAP.

camera results in a phase shift of $\varphi \approx \frac{\Delta\rho_{\mathrm{cam}}}{2} + 90\,^\circ$. The camera orientation also slightly influenced the measured relative amplitude which varied between $\Delta I/I_{0T} = 0.55\,\%$ for $\rho_{\mathrm{cam}} = 313\,^\circ$ (magenta line) and $\Delta I/I_{0T} = 1.3\,\%$ for $\rho_{\mathrm{cam}} = 82\,^\circ$ (red line). Apart from the orientation $\rho_{\mathrm{cam}} = 175\,^\circ$ (yellow line) the measured intensity values are similar.

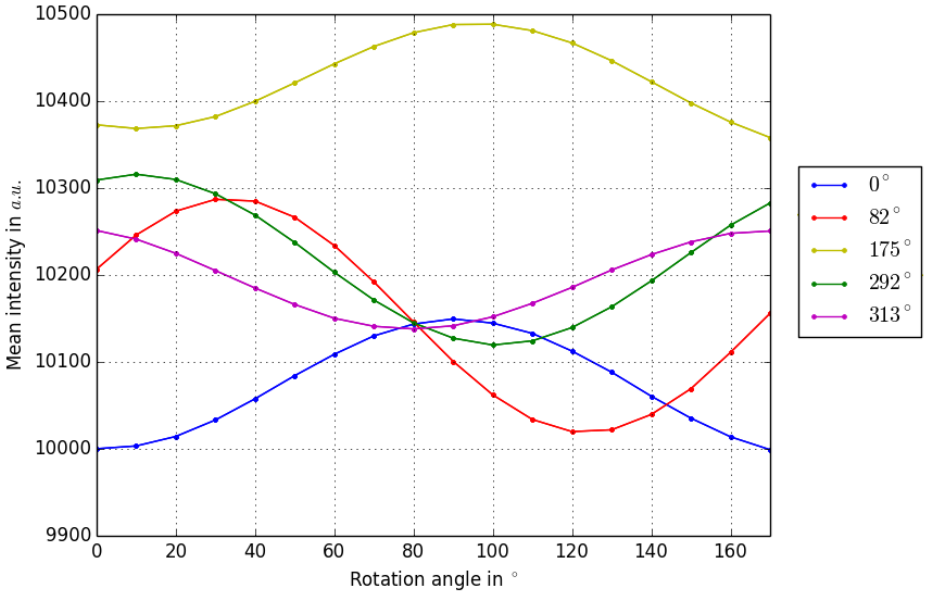

Figure 3.13: Polarization sensitivity of the camera. Depending on the camera orientation, the phase of the measured sinusoidal signal differs.

3.2.3 Discussion

In general, the measured quality of the linear polarization filters is lower than expected, which could be caused either by scattering on the surfaces within the setup, variations in the manufacturing process or aging effects of the polymer films. The slight deviations from the specifications regarding the polarization efficiency could also be due to different test setups. Typically, to investigate the polarization efficiency, the filters are illuminated with linearly polarized light and the transmission parallel and perpendicular to the oscillation direction of the electric field vector is measured. In contrast, our results were gained using the standard setup for the measurements of the nerve fiber orientation in brain sections. The polarization

efficiency of both filters was assessed simultaneously. Instead of using completely linearly polarized light, the light was only partially polarized by the first polarizer and analyzed by the second polarizer. Thus, the efficiency for each filter was $\eta_p(\text{pol}) = \eta_p(\text{ana}) = \sqrt{\eta_p(\text{ana+pol})} = 99.0\,\%$ instead of $\eta_p(\text{ana+pol}) = 98.1\,\%$. The low polarization efficiency affected the transparency of the filters. If the light is not perfectly linearly polarized, as indicated by the measured polarization efficiency, the light with the supposedly blocked component will be partially transmitted. In this case, a higher total transparency will be measured.
The decreased polarization efficiency could also be an aging effect of the employed, large-area filters. As described previously, with aging, the molecular alignment of the filters becomes more unstable. The recombination of the molecule chains cause a higher transparency of the linear filters regarding the supposedly blocked component. If the supposedly blocked polarization state passes the filter, the polarization efficiency will be decreased.
The sensor of the digital camera was slightly sensitive to the polarization states of the light. This effect has already been described in literature [59]. The slight variation of the amplitude for the different camera orientations were most likely induced by a minimal tilting of the camera head. In order to perform this measurement, the camera had to be removed from its standard orientation. In the standard setup, the camera orientation was not changeable. Thus, the camera was mounted on a tripod, which was then rotated accordingly. A tilting of the camera head was avoided as best as possible but cannot be excluded. The sensitivity of the camera to linear polarization states can negatively influence the measurements of the polarization efficiency. Depending on the main axis of the sensor, a different amount of light is detected. So far, this effect was counterbalanced with the applied calibration function.

3.3 Imaging Resolution and Optimal Imaging Settings

It is important to investigate the resolution of both imaging systems, in order to determine the smallest resolvable brain structures and to estimate the influence of partial volumes effects. Further details about partial volume effects are given in Section 4.1.2.
Of special interest are the optical performance of the LAP and the PM as well as the settings for which the best possible results, such as the highest resolution and the highest dynamic range, are obtained. The optical performance can be subdivided into the optical axial and lateral resolution limit, the object space resolution, and the modulation transfer function (MTF).

3.3.1 Materials and Methods

In general, the term "resolution" describes the ability to discriminate any two physical quantities. It specifies the smallest possible distance for which discrimination is feasible. The resolution of an imaging system is, on the one hand, restricted by the performance of its optical components, and on the other hand, by the properties of the detector. Transferring the statement of the Nyquist-Shannon theorem into the object space, it is theoretically possible to resolve structures that have double the size of the object space resolution, which is the represented size of a pixel in the object space [52,60]. However, in reality, the optical components also limit the optical resolving power. In order to obtain the best possible results, the resolving power of the lens should be matched with the resolution of the detector to avoid alias effects.
The performance of an optical system, including the lens and the detector, can be quantified by the modulation transfer function [61]. A point in object space is transferred into image space by an optical system according to its point-spread function. The MTF is defined as the ratio of the relative image contrast to the relative object contrast. It is sufficient to describe the quality of an imaging system only with the MTF, however, in this case, the explicit investigation of the optical resolution limit is also highly relevant. The resolution limit offers the possibility to draw a conclusion concerning the partial volume effects in x- and y-direction for both polarimeters.
The MTF can be determined by imaging structures with known spatial

frequencies and measuring the corresponding image contrast. In general, the image contrast is expressed using the Michelson contrast [62] (MI):

$$MI = \frac{I_{\max} - I_{\min}}{I_{\max} + I_{\min}}. \tag{3.3}$$

Several criteria to determine the optical resolution limit exist, such as the Sparrow criterion, the Rayleigh criterion [52] or other criteria such as a 40 %-contrast-criterion which is used by *Carl Zeiss AG*, for example. The most common criterion is the Rayleigh criterion which states that the resolution limit of an optical system is reached when the central maximum of the Airy disc of one imaged point falls below the first minimum of the neighbor point. This corresponds to a contrast of 15.3 % between the black and the white line. In literature, also a contrast of 26.4 % derived from $\frac{I_{\max}-I_{\min}}{I_{\max}}$ can be found. Thus, the distance (d_{xy}) between both resolved maxima is [52]:

$$d_{xy} = 1.22\frac{\lambda}{2n \cdot \sin(\Theta)} = 0.61\frac{\lambda}{NA}. \tag{3.4}$$

The resolution depends on the wavelength of the light (λ), the refractive index of the medium (n) as well as on the half acceptance angle (Θ) and the numerical aperture (NA).

Another important aspect in terms of the resolution is the axial resolving power of an optical system. The axial resolving power (d_z) is also known as depth of field, which is the distance between the nearest and the farthest object plane that are simultaneously in focus. The axial resolution is influenced by the wavelength of the illumination, the refractive index of the medium, the numerical aperture, the lateral resolution, and the lateral magnification (M) [52]:

$$d_z = \frac{\lambda \cdot n}{NA^2} + \frac{n}{M \cdot NA} \cdot d_{xy}. \tag{3.5}$$

The influence of the numerical aperture is higher along the axial direction than along the lateral direction.

The focal plane of the tissue is characterized by the fact that the imaged structures appear maximally sharp. Thus, I propose that by employing an edge detector, it is possible to determine the focal plane. An edge detector, such as the Sobel operator [63], detects large intensity changes in an image

under consideration of the 8-connected neighbor pixels. Within the edge-image, edges (= fast intensity changes in the original image) appear bright, while slow changes appear dark.
To achieve the best possible results with the given imaging system, the optimal exposure time and camera settings for imaging brain tissue were determined. The optimal exposure time provides a large amplitude of the PLI signal while simultaneously preventing overexposures. Overexposures are undesired as in over exposed areas the image information is lost.
It is also important to identify the critical aperture in order to ensure an optimal transfer of spatial frequencies. In general, two counteracting effects negatively influence the optical resolution of a system. On the one hand, the resolution is decreased for small aperture sizes due to diffraction. On the other hand, the ability to resolve fine details is limited due to aberrations of the lens for large aperture sizes (cf. Fig. 3.14). The critical aperture represents the aperture for which the net effect of these counteracting influences is minimal.

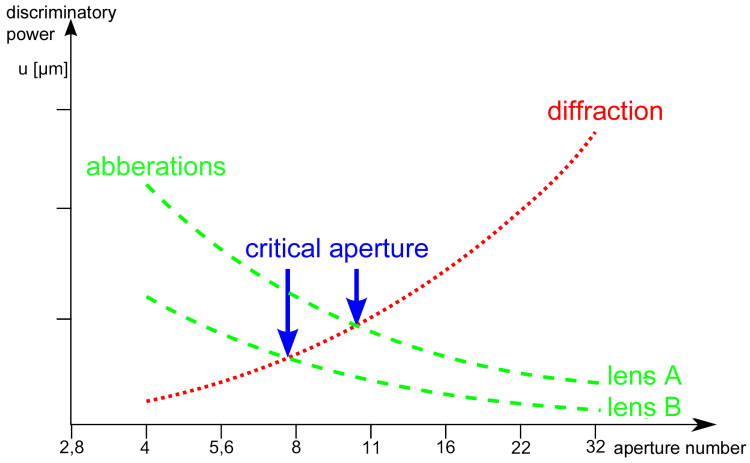

Figure 3.14: Critical aperture. The discriminatory power of a lens is limited by abberations and diffraction. The critical aperture provides the highest discriminatory power.

MTF. For the analysis, two "1951 USAF Resolution" testcharts containing structures with different spatial frequencies were used. Each element of the testcharts contains six lines - three horizontal and three vertical lines (cf. Fig. 3.15, left side). The testcharts were placed onto the object stages of the polarimeters. The high resolution target containing structures down

to 1.55 µm and the low resolution testchart containing structures between 400 µm and 4.39 µm were imaged with the PM and the LAP, respectively. The intensity of the black and the white part of the lines of each element was measured with accumulated line profiles (cf. Fig. 3.15, right side). The extracted values for the minimal and the maximal values were averaged separately and the Michelson contrast (Eq. (3.3)) for each element was calculated to determine the MTF.

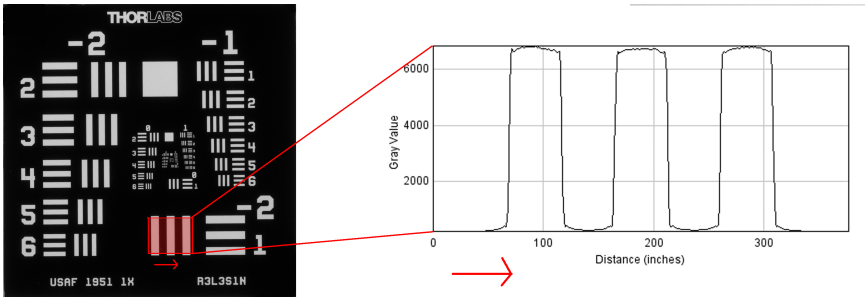

Figure 3.15: Resolution. The studies of the resolution properties of the systems are based on imaging a USAF testchart as shown on the left side. The measured contrast for the different line pairs is based on the results of the accumulated line profile as indicated on the right side.

Lateral resolution limit. The resolution limit was determined by using the data of the MTF curves. The line pair for which the Rayleigh criterion was fulfilled, was identified. The smallest resolvable distance with the employed setups corresponds to the reciprocal value of the determined number of line pairs. Furthermore, the influence of different scanning rates of the AxioCamHRc was tested. For the standard measurements in the LAP, a scanning resolution of $2776 \times 2080\,\mathrm{px}^2$ is used. However, the possibility to improve the transfer of spatial frequencies with a higher scanning resolution ($4164 \times 3120\,\mathrm{px}^2$) is given by the microscanning procedure of the Zeiss camera. Whether the increase of the scanning rate enhances the transfer of spatial frequencies was investigated using the low resolution USAF 1951 testchart.

Axial resolution. Theoretically, the focal depth can be calculated according to Equation (3.5). While this was possible for the PM as the necessary information such as the numerical aperture are known, the axial resolution for the LAP was estimated using the numerical aperture, which was determined from the measured lateral resolution limit. Using the predetermined lateral resolution and measured illumination wavelength, the numerical aperture of

the system can be calculated according to:

$$NA = \frac{0.61\lambda}{d_{xy}}. \tag{3.6}$$

This calculated numerical aperture was used to determine the minimal depth of field.

So far, the focus position within the PM has been manually determined for each investigated histological section. As for every microscopical technique, an individual focusing of each section is necessary. To enable a reliable, user-independent identification of the z-position, a semi-automated approach based on edge-detection has been developed within this work.

For this purpose, a brain section was placed on the object stage in the PM. First, the focus was manually predetermined, then the focal distance was decreased by 200 µm and stepwise increased in 10 µm-steps. For each position, a transmittance image was captured until a distance of 400 µm was covered. The images were taken at the rotation angle $\rho = 0\,^\circ$. Subsequently, the edges within the images were detected using the standard Sobel edge detector implemented in the software package *Fiji* [64]. The mean intensity of the edge image of each z-position was measured.

Optimal setting. In order to determine the optimal setting for the polarimetric measurements, the critical aperture and exposure time of the camera were determined. The aperture was changed in half aperture stops and the exposure time was adapted to ensure the same mean image brightness for all combinations. Once the critical aperture was identified, the optimal exposure time was investigated.

For the evaluation of the optimal exposure time, a tissue sample was chosen for which the amplitude of the PLI signal was measured to be maximal. The sample only contained parallel fibers which are oriented in the xy-plane. It was cut with a section thickness of 70 µm, which is currently the standard employed section thickness. This approach ensures that samples with a different composition of fibers are not overexposed. The sample was extracted from an optic tract of a human brain and cut parallel to the main fiber direction. For further details about the preparation of the optic tract, the reader is referred to Section 4.2.1. The exposure times were varied between 65 ms and 100 ms with an increment of 5 ms, and the output intensity for each rotation angle was measured to determine the exposure time that pro-

vides the maximal dynamic range of the signal.

3.3.1.1 LAP specific

For the LAP, a high resolution camera AxioCamHRc from *Carl Zeiss AG* and a high resolution standard lens, the Lametar 2.8/25 by *JENOPTIK - Laser, Optik, Systeme GmbH*, are used. The AxioCamHRc uses the possibility to shift the position of the digital sensor to enhance the sampling resolution from originally 1388×1040 up to 4164×3120. This procedure is called microscanning. The setting for the standard measurements is 2776×2080 with 5.8 Megapixel and 14 Bit per color channel. The lens has a specified contrast of 40 % for 120 LP/mm.

3.3.1.2 PM specific

The PM uses the digital camera Retiga 4000R Mono by *QImaging* with a resolution of 2048×2048 and is equipped with a Nikon TU Plan Fluor EPO P 5x lens with a specified numerical aperture of $NA = 0.15$.

3.3.2 Results

3.3.2.1 Results LAP

MTF. The LAP achieved high image contrasts of $MI = 0.91$ for low frequencies (Fig. 3.16, red squares and yellow stars) which gradually decreased towards higher frequencies. The MTF curves were plotted as a function of the spatial frequency in line pairs per mm against the Michelson contrast as shown in Figure 3.16. The chosen scanning rate in the LAP slightly influenced the transfer of the tested spatial frequencies. For the standard scanning rate of the LAP (2776×2080 - yellow stars Fig. 3.16), the contrast started to continuously decrease for spatial frequencies greater than 3 LP/mm. For the 4162×3120-scan (red squares in Fig. 3.16) the contrast started to decrease for spatial frequencies larger than 4 LP/mm. The resolution limit of the LAP was slightly increased for the higher sampling rate of the detector using the microscanning procedure. Additionally, the low spatial frequencies ($0.25\,\mathrm{LP/mm} < f < 3.5\,\mathrm{LP/mm}$) were transferred with a higher contrast using a pixel resolution of 4164×3120 (cf. Fig. 3.16).

Structures larger than 353 µm are well transmitted with a contrast down to 80 % and even structures with the size of 250 µm are still transferred with a contrast of about 50 %.

Lateral resolution limit. The optical resolution was lower than the optical space resolution which was 64 µm/px for the LAP.

The determined spatial frequency which is still considered resolved according to the Rayleigh criterion, is $d_{xy,LAP} = 6.3\,\mathrm{LP/mm}$, corresponding to an optical lateral resolution limit of 159 µm.

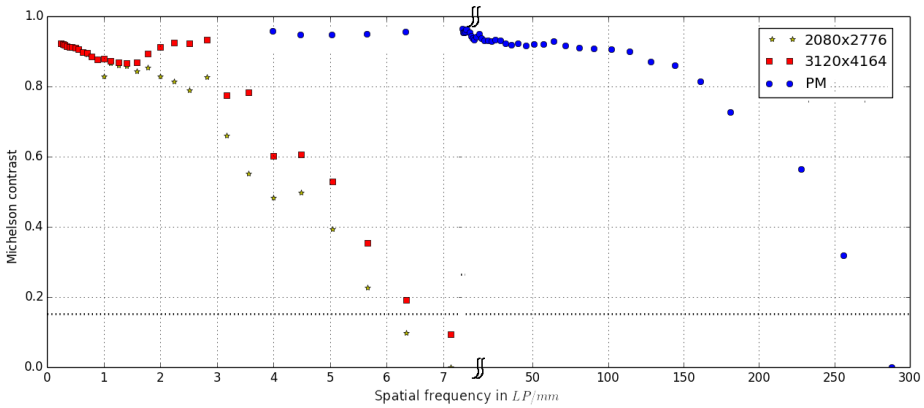

Figure 3.16: Modulation transfer function of the PM and LAP. The transfer of the different spatial frequencies was measured with USAF testcharts. For the LAP, different scanning rates ($2776 \times 2080\mathrm{px}^2$ - yellow stars, $4164 \times 3120\mathrm{px}^2$ - red squares) were tested.

Axial resolution. The calculated numerical aperture according to Equation (3.6) for the LAP is NA = 0.0018. Thus, with n = 1 the axial resolving power is $d_{\mathrm{z,LAP}} = 163\,\mathrm{mm}$.

Optimal settings. For the LAP, the optimal exposure time and critical aperture were determined. The chosen aperture (Tab 3.1) influenced the optical resolution limit of the system. The resolution limit decreased for higher apertures (small incident angles) and increased when the angle of incidence was broadend. A range of optimal apertures concerning the resolution limit exist between F/4 and F/6.7. The resolution limit can be improved by 44 % only by choosing the optimal aperture.

By employing the critical aperture, it was possible to investigate the optimal exposure time. In Figure 3.17, the results of the different exposure times are depicted. The measured intensity values vary with rotation angle and exposure time. For exposure times less than 80 ms (Fig. 3.17 purple line),

time in ms	Aperture	resolution limit
4.3 ms	2.8	198 µm
4.9 ms	3.4	177 µm
8 ms	4	177 µm
11.1 ms	4.8	177 µm
15.4 ms	5.6	177 µm
23.3 ms	6.7	177 µm
34.6 ms	8	177 µm
47.3 ms	9.5	198 µm
70.6 ms	11	223 µm
100 ms	13	281 µm
157.2 ms	16	315 µm

Table 3.1: Optimal working aperture. The resolution limit depends on the chosen aperture.

the signal is transferred without any implications. When the exposure time exceeded 85 ms, the signal was saturated for the maximum of the sinusoidal signal ($\rho = 140\,^{\circ}$). Thus, the measured retardation which is directly correlated to the amplitude of the sinusoidal signal, was lower for exposure times where the sample was overexposed (Tab. 3.2). The highest retardation signal ($r = 0.673$) was measured for exposure times of 80 ms and 75 ms.

exp. time	retardation value
65 ms	0.667
70 ms	0.670
75 ms	0.673
80 ms	0.673
85 ms	0.639
90 ms	0.626
95 ms	0.608
100 ms	0.585

Table 3.2: Optimal exposure time. The amplitude of measured signal depended on the exposure time.

3.3.2.2 Results PM

MTF. The optical components of the PM transferred the imaged spatial frequency exceptionally well (cf. Fig. 3.4, blue circles). Only for structures

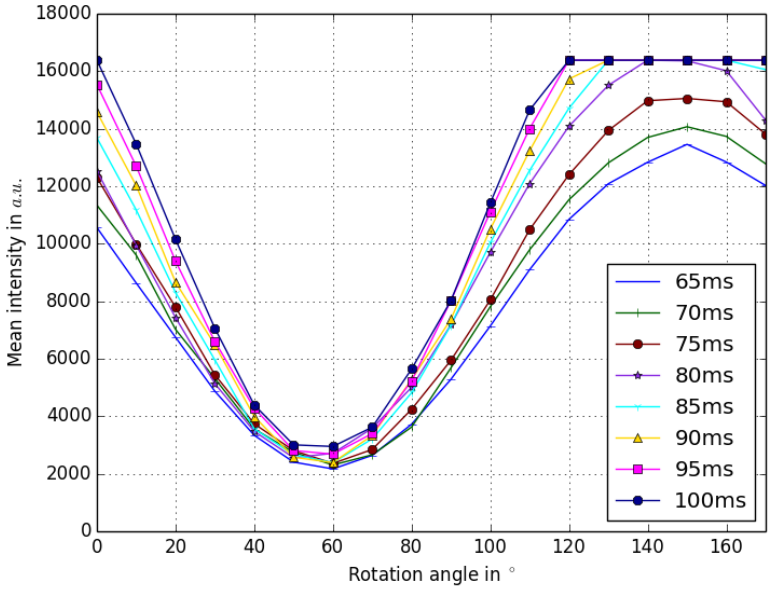

Figure 3.17: Optimal exposure time of the LAP. The signal response to the image optic tract during a standard measurement employing F/6.7 and different exposure times was investigated.

below 6.2 µm $\hat{=}$ 161 LP/mm, is the measured Michelson contrast lower than 80 %. The image contrast started to decrease for 114 LP/mm and dropped abruptly for structures lower than 5.5 µm $\hat{=}$ 181 LP/mm.

Lateral resolution limit. For the PM, the optical resolution is also lower than the optical space resolution, which is 1.33 µm/px. It was even possible to achieve a contrast of $MI = 80\,\%$ for a spatial frequency of 161 LP/mm. The determined maximal spatial frequency which is considered to be resolved according to the Rayleigh criterion, was $d_{\mathrm{xy,PM}} = 256\,\mathrm{LP/mm}$, which corresponded to an optical resolution limit of 3.9 µm.

Axial resolution. The calculation for the PM with the specified numerical aperture ($NA = 0.15$) of the lens resulted in a theoretical resolution according to Equation (3.4) of $d'_{\mathrm{xy,PM}} = 2.24\,\mu\mathrm{m}$ and a theoretical axial resolution of $d_{\mathrm{z,PM}} = 24\,\mu\mathrm{m}$.

Determining the focal plane is a crucial part for measurements with the PM. The measured mean intensity of the edge images showed a dependency on the chosen distance between the lens and specimen stage. For the manually determined optimal focal distance, the measured mean intensity of the

edge image was maximal (Fig. 3.18). As soon as the distance was larger or smaller than the manually determined optimal focal distance, the amount of detected edges diminished abruptly.
This procedure was further tested on 20 sections and the highest intensity in the edge image always corresponded to the manually determined distance for which the tissue was in focus.

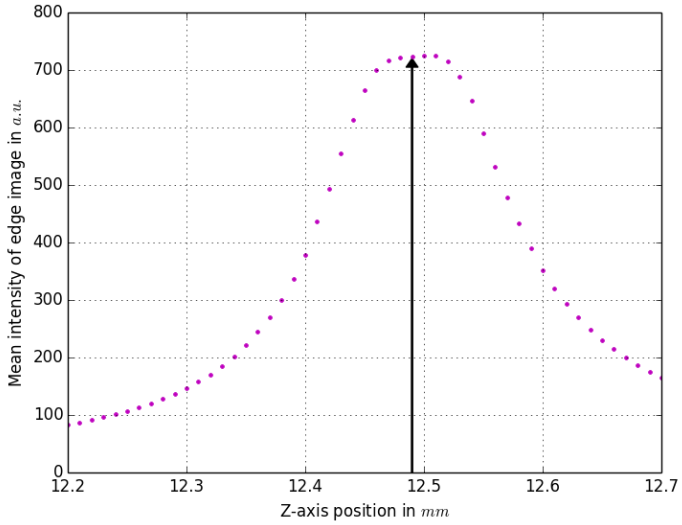

Figure 3.18: Focal distance. Variation of the z-axis position induced different mean intensities in the calculated edge images.

3.3.3 Discussion

3.3.3.1 Discussion LAP

The measured resolution is lower than the specifications for the employed detector and lens suggested. The resolution is limited rather by aberrations than by diffraction as the best results were achieved for large aperture sizes. If the resolution limit had been diffraction limited, fine structures would have been best resolved for small aperture sizes.
The fact that the resolution limit was only slightly improved by increasing the spatial sampling rate of the detector indicates that the optical resolution limit is not restricted by the detector, but by aberrations and scattering within the optical system. The polarization filters did not reduce the optical performance of the system as the same results were obtained when the filters

were removed from the light path. Thus, only aberrations of the lens and scattering within the system reduce the theoretically possible resolution.
While the lateral resolution was experimentally investigated, the axial resolution was calculated based on the results of the lateral resolution limit. A high depth of field is especially important to be able to tilt the specimen stage which is necessary to resolve the apparent sign ambiguity (Sec. 2.4.5) [39, 65]. Even though the depth of focus was only calculated and not experimentally verified, tilted images of tissue confirmed that the currently performed tilting with an angle of 8 °, which corresponds to a distance of 21 mm to the focal plane, still appear sharp. Thus, the depth of focus is sufficient for the evaluation of the sign of the nerve fiber orientation.
The employed "1951 USAF Resolution" testchart contains only a limited number of line pairs with different spatial frequencies. This reduced the accuracy with which the lateral resolution limit was assessed. The accuracy of the identification of the resolution limit and the critical aperture can be increased by employing a testchart containing a continuous spectrum of spatial frequencies. However, even if the accuracy of the determination of the lateral resolution limit is increased with such a testchart (e.g. Siemens star), this will not improve the accuracy of the determined fiber orientation. For the purpose of the characterization performed in this study, it was sufficient to determine the magnitude of the resolution limit and to compare it to the resolution limit of the PM. With the current setup, only the highest frequency which was considered resolved was measured, even though the structure was transferred with a higher contrast than 15.3 %.
The evaluation of the optimal exposure time was performed with a sufficient accuracy as the properties of different brains varies for example with age due to a decrease in myelination. The used brain tissue belonged to a patient who died in its seventies, thus being representative for the standard investigations performed in our laboratory. However, it would be desirable to determine the optimal exposure time for each investigated brain. Using the described approach this is easily possible. Still, the determined exposure time is a good reference value for the standard measurements performed in our laboratory.

3.3.3.2 Discussion PM

The evaluation of the lateral and axial resolution limit as well as the MTF were straight forward. The determined values are close to the values specified by the manufacturers as the identified resolution limit was similar to the physical limit given by the detector. The actual resolution limit was between 3.4 µm and 3.9 µm and could not be identified more accurately due to the discretization of spatial frequencies of the testchart. To determine the exact resolution limit, a testchart with a continuous spectrum of spatial frequencies is necessary. As already discussed for the LAP, such an investigation is not constructive for the investigated purpose.
Even though the resolution limit was close to the one theoretically proposed based on the datasheets of the lens and detector, it was decreased due to internal aberrations and diffractions in the system. Employing an objective lens with a higher numerical aperture, e.g. $NA = 1.5$ it is possible to realize a higher lateral resolution of $d_{xy} = 215\,\text{nm}$. Increasing the numerical aperture, has it advantages as well as disadvantages. On the one hand, it would be possible to resolve the fiber structures that cannot be resolved with the current setup in the x- and y- plane. On the other hand, the axial resolution would decrease, increasing the difficulty to determine the focal plane. It is problematic that for a low axial resolution only a small part of the section is in focus. The out-of-focus fibers are transferred unsharp contributing diffuse to the measured signal, causing an intensity offset in the measurement. Due to the diffuse influence of the out-of-focus fibers, the interpretation of the measured retardation and transmittance signals would become more complicated. Anyhow, the exact influence of a low depth of field has to be investigated in the future. Most of the time, a numerical aperture of the lens comes at the cost of a higher magnification, prolonging the measuring time considerably and increasing the amount of data extensively. For example, for a lens with a 10x-magnification and a numerical aperture of $NA = 0.3$, the lateral resolution, assuming an ideal detector, would increase to 1.1 µm, while at the same time,the measuring time and the amount of data would increase by a factor of four. Thus, instead 600 minutes and 700 GB data, it would take 2400 minutes and 2.8 TB data to measure a complete representative human section with this lens. So far, the current lens represents the optimal compromise between the advantages and disadvantages of a high quality polarization lens.

The developed semi-automatic approach to identify the z-position proved to be reliable and user-independent. The manually and automatically determined distance only varied by ±5 µm. 5 µm represents the limit for which the user is able to observe slight changes in structuring. For practical purposes, it is sufficient to roughly predetermine the distance for which the tissue appears to be in focus and then perform a z-scan as described previously. However, instead of covering a distance of 500 µm, it is sufficient to cover 100 µm in 5 µm-steps. A macro was implemented in *Fiji* to enable an automatic generation of the edge images and calculation of the mean intensity. Applying this macro, the observer is provided with the information about the z-position for which most edges are detected.
However, it is important that these measurements are performed in the white matter. The Sobel operator is a line detector and as such only detects linear structures which are present in the shape of fibers within the white matter, while the gray matter mostly contains oval shaped cells.

3.4 System Sensitivity for 3D-PLI Analysis

The evaluation of the sensitivity of the polarimetric setups is important to quantify the validity of the measurements. It has to be assessed whether the determined nerve fiber orientation is reproducible or whether the noise level is too high. By estimating how the noise level affects the measurements, it will be possible to elicit the statistical error of the determined fiber orientation.

3.4.1 Materials and Methods

The assessment of the response of the systems to birefringent signals includes a modified Opto Electronic Conversion Function (OECF), the signal-to-noise ratio (SNR), and the reproducibility of the measured fiber orientation. In general, the OECF describes the performance of an optical system regarding the correlation of a given optical input signal and the electrical output signal. It is specified in the ISO standard 'ISO 14524' [66]. As the investigated setups rely on the analysis polarized light for imaging purposes, instead of measuring the response of the systems to samples with a known optical density, samples inducing different states of polarization were selected for this assessment.
As the analysis of the fiber orientation in brain tissue is based on the analysis of the state of polarization, it is important to investigate the signal response of the given polarimetric imaging systems with respect to known polarization states. It is ensured that the imaged sample is homogeneous to avoid possible partial volume effects. This newly developed approach to evaluate the systems response with respect to known states of polarization will be referred to as the Polarization Electronic Conversion Function (PECF).
Furthermore, it is important to quantify the validity of the measurements. The signal-to-noise ratio represents a suited measure. If the SNR is too low, the measured signals would be unreliable as the measured value would greatly fluctuate due to noise. The SNR compares the level of the desired signal to the level of the unwanted background noise. Traditionally, the SNR is defined as:

$$SNR = \frac{\mu_{\text{sig}}}{\sigma_{\text{sig}}}, \tag{3.7}$$

with μ_{sig} and σ_{sig} corresponding to the average signal value and the standard deviation of the signal, respectively. Within digital imaging, different kinds of noise such as dark current noise and shot noise exist. Shot noise, also referred to as photon noise, has its origin in the statistical generation and detection of photons. This kind of noise depends on the intensity of light. Its distribution is described by a Poisson distribution: $\text{SNR} = \frac{N}{\sqrt{N}}$, with N being the number of photons. In contrast, the dark current noise is uniformly distributed. It is caused by the relatively small electric currents that flow through semiconductors and is especially relevant for very small signal strengths. In this study only the net effect of the different noise sources is investigated.

Of special interest is the reproducibility of the determined fiber orientation. The term "reproducibility" describes the stability of the imaging system with regards to the reconstructed fiber orientation. It is affected by the signal fluctuations caused by the detector noise and the variations in the illumination. The inhomogeneities of the filters influence the measured signal with respect to the transparency and the polarization efficiency. Due to the filter inhomogeneities, the reconstructed fiber orientation might depend on the position of the fiber of interest with regards to the object plane. Additionally, the image post-processing that enables a 3D reconstruction of the consecutive sections, induces signal interpolations. The interpolation leads to undesired changes of the measured signal, decreasing the accuracy of the determined nerve fiber orientation.

The reproducibility and accuracy of the determined in-plane direction and the out-of-plane inclination angle is investigated. The accuracy of the direction angle can be directly measured, while the reproducibility and accuracy of the inclination angle can only be determined indirectly by employing Gaussian error propagation. The measured fluctuation of the retardation value (Δr) is propagated to the uncertainty of the inclination angle ($\Delta\alpha$) according to:

$$\Delta\alpha = \sqrt{\left(\frac{\partial\alpha}{\partial r} \cdot \Delta r\right)^2}. \tag{3.8}$$

The differentiation of Equation (2.24) yields:

$$\begin{aligned}\frac{\partial\alpha}{\partial r} =& \frac{-t_{\text{rel}}}{2\cdot\sqrt{1-r^2}\cdot\sqrt{\frac{\pi}{2}-t_{rel}\cdot\arcsin(r)}\sqrt{t_{\text{rel}}\cdot\arcsin(r)}} \\ =& \frac{-1}{2\cdot\sqrt{1-r^2}\cdot\sqrt{\frac{\pi}{2}-\arcsin(r)}\cdot\sqrt{\arcsin(r)}},\end{aligned} \tag{3.9}$$

with $t_{\text{rel}} = 1$.
It is expected that the accuracy of the determined direction angle greatly decreases for small signal modulations as it is the case for steep fibers.

PECF. In order to analyze the signal response with respect to different states of polarization, a linear polarizer and a quarter-wave retarder, similar to the ones employed in the LAP, were combined and the angle (B in Eq. (3.10)) between the two filters was varied as shown in Figure 3.19 A. The variation of the angle influenced the polarization state of the light from circular to elliptical polarization. The ellipticity of the indicatrix was directly correlated to the angle between the linear polarization filter and the wave retarder. Thus, it enables a controlled investigation of the signal response of both systems regarding different states of polarization. Usually, the orientation of fibers within the tissue sample induces elliptically polarized light with different orientations, but it is not possible to control the influence of the tissue on the circularly polarized light. Hence, the combination of the two filters enables the simulation of the effect that the brain tissue has on the incident light. Furthermore, the comparison of the response of both polarimetric systems neglecting resolution effects was possible as the filters are considered as homogenous in comparison with the usually investigated brain tissue.
The relation between the measured intensity and the angle B between the two non-fixed filters, the retardance Γ_1 of the fixed retarder and Γ_2 the retardance of the non-fixed retarder can be calculated using the Jones matrix

calculus [47, 48] (see Appendix A.2). The calculation yields:

$$
\begin{aligned}
&I_{T,\mathrm{PECF}}(\Gamma_1, \Gamma_2, \rho, B) \\
&= \sin^2(\Gamma_1) I_{0T,\mathrm{PECF}}^2 \Bigg[\sin^2(\Gamma_2) \Bigg(-\frac{1}{2} \sin(2\rho) \sin(4B) + \cos^4(\rho) \sin^2(2B) \\
&+ \sin^4(\rho) \cos^2(2B) \Bigg) + \sin^4(\rho) \cos^2(\Gamma_2) + \frac{1}{4} \sin^2(2\rho) \Bigg]. \qquad (3.10)
\end{aligned}
$$

The derived equation describes the intensity change depending on the retardances Γ_1 and Γ_2 of the two implemented retarders, the rotation angle ρ of the linear polarizer, and the angle B between the retarder and the linear polarizer that constitute the PECF-sample.
As the signal is symmetric, all angles are mapped into the range between $45\,^\circ$ and $90\,^\circ$ (see Fig 3.19 B). The theoretically expected retardation was calculated and compared with the measured retardation signal.

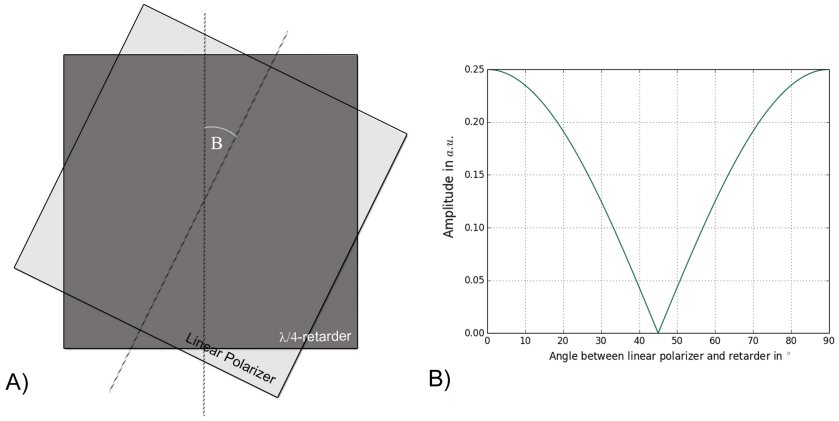

Figure 3.19: Sample for the PECF measurement. The variation of the angle (B) between the linear polarizer and the quarter-wave retarder resulted in light with different states of elliptically polarized light. For example, for an angle of $B = 45\,^\circ$ circularly polarized light was created, resulting in an amplitude of 0.

SNR. In order to investigate the influence of the photon noise, 100 empty images were measured (with $\rho = 0\,^\circ$) and analyzed with respect to the transmitted signal and the standard deviation. Only the net noise was measured and the theoretical SNR was calculated according to Equation (3.7).
To determine the influence of the SNR on the measurement of the fiber orientation, the same ROI containing fibers with multiple orientations were measured using the standard procedure. The ROI was measured 50 times to gain significant results. The measurements were calibrated and the direction

angle, the transmittance, and the retardation were calculated according to Equation (2.16). As the sample was fixed in the sample holder, a registration of the measurements was not necessary. Each modality was evaluated separately. The 50 maps containing the direction angle were averaged and the standard deviation from this average map was calculated. The standard deviation contains the information about the reproducibility of the measured fiber orientation. This procedure was also realized for the transmittance and the retardation. Based on Equation (3.9) the error of the inclination angle was calculated.

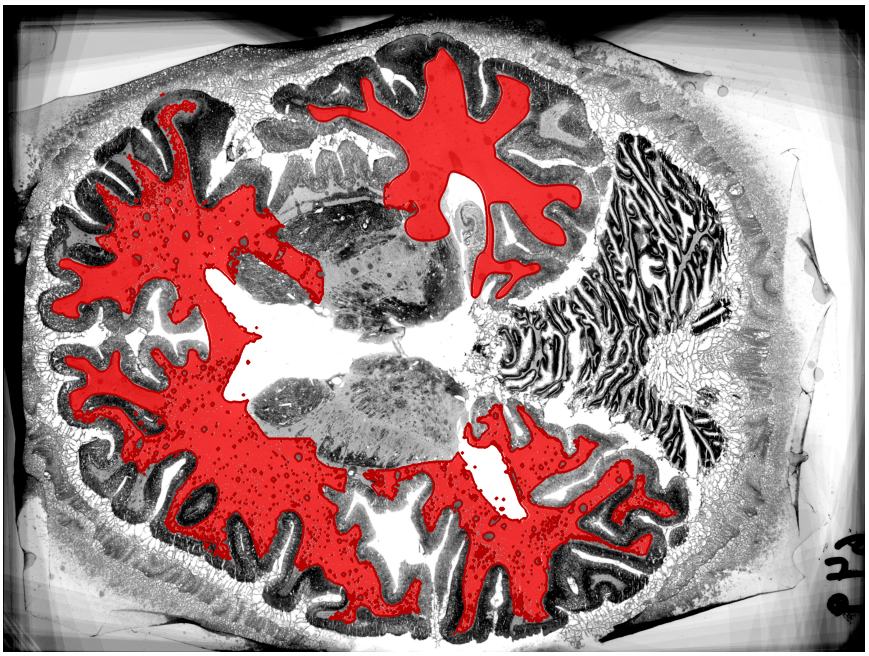

Figure 3.20: SNR and reproducability. The red area of the imaged brain section represents the analyzed ROI for the measurements of the SNR and the reproducability.

Reproducibility. For the reproducibility measurements, the same sample was measured multiple times. Before each standard measurement, the brain section was removed from the sample holder and placed back into the setup. This procedure ensured that the section was measured at different positions. The measurements were calibrated and registered. Afterwards, the direction angle, the transmittance, and the retardation were calculated. For each modality, the average and standard deviation for each pixel were calculated.

3.4.1.1 LAP specific

The employed AxioCamHRc in the LAP has a specified dynamic range of typically $> 1:2200$ at 25 MHz at a read-out-noise of 7.7 electrons. And for 12.5 MHz a read-out-noise of 6.8 electrons of $> 1:2500$. The full well capacity is typically 17.000 electrons and the dark current 0.7 electrons/px/s.
To quantify the noise of the detector and the illumination source affecting tissue measurements, a representative brain section was inserted into the sample holder. The section was selected to likely contain fibers with all possible direction and inclination angles to enable a thorough analysis. Without moving the section, 50 standard measurements were performed and the actual SNR was calculated.
For the reproducibility of the LAP assessment, the same section was imaged 50 times, but the section was removed after each measurement and placed back into the polarimeter. For 30 measurements the sample was placed with a slightly different angle ($-5\,^\circ < \rho_{\text{sample}} < 5\,^\circ$), 15 times the angle was varied up to $\pm 20\,^\circ$ and five times the sample was rotated by $180\,^\circ$. The measurements were calibrated, registered with a rigid transformation, the different modalities (retardation, direction, transmittance) calculated and evaluated. In this case, as illustrated in Figure 3.20, only the white matter was investigated.

3.4.1.2 PM specific

The implemented Retiga-4000R from *QIMAGING* is a high sensitivity camera with an implemented CCD chip. It has a high sensitivity, high dynamic range, large well capacity of 40.000 electrons, and low dark current noise of 1.64 electrons/px/s.
To measure a whole brain section 50 times (as done for the LAP) was not practical due to the extensively long measurement times of the PM. The standard measurement of a complete brain section with the microscope takes up to 10 h and about 750 GB of data is produced. Thus, to measure the section 50 times, 500 h are necessary and afterwards 37.5 TB have to be processed and analyzed. Therefore, only a single tile containing white matter was imaged 50 times in order to get an estimate of the noise level.
The reproducibility measurements were not performed with the PM as the practical realization of the reproducibility measurements was not possible

and not necessary. The homogeneity level of the illumination greatly exceeds the one of the LAP and the filters are of a higher quality.

3.4.2 Results

3.4.2.1 Results LAP

PECF. The measured Polarization Electronic Conversion Function revealed significant differences between both systems. Varying the angle between the two filters resulted in different signals, which were analyzed according to Equation (3.10). The measured amplitudes of the LAP (red triangles in Fig. 3.21) were always higher than theoretically expected for a light retardance of a quarter wavelength (green line). Instead, seemed the measurements of the LAP to be correlated to a larger light retardance of about $142/529\lambda$ (yellow line). Still, most measurements with the LAP were slightly lower than expected for this retardation.

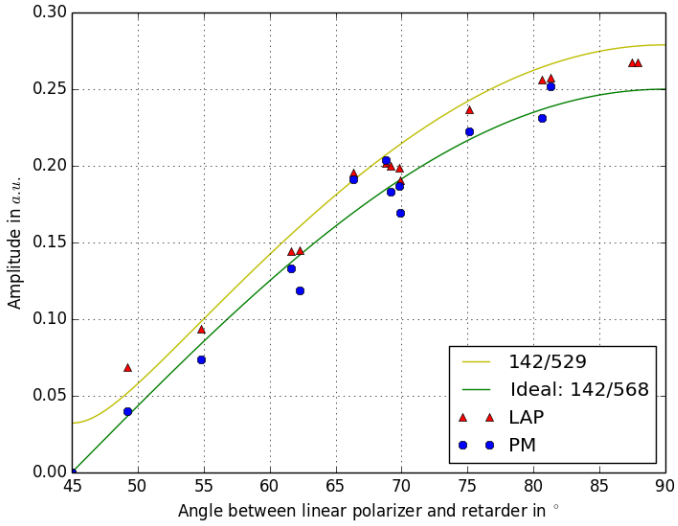

Figure 3.21: PECF measurements. The variation of the angle between the linear polarizer and retarder induced different signal responses in the LAP and the PM.

SNR. The noise level of $\sigma_{\mathrm{I,LAP}} = 58 \pm 10$ was not influenced by introducing a specimen into the path of light. The noise level of the transmitted light obviously decreased with increasing light intensity (Fig. 3.23 A) and had a $1.5\sqrt{N}$ dependency on the incident light intensity, where N is the number of counts.

In contrast, the noise level of the determined direction angle was constant and independent from the in-plane orientation of the imaged nerve fiber (Fig. 3.23 C). The image noise affected every angle uniformly and decreased the accuracy of the determined angles by $\sigma_{\varphi,\mathrm{LAP}} = (0.306 \pm 0.08)^\circ$ (Fig. 3.23 D). Only 24 % of the imaged pixels had a standard deviation larger than 1 °. Large inaccuracies in determining the in-plane angle mostly occurred for low amplitudes (Fig. 3.24). Especially for retardation values smaller than $r = 0.5$, the noise level increased significantly and deviations up to 20 ° of the determined direction angle were possible. For higher retardation values ($r \geq 0.8$), the determination of the direction angle was most accurate.
The fluctuation in intensity also influenced the determined retardation. The noise level was nearly constant for all measured retardation values, even low retardation values were hardly affected. Only for retardation values higher than $r > 0.5$ (Fig. 3.23 E) the influence of the noise slightly decreased. In general, the noise only affected the determined retardation value of about $\sigma_{r,\mathrm{LAP}} = 0.008 \pm 0.002$ (Fig. 3.23 F).
The error of the inclination assuming a constant error of 0.008 of the retardation is according to Equation (3.9), maximally 1.5 ° for flat fibers and up to 3.3 ° for steep fibers (cp. Fig. 3.22, red line).
Reproducibility. The measured deviations of the direction and retardation caused by the replacing of the sample were increased as compared to the noise measurements. Even though the images were registered, the variations of the direction angle of the imaged nerve fibers increased from $\sigma_{\varphi,\mathrm{fixed}} = (0.306 \pm 0.08)^\circ$ to $\sigma_{\varphi,\mathrm{moved}} = (0.72 \pm 0.4)^\circ$ (Fig. 3.25). For the fixed position only about 24 % of all analyzed pixels containing fibers had a standard deviation above 1 °, for the reproducibility measurements this was true for about 62 % of all analyzed pixels.
The spatial position and interpolation artifacts of the registration procedure hardly influenced the measurement of the retardation. The peak standard deviation is not affected by the moving of the section: $\sigma_{r,\mathrm{fixed}} = 0.008 \pm 0.002$ to $\sigma_{r,\mathrm{moved}} = 0.008 \pm 0.003$. But still for the reproducibility measurements higher standard deviations occurred (Fig. 3.25 B, blue curve).

3.4.2.2 Results PM

PECF. For the PM, the assumed light retardance of a quarter wavelength describes the measurements of the PECF sample best (Fig. 3.21, blue cir-

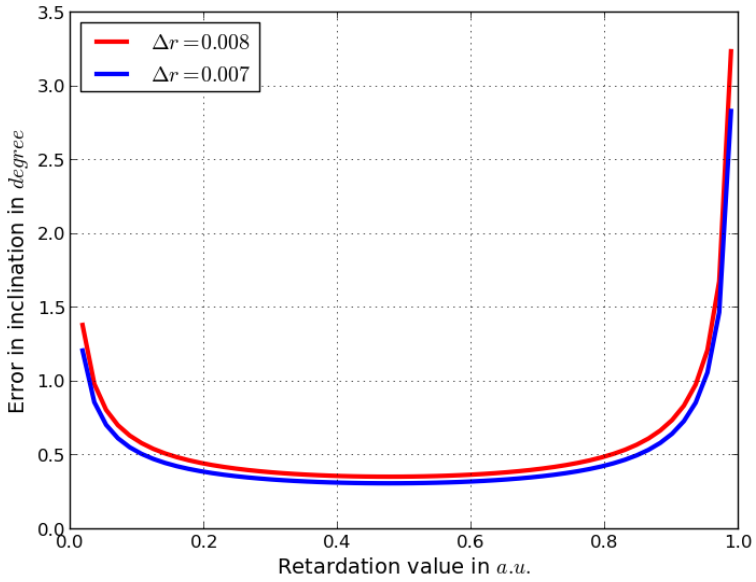

Figure 3.22: Error of the inclination angle. The error of the inclination angle depends on the measured retardation signal and the measured accuracy of the retardation signal which is for the LAP $\sigma_{r,\mathrm{LAP}} = 0.008$ and for the PM $\sigma_{r,\mathrm{PM}} = 0.007$.

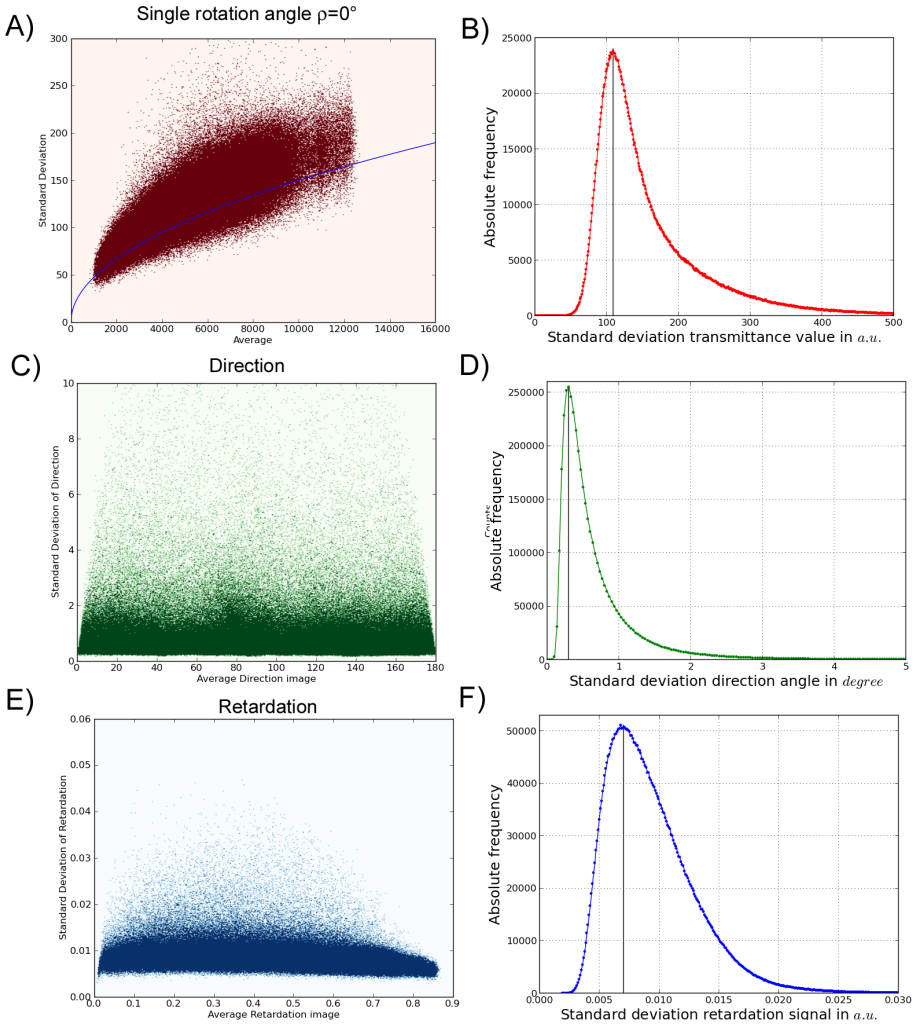

Figure 3.23: SNR measurements of LAP. Correlation between the measured average value of the transmittance signal (A+B), the direction angle (C+D), the retardation (E+F), and the respective standard deviation.

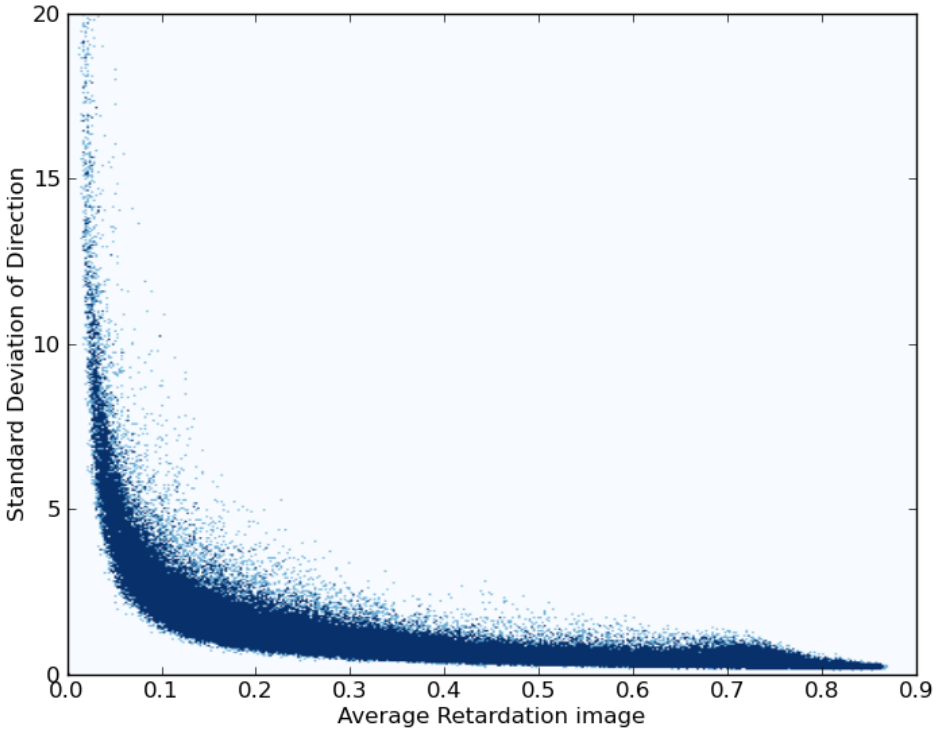

Figure 3.24: Accuracy of the direction angle for LAP. Dependency of the standard deviation of the direction angle on the retardation value.

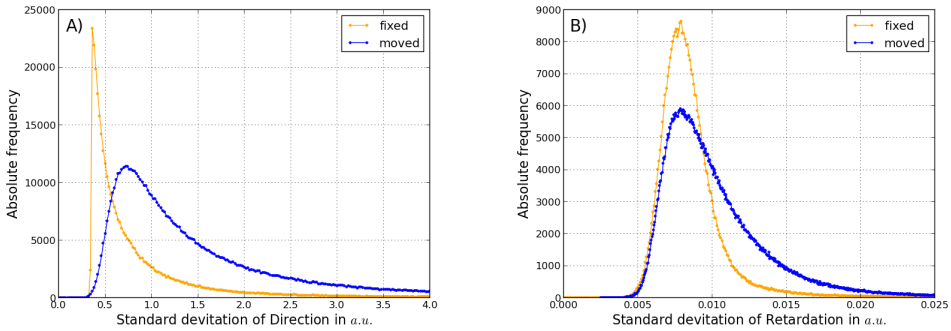

Figure 3.25: Comparison of SNR and reproducibility measurements for the LAP. The standard deviation distribution of the measured direction angle (A) and retardation (B) is broader for the reproducibility measurement than for the SNR measurement.

cles). The measured values are slightly scattered around the theoretically predicted values. However, there is no clear shift to lower or higher values apparent.

SNR. The measurement of a single tile only provides an estimate of the actual SNR when imaging brain tissue. The transmittance signal of the imaged section is lower than a $1.5\sqrt{N}$-dependency of the noise level. The assumed fluctuation was rather limited by the $1.5\sqrt{N}$-dependency, as the majority of all measured standard deviations was lower (Fig. 3.26 A). The measured intensity value has a standard deviation of $\sigma_I = 4.1$ a.u.

The standard deviation of the measured direction angle is also low with a mode value of $\sigma_{\varphi,PM} = 0.29\,^\circ$ (Fig. 3.26 D). The fibers in the imaged tile contain a predominant direction of $\varphi = 120\,^\circ$, which is visible when observing the scatterplot (C) as well as the actual transmittance image (see Appx. A.5, Fig. 2). The accuracy of the measured values is $\sigma_{r,PM} = 0.007$ for the PM measurements (F), resulting in a maximal error of the inclination angle of $2.8\,^\circ$ for very steep fibers (cf. Fig. 3.22, blue line).

3.4.3 Discussion

3.4.3.1 Discussion LAP

The measurement of the PECF revealed that the mismatch of the wavelength of the retarder and the illumination have to be taken into account

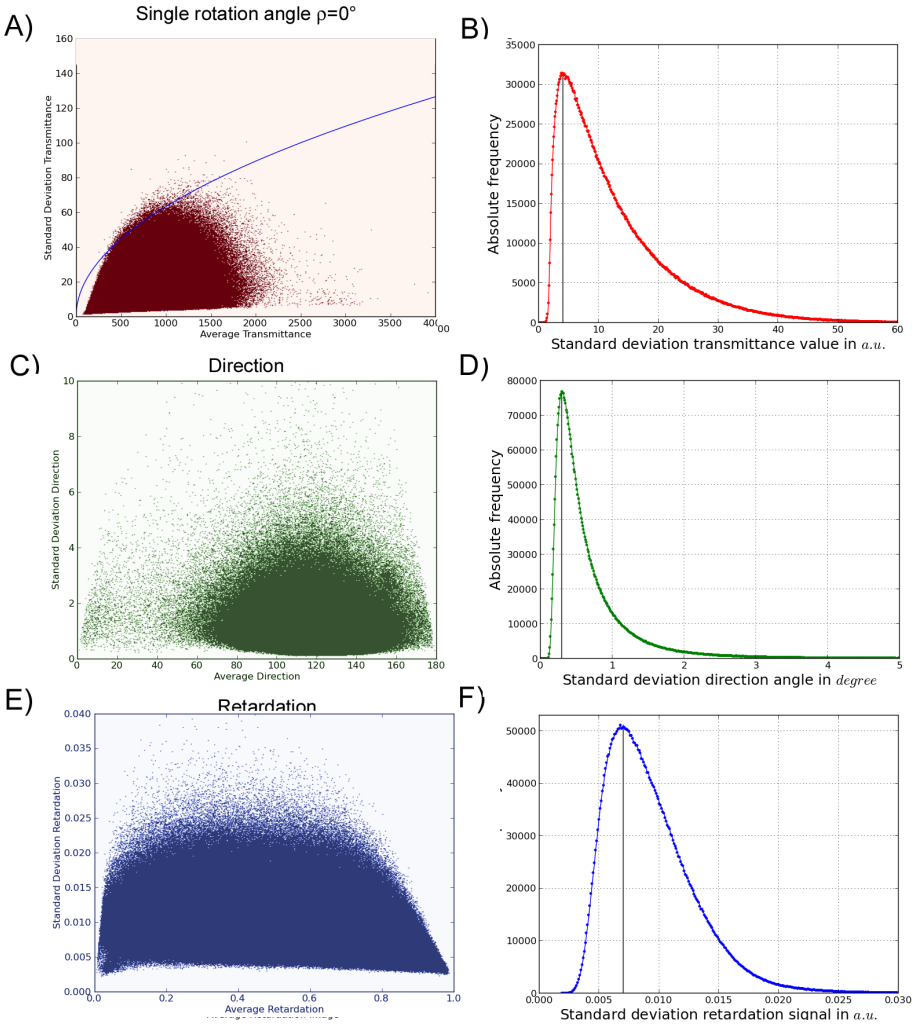

Figure 3.26: SNR measurements of PM. Correlation between the measured average value of the transmittance signal (A+B), the direction angle (C+D), the retardation (E+F), and the respective standard deviation.

when analyzing the measurements of postmortem brain tissue. The lower than expected amplitude for all angles between the filters was caused by a slightly lower retardance of the light than $142/529\lambda$ (cf. Fig. 3.21). Thus, the assumption that the retarder worked like a true zero-order retarder was confirmed. The slight aberrations towards smaller values were due to the asymmetrical spectrum (Fig. 3.4). More specifically, the spectrum is positive skewed with the mass of the photons having longer wavelengths than the peak wavelength. High frequencies are retarded less than $142/529\lambda$, causing lower signal amplitudes. Due to the theoretical symmetry of the signal, the measurements performed with an angle variation of $0° < B < 90°$, were mapped into the range of $45\,° < B < 90\,°$. However, if the sheet filters are not working symmetrically, aberrations could be induced.

It would be interesting to increase the sampling rate between $45\,° < B < 55\,°$ to investigate the system response to very small amplitudes which occurred in tissue with a low birefringence as such is the case for crossing or steep fibers in brain tissue. In this case, the noise level should negatively affect the amplitude measurement such as it was the case for $B = 49\,°$.

The SNR measurement showed that the measured light intensity was indeed Poisson distributed as expected. However, the noise was higher than theoretically expected when the only relevant noise source would have been photon noise. The higher noise level is introduced by internal signal amplification in the camera, amplifying not only the desired signal but also the noise level.

The observation of the influence of the noise of the direction angle met the expectations. The in-plane orientation of the angle only influenced the phase of the sinusoidal signal. Thus, for a given inclination angle, resulting in a certain amplitude, it was expected that the noise level is independent of the in-plane direction angle.

All measured retardation values were equally affected by the fluctuation of the incident light. In average, each sinusoidal signal encountered a similar intensity fluctuation. For example, for a large amplitude ($\Rightarrow$ high retardation values), the influence of photon noise on the highest intensity is maximal and for the lowest value, it is minimal, resulting in a medium noise level for the complete amplitude.

Overall, the statistical variation of r and φ are due to the photon noise of the set up.

3.4.3.2 Discussion PM

Some minor aberrations of the measured signal amplitude to the theoretically proposed exist. The same considerations regarding the used PECF-sample as discussed for the LAP have to be made for the PM.
However, apart from the slight deviations, the assumption that the implemented retarder and the illumination wavelength are well matched, was confirmed. The imaging of an area of 2.7×2.7 mm^2 is sufficient to estimate the accuracy of the determined fiber direction and light retardance as expected. Still, to confirm that the accuracy of the fiber direction is independent of the in-plane angle, as observed for the LAP, a larger area containing fibers with in-plane angles between $0\,^\circ$ and $180\,^\circ$ is necessary. Also a broader variety of transmittance signals are desirable to determine the actual dependency of the noise. Nevertheless, the measurements were completely sufficient to evaluate the accuracy of the measured fiber orientation and the influence of the noise.

3.5 Comparision of LAP and PM

The evaluation of the system properties of the two polarimetric systems revealed great differences and provided the opportunity to increase the accuracy of the measured signals for an improved evaluation of the fiber orientation in postmortem brain tissue.

Property	LAP	PM
Illumination		
time until thermal stability	43 min	2 min
peak wavelength	(529 ± 17) nm	(550 ± 4.5) nm
inhomogeneity level	9.58 %	5.4 %
SNR	58	108
inhomogeneity polarizer	2.20 %	-
inhomogeneity analyzer	2.28 %	-
inhomogeneity retarder	1.52 %	-
Polarization effects		
PER	2.2027	-
η_p	99 %	-
pol. sensitive camera	yes	-
Imaging resolution		
object space resolution	64 µm/px	1.33 µm/px
d_{xy}	159 µm	3.9 µm
d_z	163 mm	24 µm
System sensitivity		
σ_I	$1.5\sqrt{N}$	$< 1.5\sqrt{N}$
σ_φ	$(0.306 \pm 0.08)\,^\circ$	$0.29\,^\circ$
σ_r	$(0.008 \pm 0.002$	0.007
field of view	(25×25) mm^2	(2.7×2.7) mm^2
working wavelength retarder	568 nm	545 nm
acquisition time (per section)	15 min	2400 min
data	2 GB	750 GB
sign determination	yes (tiltable stage)	no

Table 3.3: Comparison of system properties between the LAP and the PM.

In Table 3.3, the main results of the performed measurements for the LAP and the PM are listed.
The polarizing microscope represents an almost ideal system in terms of analyzing birefringent samples. The peak wavelength of the LED and the optimal working wavelength of the retarder are nearly perfectly matched,

resulting in an exemplary analysis of brain tissue samples. The implemented Koehler illumination - yields together with the calibration procedure - a homogeneous illumination. Apart from the newly implemented semi-automatic identification of the focal distance, no further optimizations were necessary to improve the system performance of the PM.
In contrast, the characterization of the LAP provided the opportunity to improve the system's performance. For instance, a water-cooling was implemented into the LED panel and the critical aperture as well as the optimal exposure time were determined.
Even though the PM is superior to the LAP with respect to the illumination homogeneity and the optical resolution, the reliability of the measured fiber orientation is similar for both systems .

3.6 Influence of the System Properties on the Investigation of the Nerve Fiber Orientation

All in all, the characterization and optimization of the polarimetric systems provided a deeper knowledge regarding the influence of the system properties on the investigation of the orientation of nerve fibers. Any fluctuations, inhomogeneities or changes in the illumination intensity, either caused by the LEDs or the filters, directly influence the transmittance signal, thus complicating the interpretation of the gained transmittance signals. The implementation of the water-cooling into the LED panel of the LAP together with the calibration procedure enable the sensible assessment of the transmittance signal. The phase ($\Rightarrow$ direction angle) and the relative amplitude ($\Rightarrow$ inclination angle) of the measured sinusoidal signal are not affected. In case of the retardation, only the relative intensity changes due to the birefringent tissue are relevant, making the retardation independent of light intensity changes. Only sudden, significant intensity changes would negatively influence the measurement of the signal amplitude and the phase. This is not the case, the intensity only changes gradually over time. Thus, when analyzing the orientation of nerve fibers, the influence of intensity fluctuations is neglectable.

For the LAP, it is critical that the peak wavelength differs greatly from the optimal working wavelength of the retarder. Even though polymer retarders are considered to act like zero-order waveplates [58, 67], it is likely that the wavelength mismatch of $\Delta\lambda_{\mathrm{LAP}} = 39\,\mathrm{nm}$ causes the optical path difference to be longer than $\Delta n \cdot t = \lambda/4$. This difference of the optical path difference results in elliptically instead of circularly polarized light. The exact specifications of the implemented retarder are not known, but it is very likely that the retarder shows a similar behavior typical for polymer retarders (depicted in Fig. 3.11). Thus, the incident light is not retarded by a quarter of wavelength but rather by $142/529\lambda$. The PECF measurements confirm that this is indeed the case. The current approach assumes an exact retardance of the light of $\lambda/4$ causing misinterpretations of the measured signal. Thus, when describing the LAP with the Jones matrix calculus an optical path difference of $\gamma = 142/529 \cdot \lambda$ in Equation (2.8) has to be considered. So far, no retarder could be ordered that provides a quarter-wave retardance for the LAP setup. A possible approach to experimentally correct the mismatch of

the wavelength is to mount a suited bandwidth filter in front of the camera lens to ensure that only light that matches the working wavelength of the retarder is evaluated.
Another critical result of the characterization is that the linear polarization filters have a reduced polarization efficiency, thus the measurements are performed with partially polarized light. It has to be clarified whether the description using the Mueller calculus could significantly improve the results as partially polarized light is considerable with this calculus. Both formalisms are suited and commonly used to describe the interaction of polarized light with elements that change the state of polarization. The Jones matrix calculus is derived from the mathematical description of the phase and amplitude of light and assumes completely polarized light. The Jones matrices have simpler properties and their interpretations are easily accessible. In contrast, Mueller matrices are more complex, but can represent depolarization [68]. Assuming fully polarized light, the Jones and Mueller formalisms merge. But as the measurements revealed about 1% of the incident light is not completely polarized, the influence of the partially polarized light and the analysis with the Mueller formalism should be addressed in future studies.
Identifying the critical aperture and the optimal exposure time was important to provide the best possible transfer of the imaged structure into the object space. The optical resolution directly influences the in-plane partial volume effect. Because of the limited resolution and the pixel size, the signals of multiple fibers are averaged and the total measured retardation signal is expected to drop.
The optimal exposure time of 80 ms ensures the best possible transfer of the signal without a lower than necessary image contrast and without a saturation of the signal. An overexposure as can be observed for longer exposure times results in a saturated signal, thus in a lower retardation. This induces a wrong conclusion about the inclination of the imaged nerve fibers. However, the exposure time of 80 ms is only optimal for a section thickness of 70 µm. If the local myelination is lower, which might be caused by brain aging effects or variations of section thickness, a higher exposure time could be optimal. Thus, for each brain, an individual determination of the optimal exposure time should be performed.
The shot noise affects the determination of the retardation and the phase

similarly. The direction angle can be measured with a high accuracy. However, the accuracy of the direction angle depends to some extend on the amplitude of the measured signal. Low amplitudes, for example, caused by steep fibers, increase the difficulty to measure the phase of the signal. Especially for very steep fibers, the accuracy of the measured inclination and direction angle decrease dramatically.
Deviations of the retardation value are nearly independent of the intensity value. The deviations are especially uncritical for flat fibers. However, it is critical that the accuracy of the retardation signal is about the same magnitude as signals within low myelinated areas such as gray matter, making the determination of the fiber orientation very difficult.
In general, the direction angles can be determined with a higher accuracy $\sigma_\varphi << 1^\circ$ than the inclination angle. Thus, increasing the accuracy of the determined fiber inclination angle is of a high importance.

Chapter 4

Accomplishment of a Multiscale Analysis with 3D-PLI

The previous chapter focused on the characterization and optimization of the employed polarimetric systems. It was shown that the measured signal intensity is influenced by certain properties of these systems. These properties comprise the lateral resolution, the polarization efficiency, the matching of the retarder wavelength with regards to the illumination wavelength, and the illumination wavelength itself. The conducted PECF experiments revealed that a measurement of the same homogeneous birefringent sample results in different signal responses from the two systems. The fact that the signal responses differ is problematic as for the realization of a multiscale analysis of the fiber architecture of the human brain, it has to be ensured that the same fiber orientations are measured with both systems . Hence, when interpreting the measured signals the influence of the relevant system properties has to be considered.
Within this chapter a modification of the current 3D-PLI analysis (→ Chap. 2) is developed, considering the influence of the wavelength discrepancy observed in measurements with the LAP. Furthermore, the influence of the different resolutions of both systems is taken into account when interpreting the measured signal. Subsequently, the proposed compensation approaches that are intended to enable a multiscale analysis of the nerve fiber architecture are validated by employing a fiber model.

4.1 Theoretical Considerations of the Influence of System Properties

4.1.1 Influence of the Wavelength Discrepancy

The measurements of the light spectrum and the PECF of the LAP (see Secs. 3.1 and 3.4) revealed that the phase shift between the extraordinary and the ordinary ray differs from the assumed quarter-wave retardance. So far, for the theoretical description of the 3D-PLI analysis the induced path difference between the ordinary and the extraordinary ray was assumed to be $\lambda/4$ (cp. Eq. (2.15)). The differing retardance is considered by adapting the theoretical, mathematical description of the 3D-PLI measurements. For this purpose, the Jones matrix that describes a retarder with an arbitrary retardance is used instead of the matrix for a quarter-wave retarder to derive the correct description of the used setup. A more detailed derivation of the effects induced by an arbitrary retardance is given in Appendix A.3. Replacing the matrix describing the quarter-wave retarder with a retarder that induces an arbitrary phase shift of Γ in Equation (2.13) results in:

$$
\begin{aligned}
\vec{E_T}' =& P_y \cdot M_{\text{fiber}}(\delta,\beta) \cdot M'_{\text{ret}}(\Gamma) \cdot \vec{E}_x \\
=& \begin{pmatrix} 0 & 0 \\ 0 & 1 \end{pmatrix} \cdot \begin{pmatrix} \cos\left(\frac{\delta}{2}\right) + \mathrm{i}\sin\left(\frac{\delta}{2}\right)\cos(2\beta) & \mathrm{i}\sin\left(\frac{\delta}{2}\right)\sin(2\beta) \\ \mathrm{i}\sin\left(\frac{\delta}{2}\right)\sin(2\beta) & \cos\left(\frac{\delta}{2}\right) - \mathrm{i}\sin\left(\frac{\delta}{2}\right)\cos(2\beta) \end{pmatrix} \\
& \cdot \begin{pmatrix} \cos(\Gamma) & -\mathrm{i}\sin(\Gamma) \\ -\mathrm{i}\sin(\Gamma) & \cos(\Gamma) \end{pmatrix} \cdot \begin{pmatrix} E_x \\ 0 \end{pmatrix} \\
\overset{A.3(8)}{=}& \Bigg[\underbrace{\left(\cos(\Gamma)\sin\left(\frac{\delta}{2}\right)\sin(2\beta) - \sin(\Gamma)\cos\left(\frac{\delta}{2}\right) \right)}_{\text{Im}} \cdot \mathrm{i} \\
& \underbrace{- \sin(\Gamma)\sin\left(\frac{\delta}{2}\right)\cos(2\beta)}_{\text{Re}} \Bigg] E_x \vec{e}_y
\end{aligned}
\tag{4.1}
$$

The measured light intensity corresponds to the absolute square of the electric field vector ($I'_T \sim |\vec{E}'_T|^2$):

$$\begin{aligned} I'_T \sim |\vec{E_T}'|^2 =& \mathrm{Re}^2\left(\vec{E_T}'\right) + \mathrm{Im}^2\left(\vec{E_T}'\right) \\ \overset{A.3(9)}{=}& \left[\frac{1}{2}\sin^2\left(\frac{\delta}{2}\right) - \frac{1}{2}\sin^2\left(\frac{\delta}{2}\right)\cos(4\beta) + \sin^2(\Gamma)\cos^2\left(\frac{\delta}{2}\right) - \frac{1}{2}\right. \\ & \left. \cdot \sin(2\Gamma)\sin(\delta)\sin(2\beta) + \sin^2(\Gamma)\sin^2\left(\frac{\delta}{2}\right)\cos(4\beta)\right] I'_{0T}. \end{aligned} \tag{4.2}$$

By replacing the angle β with $\rho - \varphi$ in Equation (4.2) the dependency of the measured light intensity from the filter rotation angle ρ, the in-plane direction angle φ, the phase shift induced by the fiber δ and the retardance Γ induced by the employed retarder can be derived:

$$\begin{aligned} I'_T \overset{A.3(10)}{=}& \left[\frac{1}{2}\sin^2\left(\frac{\delta}{2}\right) + \sin^2(\Gamma)\cos^2\left(\frac{\delta}{2}\right)\right. \\ & + \frac{1}{2}\sin(2\Gamma)\sin(\delta)\sin(2\rho)\cos(2\varphi) \\ & - \frac{1}{2}\sin(2\Gamma)\sin(\delta)\sin(2\varphi)\cos(2\rho) \\ & - \frac{1}{2}\sin^2\left(\frac{\delta}{2}\right)\sin(4\varphi)\sin(4\rho)\cos(2\Gamma) \\ & \left. - \frac{1}{2}\sin^2\left(\frac{\delta}{2}\right)\cos(4\varphi)\cos(4\rho)\cos(2\Gamma)\right] I'_{0T}. \end{aligned} \tag{4.3}$$

Using a discrete Fourier analysis, Equation (4.3) is parameterized. Thus the Fourier analysis is expressed by:

$$I'_T(\rho) = a'_0 + a'_1\sin(2\rho) + b'_1\cos(2\rho) + a'_2\sin(4\rho) + b'_2\cos(4\rho), \tag{4.4}$$

with

$$
\begin{aligned}
a'_0 =& \frac{I'_{0T}}{2}\sin^2\left(\frac{\delta}{2}\right) + I'_{0T}\sin^2(\Gamma)\cos^2\left(\frac{\delta}{2}\right),\\
a'_1 =& \frac{I'_{0T}}{2}\sin(2\Gamma)\sin(\delta)\cos(2\varphi),\\
b'_1 =& -\frac{I'_{0T}}{2}\sin(2\Gamma)\sin(\delta)\sin(2\varphi),\\
a'_2 =& -\frac{I'_{0T}}{2}\cdot\cos(2\Gamma)\sin^2\left(\frac{\delta}{2}\right)\sin(4\varphi),\\
b'_2 =& -\frac{I'_{0T}}{2}\cos(2\Gamma)\sin^2\left(\frac{\delta}{2}\right)\cos(4\varphi).
\end{aligned}
$$

The used convention of the discrete Fourier analysis is in accordance with the convention introduced by Axer et al. [39].
The determined Fourier coefficients differ from the ones determined for a light retardance of $\delta = \pi/2$ (cf. Eqs. (2.18) to (2.20)). The calculation of the direction angle is equivalent to the previous calculation (see Eq. (2.23)). It only depends on a'_1 and b'_1:

$$\varphi' = \frac{1}{2}\text{arctan2}(-b'_1, a'_1). \tag{4.5}$$

In contrast, the retardation and transmittance differ as compared to the previous calculations (Eqs. (2.21) and (2.22)) which consider a retardance induced by a quarter-wave retarder. It is possible to derive the retardation and transmittance by employing all five of the new Fourier coefficients. The equations describing the new correlations are:

$$r' = \left|\sqrt{a_1'^2 + b_1'^2}\cdot\frac{2\sin^2(\Gamma)}{|\sin(2\Gamma)|}\left(a'_0 - \frac{\sqrt{a_2'^2 + b_2'^2}}{|\cos(2\Gamma)|}\left(\cos(2\Gamma)\right)\right)^{-1}\right|, \tag{4.6}$$

$$I'_{0T} = \frac{1}{\sin^2(\Gamma)}\left(a'_0 - \frac{\sqrt{a_2'^2 + b_2'^2}}{|\cos(2\Gamma)|}\left(\cos^2(2\Gamma)\right)\right). \tag{4.7}$$

The dependency of r' and $I_{0T'}$ from the Fourier components are more complex as compared to the perfect quarter-wave retardance. Therefore, it is no longer possible to assign the measured relative amplitude to the retardation and the average intensity across all 18 measurements to the transmittance. For previously measured data which was analyzed using the 3D-PLI standard analysis, it is possible to correct the determined retardation values.

The necessary correction is:

$$f_c(\Gamma,\delta) = \frac{r}{r'} = \frac{\frac{\sqrt{a_1'^2+b_1'^2}}{a_0'}}{\sqrt{a_1'^2+b_1'^2}\cdot\frac{2\sin^2(\Gamma)}{\sin(2\Gamma)}\left(a_0' - \frac{\sqrt{a_2'^2+b_2'^2}}{|\cos(2\Gamma)|}\left(\cos^2(2\Gamma)\right)\right)^{-1}}$$
$$= \frac{\frac{1}{2}\sin(2\Gamma)}{\frac{1}{2}\sin^2\left(\frac{\delta}{2}\right)+\sin^2(\Gamma)\cos^2\left(\frac{\delta}{2}\right)} \tag{4.8}$$

Thus, a correction function $f_c(\Gamma,\delta)$ depending on the fiber inclination angle and the induced phase shift of the retarder is necessary to correct the retardation value determined with the 3D-PLI standard analysis. The amplitudes of the 3D-PLI signal measured with a retardance of $\delta = 2\pi\cdot 142/529$ are expected to be lower than for a light retardance of $\pi/2$ (cp. Fig. 3.11). The correction function implicates the necessity to multiply the measured retardation values with a value between $f_c(\alpha = 0\,^\circ) = 1/0.939$ and $f_c(\alpha = 90\,^\circ) = 1/0.8904$ (see Fig. 4.1 A) when considering a light path difference of $142/529\lambda$. However, when measuring tissue the fiber inclination angle is unknown and it is not possible to use the correction function proposed in Equation (4.8). Thus, instead of employing a correction function, a correction factor c_λ is introduced to compensate the decrease of the normalized amplitude caused by the wavelength discrepancy:

$$\sim c_\lambda \cdot r. \tag{4.9}$$

The compensation with a factor is only possible as the maximal and minimal value obtained with the correction function only differ by $\Delta r = 0.0486$. The maximal measurable retardation value is reduced from $r_{\max} = 1.0$ to 0.939 due to the wavelength discrepancy. If $c_\lambda = 1/0.939$ is chosen as a correction factor, a marginal error of up to $|\Delta r| = 0.025$ for $\alpha = 45\,^\circ$ is introduced (see Fig. 4.1 B).

Theoretically, it is possible to choose any value between $f_c(0\,^\circ) = 1/0.939$ and $f_c(90\,^\circ) = 1/0.8904$ as a correction factor, but, by choosing the maximal value, the overall induced error is minimized and the determination of low inclination angles is as accurate as possible. Especially for low inclination angles, small deviations of the retardation value induce large errors in the inclination angle.

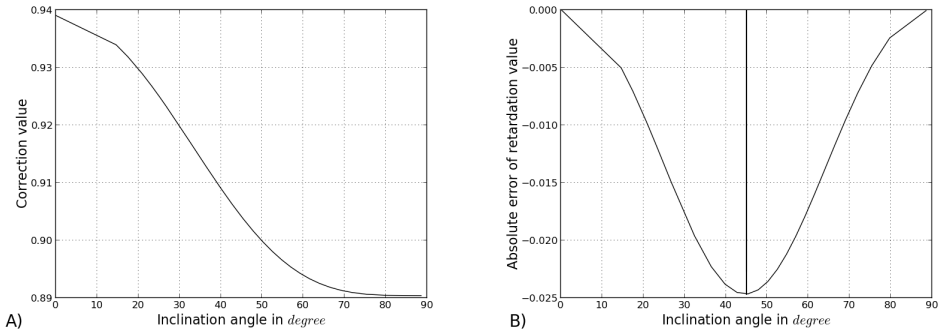

Figure 4.1: Correction factor c_λ. (A) Correction function to compensate the described wavelength discrepancy depending on the fiber inclination angle. (B) Induced error by employing a factor of $c_\lambda = 0.939$ instead of the correction function.

4.1.2 Influence of the Lateral Resolution

The influence of the partial volume effects induced by the inhomogeneity of biological tissue and the discrete sampling of these structures has to be considered. The term "partial volume effect" is commonly used in medical imaging such as in positron emission tomography [69], single-photon emission computed tomography [70], and diffusion tensor imaging [71] to describe the fact that within a single volume element (voxel), a signal composed of several, typically unknown sources is measured (as visualized in Fig. 4.2). In 3D-PLI the different unknown sources are nerve fibers with diverging orientations. Assuming that a single voxel contains only a single fiber, would result in a measured sinusoidal signal which encodes exactly this fiber orientation. For a coarser resolution, where a voxel contains multiple fibers with different orientations, it is not possible to decode this information of multiple fiber orientations from a single sinusoidal signal. The more heterogeneous the fiber orientations are, the higher is the expected partial volume effect. Hence, the lateral partial volume effect in 3D-PLI depends on the inhomogeneity of biological tissue and the employed spatial resolution with which these structures are imaged. For 3D-PLI, the partial volume effects in the x-y-plane (also referred to as lateral partial volume effect) and partial volume effects in the z-plane (also called axial partial volume effect) differ significantly in their theoretical description and have to be considered separately. The lateral partial volume effect is caused by the discrete sampling

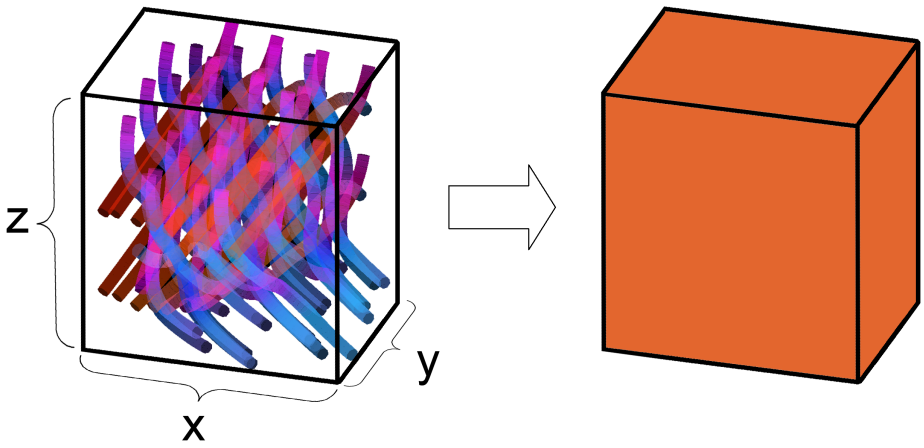

Figure 4.2: Partial volume effect. Only the net effect of multiple fibers crossing within a single voxel is measured.

of the fibers. With an optimal system, each fiber would be measured in a single pixel inducing a sinusoidal signal that encodes the fiber orientation of this fiber. By reducing the resolution, multiple fibers contribute to the signal measured within one pixel. A reduction of the optical resolution can be modeled by blurring the signal and reducing the sampling rate of the detector. The measured sinusoidal curve is the result of the averaging of multiple curves. In contrast, the axial partial volume effect is induced by the spatial stacking of multiple fibers. An ideal sample would be so thin that only one fiber is measured along the z-axis. The fiber retards the light individually depending on its orientation. However, in reality the sections are cut with a thickness between 50 µm and 100 µm. In this case, the light encounters multiple fibers when traveling through the tissue. Each fiber retards its input light depending on its individual orientation. Thus, the tissue measurements should be described by a sequence of multiple retarders, which is not realized, yet.

The following considerations will only concern the lateral partial volume effect. The influence of the axial partial volume effect will be neglected as it is not caused by limitations of the system but rather by a simplification of the theoretical model. To investigate the lateral partial volume effec,t it is important to comprehend the signal theory behind it.

Within an ideal system, each point in object space is represented by a point in image space. Due to the 3D-PLI measuring procedure, each point in the

image space is described by a sinusoidal wave (cp. Fig. 2.5). The sinusoidal waves all have the same frequency, but they differ in terms of amplitudes and phases which depend on the orientation of the imaged nerve fibers. Thus, in reality, where the object space is sampled in discrete steps, multiple sinusoidal waves are averaged in one point in image space. If different sinusoidal signals are averaged, the result is a sinusoidal wave with a different amplitude A and a different phase ϕ.
The superposition of two sinusoidal waves with a phase shift of ϕ_1 and the amplitudes A_1 and A_2 can be described as:

$$\begin{aligned} f_1(t) &= A_1 \sin(\omega t), \\ f_2(t) &= A_2 \sin(\omega t + \phi_1), \\ \Rightarrow f_1(t) + f_2(t) &= A \sin(\omega t + \phi), \end{aligned}$$

with

$$A = \sqrt{A_1^2 + A_2^2 + 2A_1A_2\cos(\phi_1)} \tag{4.10}$$

and

$$\phi = \arctan\left(\frac{A_2\sin(\phi_1)}{A_1 + A_2\cos(\phi_1)}\right) \tag{4.11}$$

(The detailed derivation of this correlation is given in Appendix A.4.)
The following considerations are based on Equations (4.10) and (4.11). This approach is a simplification of the actual measurement, but it is not sufficient to grasp the idea of averaging multiple sinusoidal signals.
The outcome of the superposition depends on the mixture of the orientations of nerve fibers measured simultaneously within a pixel. If the fibers are perfectly aligned (i.e., parallel, see Fig. 4.3 A), the influence of the resolution will be neglectable. In this case, all fibers cause sinusoidal signals with the same amplitude and phase. Thus, the result in image space is the same, independently of the optical resolution. However, as soon as the fibers that are measured in a single image point have different orientations, the amplitude of the output signal will be reduced as compared to the maximal input amplitude.
In case that fibers with different inclination angles (= with different amplitudes), but with the same in-plane direction (= the same phase) are measured, the output amplitude is lower than the maximal input amplitude,

but not less than half of the maximal input amplitude (see Fig. 4.3 B). If fibers with the same inclination angle (= same amplitude), but with varying in-plane-directions (= different phases) are averaged, the amplitude of the output sinus will be smaller than half of the initial amplitudes (see Fig. 4.3 C).
It is also possible that the output amplitude is lower than either one of the input amplitudes, but this only occurs for large discrepancies of the phases. In the extreme case that fibers with the same inclination run perpendicular to each other ($\Delta\varphi = 90\,^\circ$), the output amplitude is zero (see Fig. 4.3 D). Thus, as soon as the signals of multiple fibers are averaged, a signal decrease is expected. Determining the system response to a known fiber distribution enables the compensation of the error inflicted by partial volume effects.
Within brain tissue, a vast variety of mixed fiber orientations can occur. If measured with a relatively low resolution, the averaging will result in minor or major signal decreases. A function considering the heterogeneity of the tissue per pixel and the optical resolution, enables a correction of the partial volume effect in the x-y-plane.
Due to the thorough characterization of the two employed polarimetric systems, the optical resolutions are known. Up to now, no measure was available to evaluate the heterogeneity of the tissue. The wavelength discrepancy as well as the influence of the resolution concerning the lateral partial volume effect are both system intrinsic and influence every measurement equally. Thus, an additional correction function considering the heterogeneity of the tissue for each pixel is necessary:

$$r_c'' = f_{xy} \cdot c_\lambda \cdot \left| \sin\left(\frac{\pi}{2} t_{\mathrm{rel}} \cos^2(\alpha) \right) \right|.$$

However, as a first approach, the minimal signal decrease that occurs for almost parallel fibers induced by different optical resolutions is investigated.

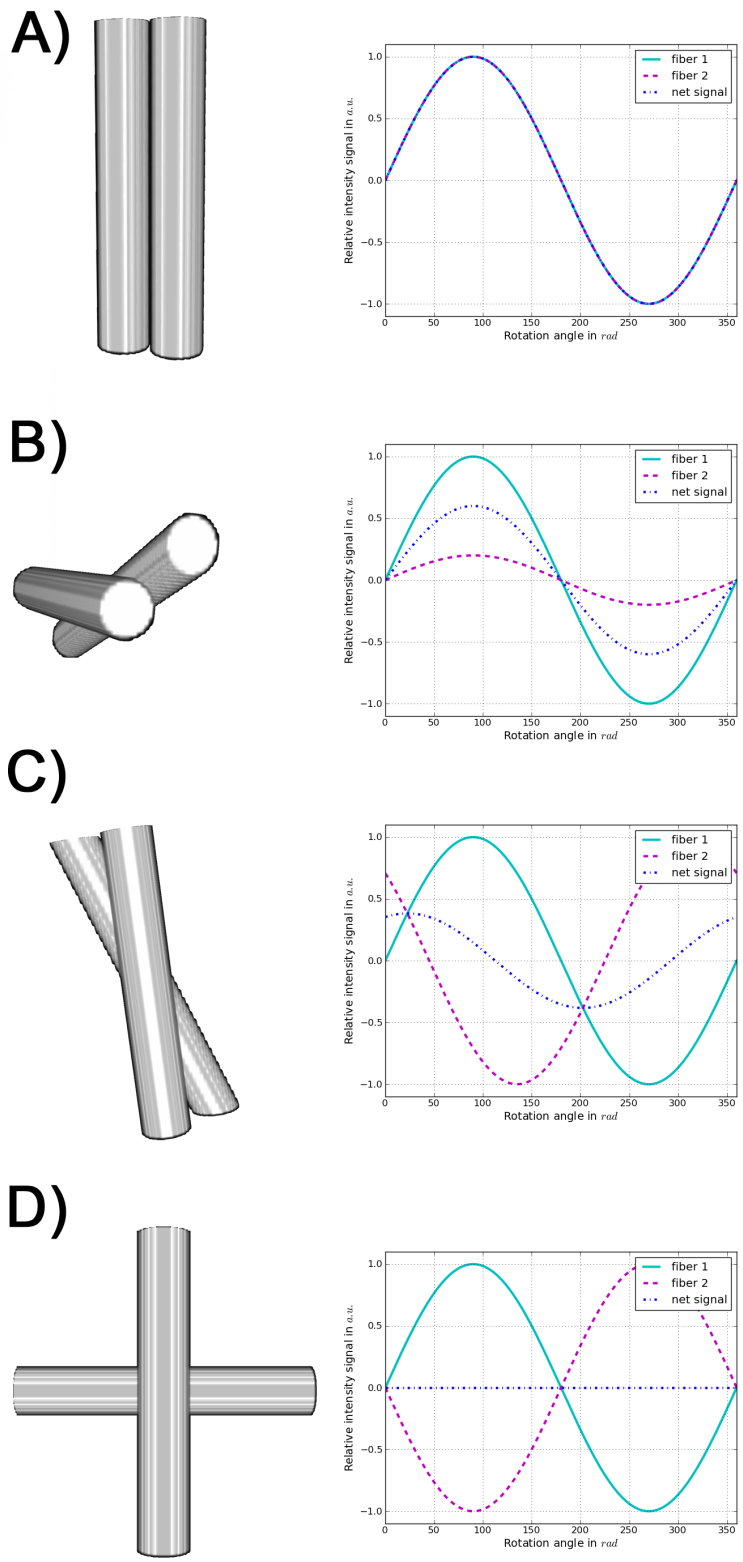

Figure 4.3: Examples of different fiber alignments. A) parallel fibers, B) fibers with different inclination angles, C) fibers with different direction angles, and D) perpendicular fibers.

4.2 Experimental investigation of correction factors

This section will address the issue if the determined correction factor c_λ is sufficient to compensate the influence of the wavelength discrepancy. Furthermore, the influence of the lateral partial volume effect is investigated by artificially reducing the resolution of the data obtained with the PM. Finally, the consistency of the fiber orientations measured with the LAP and with the PM will be tested.

4.2.1 Materials and Methods

Tissue preparation For the evaluation of the influence of the wavelength discrepancy and the optical resolution a human optic tract and the optic nerve were chosen. For convenience, both the optic tract and the optic nerve are going to be referred to as the "*optic tract*". The *optic tract* is a massive bundle of nerve fibers which is commonly used as a reference fiber bundle of uniformly oriented fibers with a homogeneous myelination [72]. So far, it represents the best available phantom to investigate the system's response to birefringent tissue. To obtain the optic tract, a post-mortem adult human brain was retrieved in accordance with legal requirements from the body donor program at the medical department of the Rheinisch-Westfälische Technische Hochschule in Aachen (Germany). The donor had no documented neurological or psychiatric diseases. Directly after its removal, the brain was immersed in a 4% buffered formalin solution for six months. Before freezing, the brain was placed in glycerin which acts as a cryoprotector. After its extraction from the brain, the *optic tract* was divided into four slabs. Using TissueTek, each slab was separately mounted onto a mounting table, in such a way that it was cut under angles of 0 °, 30 °, 60 °, and 90 ° with respect to the main fiber bundle direction (see Fig. 4.4). Since only the fiber inclination angle is relevant for the studies described here, the sections cut under different angles will be referred to as 0 °-, 30 °-, 60 °- and 90 °-sections in the following. Furthermore, the slabs were cut with thicknesses of 20 µm, 30 µm, 50 µm, 70 µm and 100 µm using a cryostat microtome (Polycut CM 3500, Leica, Germany). For each angle and thickness, at least four sections were prepared (the exact number of sections is given in the Appendix A.6). In order to prevent the histological sections from dehydration, they were

covered with Aquatex and a thin glass cover slip.

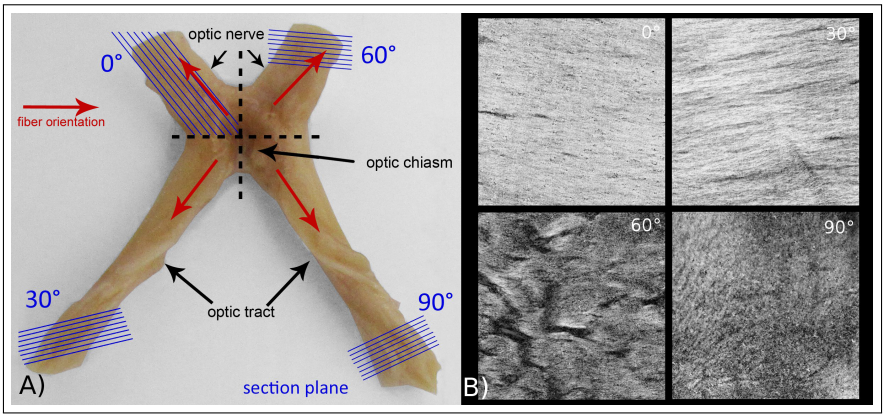

Figure 4.4: Formalin fixed cross-over (optic chiasm) of the optic nerve to the optic tract. (A) Cutting scheme of optic tract and nerve. (B) Microscopic 3D-PLI transmittance images of *optic tract* sections cut under different angles (0°, 30°, 60° 90°).

For further investigations, a coronal section of a post-mortem Vervet monkey brain was prepared. Through the NIH program under grant number *1R01MH092311-01A1* one post-mortem brain of a Vervet monkey was retrieved, in accordance with legal requirements. The same preparation procedure as described for the *optic tract* was used. The brain of the Vervet monkey was cut with a thickness of 70 µm using a freezing microtome (Polycut CM 3500, Leica, Germany).

Downsampling procedure. To investigate the influence of different optical resolutions regarding the measured signal, the images obtained with the PM were artificially downsampled. It is assumed that artificial downsampling describes the process of convoluting the PM images with a Gaussian filter and rescaling the processed image (as shown in Figure 4.5 on the left side). The artificial downsampling approach is based on signal theoretical considerations. As depicted in Figure 4.5 (for the LAP), the imaging process is separated into two steps. First, the sample is imaged with the lens which is approximated by the convolution of the image with a Gaussian filter. After passing the lens, the image is spatially digitized by a CCD chip. In case of the PM, the object is first imaged regularly and is then artificially downsampled. In order to simulate the influence of the lens of the LAP, a Gaussian filter was chosen considering the predetermined optical resolution

limits, which in this case corresponds to a filter radius of:

$$\sigma_{\mathrm{LAP}} = \frac{1}{2} \cdot \frac{d_{xy}(\mathrm{LAP})}{d_{xy}(\mathrm{PM})} = \frac{1}{2} \cdot \frac{159}{3.9} \approx 20.$$

For this purpose, the standard Gaussian filter that is implemented in *Fiji* [64] was used. The Gaussian filter was applied to the 18 calibrated images. Afterwards, the blurred images were resampled with a factor of:

$$f_{sc} = \frac{1.33 \frac{\mu m}{\mathrm{px}}}{64 \frac{\mu m}{\mathrm{px}}} \approx \frac{1}{48},$$

to model the spatial sampling of the detector of the LAP. It is essential that the downsampling is executed either using the calibrated images obtained for each rotation angle or using the maps a_0, a_1 and b_1 of the Fourier coefficients which were calculated using Equations (2.18) to (2.20). This approach reproduces the averaging process of the sinusoidal signals during the imaging process. It is important to apply the downsampling procedure to the measured images or to apply it to the maps containing the information about the Fourier coefficients instead of using the retardation and direction maps to prevent false interpretations. A reasonable direct downsampling of the direction angle map is not possible due to its parameter space, where the in-plane fiber directions are described within a range of $0\,^\circ < \varphi < 180\,^\circ$. Hence, the direction values $\varphi = 0\,^\circ$ and $\varphi = 180\,^\circ$ describe the same in-plane orientation of nerve fibers and averaging these fiber directions yields incorrect results.

A manual segmentation of the images was performed using the high resolution, stitched PM images. The obtained masks were rescaled using a nearest neighbor interpolation. To understand how slight changes of the imaging resolution affect the measured retardation signal, the PM measurements of the *optic tract* were downsampled by applying different configurations:

- PM_2: $\sigma_2 = 2\,\mathrm{px}$, $f_{\mathrm{sc}} = \frac{1}{2}$,
- PM_4: $\sigma_4 = 4\,\mathrm{px}$, $f_{\mathrm{sc}} = \frac{1}{4}$,
- PM_8: $\sigma_8 = 8\,\mathrm{px}$, $f_{\mathrm{sc}} = \frac{1}{8}$,
- PM_{16}: $\sigma_{16} = 16\,\mathrm{px}$, $f_{\mathrm{sc}} = \frac{1}{16}$,
- $\mathrm{PM}_{\mathrm{LAP}}$: $\sigma_{\mathrm{LAP}} = 20\,\mathrm{px}$, $f_{\mathrm{sc}} = \frac{1.33}{64} = \frac{1}{48}$.

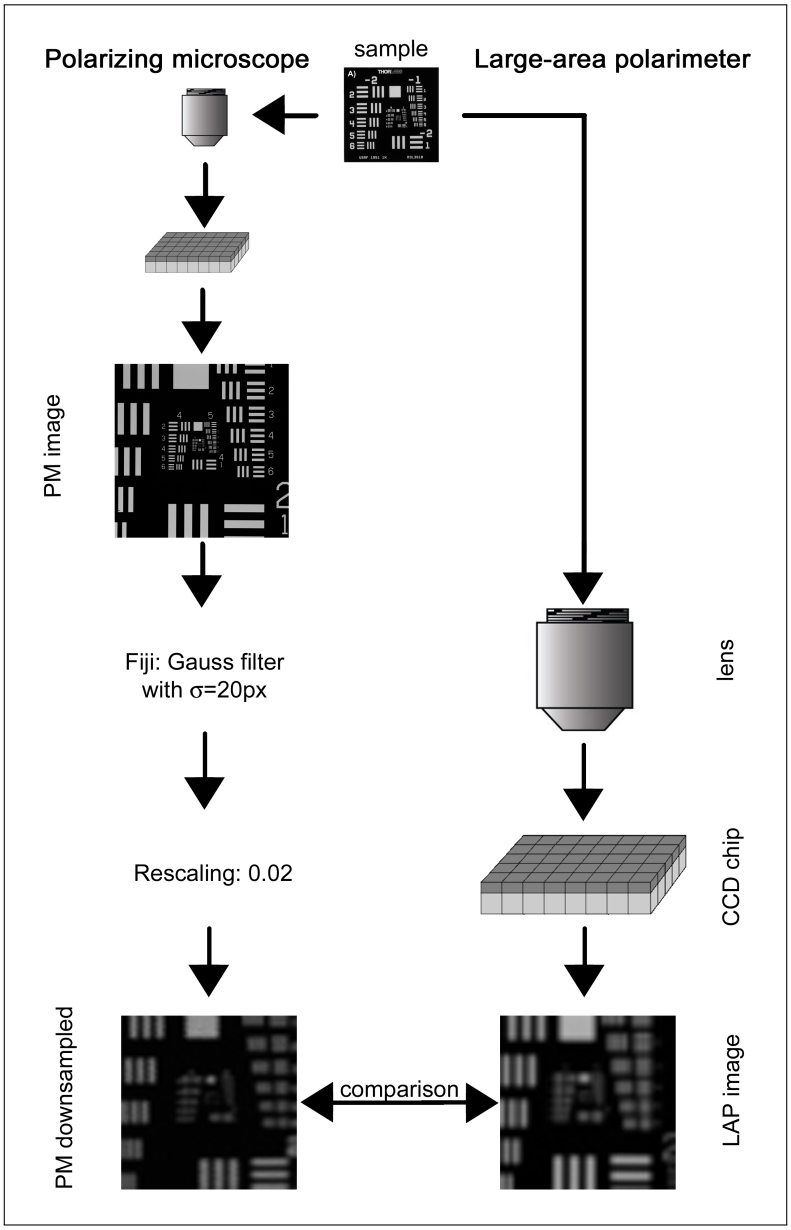

Figure 4.5: Scheme of the downsampling procedure. The images obtained from the PM were filtered with a Gaussian filter and rescaled to model the influence of the lens and the CCD chip of the LAP.

Influence of the wavelength discrepancy. To compare the responses of both polarimetric systems to homogeneous brain tissue, carefully selected sections of the *optic tract* were measured using the standard 3D-PLI procedure (see Sec. 2.3). The sections were chosen with respect to their homogeneity. They were segmented, i.e., the background was removed from the image to ensure that only the homogeneous parts were considered for further measurements and to ensure comparable results from the PM and the LAP. The images obtained with the PM were not stitched and each tile was segmented separately.
To increase statistics, the sections were grouped into so called "datasets". Each dataset consists of sections with the same thickness and the same cutting angle. The sections of each dataset were analyzed using an accumulated histogram. The resulting frequency distribution of the normalized signal amplitudes was fitted with a modified sigmoidal function to determine the retardation value with the highest number of entries, thus yielding a representative retardation value. Finally, the extracted values for the PM and the LAP were compared to each other for each dataset.The measurements obtained with the LAP were evaluated with three different approaches. First, the retardation values were calculated according to the 3D-PLI standard analysis (see Eq. 2.22). Secondly, the determined retardation values obtained with the standard approach were multiplied with the correction factor c_λ. And thirdly, the retardation values were calculated according to new approach using Equation 4.8.
For a quantitative analysis of these three approaches a section of the *optic tract* cut under an angle of $30\,^\circ$ with respect to the main fiber orientation was investigated. The section was imaged with both systems. To ensure the best possible comparability the data measured with the PM was stitched. Furthermore, it was ensured by manual segmentation that exactly the same areas were analyzed.

Influence of the resolution. According to Chapter 3, the PM and LAP differ in terms of their optical resolution limit as well as their spatial sampling rates. For the analysis of the combined influence of the inhomogeneity of brain tissue and the optical resolution, data obtained with the PM was artificially downsampled using the downsampling parameters $\sigma_{\mathrm{LAP}} = 20\,\mathrm{px}$ and $f_{\mathrm{sc}} = 1/48$ to match the resolution of the LAP.

To compare the results obtained with the LAP with the artificially downsampled PM results, the retardation signals of the LAP were calculated according to new approach which considers the wavelength discrepancy. The downsampling procedure was applied to six representative sections. The sections had a thickness of $t = 70\,\mu\text{m}$ and inclination angles of $\alpha = 0\,^\circ$ and $\alpha = 90\,^\circ$. They were imaged and processed according to the standard 3D-PLI procedure as described in Section 2.3. The images obtained with the PM were stitched to enable an identical segmentation of the sections imaged with both polarimeters.

The necessity to introduce a correction factor c_{xy} to compensate a minimal partial volume effect was investigated based on the measurements of the *optic tract* sections which were cut under an angle of $0\,^\circ$ with respect to the main fiber orientation and a section thickness of 70µm. By comparing the results measured with the LAP and the PM, it is possible to evaluate a minimal partial volume effect that is expected to affect all measurements with the LAP. The *optic tract* was chosen for this investigation as it is mainly composed of parallel fibers. Thus, if the measurements of the LAP show a reduced retardation signal in comparison to the PM data, all LAP measurements have to be correct for a minimal partial volume effect. In this case, the correction factor to correct for a minimal partial volume effect c_{xy} will be determined according to the following equation:

$$c_{\text{xy}} = \frac{r'_{\text{LAP}}(0\,^\circ, 70\,\mu\text{m})}{r_{\text{PM}}(0\,^\circ, 70\,\mu\text{m})} \tag{4.12}$$

For the majority of white matter, higher partial volume effects than the ones measured for the *optic tract* are expected as most fiber tracts contain fibers with a more heterogeneous orientation. However, with this approach it is only possible to investigate the minimally introduced partial volume effect. For a more general investigation of the partial volume effect, the section of the Vervet monkey brain was investigated. As explained previously, the lateral partial volume effect in 3D-PLI depends on the inhomogeneity of biological tissue and the employed spatial resolution with which these structures are imaged. It is highly desirable to quantify the influence of the lateral partial volume effect, in order to improve the interpretation of 3D-PLI measurements. A comparison of the averaged retardation value with the value of averaged sinusoidal curves seems promising. For example, for parallel

fibers, the averaging of the amplitudes of each pixel will give the same results, if the sinusoidal curves are averaged. As soon as the orientation of the fibers are heterogeneous, the averaged amplitude value is higher than the amplitude value of the averaged sinusoidal signals. Thus, the difference of the averaged and correctly downsampled amplitude values should be a measure of the heterogeneity of the imaged tissue structure.
For such a quantitative evaluation of the lateral partial volume effect, the registered section of the Vervet monkey brain was used. First, the LAP image was upscaled using a nearest neighbor interpolation to match the pixel/image-matrix of the PM image. Then, for each original LAP-pixel a region of interest (consisting of 48×48 pixels in the upscaled LAP image) was defined, creating a list of 498,612 ROIs to be evaluated. The mean retardation value and correlated standard deviation of each ROI was measured individually for the LAP image and for the PM image. The evaluated retardation values measured with the LAP were calculated according to the new analysis.

Comparison of retrieved fiber orientations. In order to evaluate the consistency of the fiber orientations measured with the PM opposed to the corrected measurements executed with the LAP, a whole Vervet brain section was exemplarily measured employing both systems. The measurements were calibrated and processed according to the 3D-PLI standard analysis ($\sigma_{\mathrm{LAP}} = 20\,\mathrm{px}$, $f_{\mathrm{sc}} = 1/48$). The PM data was artificially downsampled to match the image resolution and dimensions of the LAP. In this case, the downsampling procedure was directly applied to the parameter maps of the Fourier coefficients (a_0, a_1, and b_1 (cf. Eqs. (2.18) to (2.20))). This approach reproduces the averaging process of the sinusoidal signals during the imaging process. Based on the downsampled Fourier coefficient maps, the downsampled direction and retardation maps were calculated according to Equations (2.21) to (2.23).
Furthermore, the LAP image was registered to the PM image. As the tissue is in a liquid solution, its shape can change slightly between the two measurements causing the necessity of a non-linear registration. The images were subdivided into four regions of interest to minimize the influence of local rectifications. The images were first registered using a rigid and affine transformation and finally a b-spline transformation [73] was used.

The in-plane direction angles determined with the PM were corrected with $\Delta\varphi = -20.63\,°$. The retrieved fiber direction angle and retardation maps measured with the LAP and the downsampled PM were evaluated pixelwise using differential maps and scatterplots. The differential maps represent the difference between the value measured with the LAP and the value measured with the PM. The analysis is based on the evaluation of the white matter (see reddish highlighted area in Fig. 4.6). In total, 206,788 single pixels were evaluated in the white matter.
The scatterplots were fitted based on a simple linear regression using *Python*.

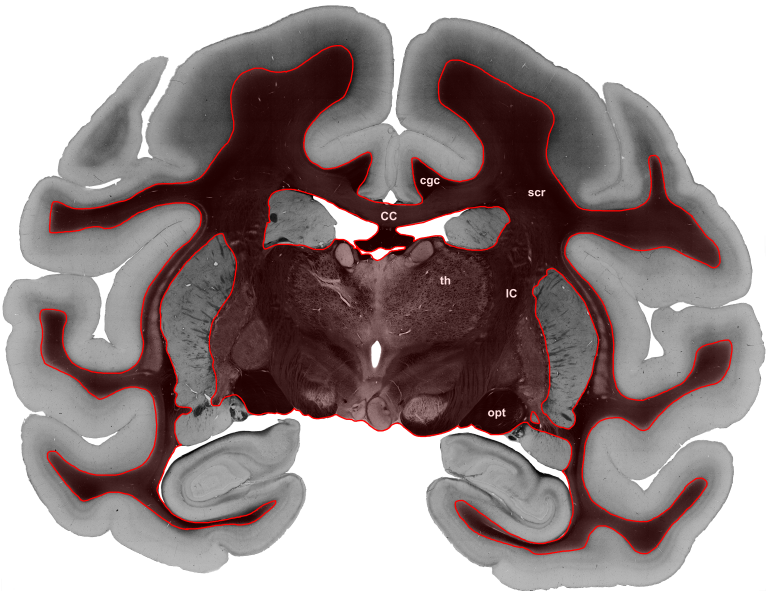

Figure 4.6: Transmittance image of the evaluated coronal, Vervet monkey brain section. The red shaded area indicates the evaluated region of interest.
(CC: corpus callosum, cgc: cingulate gyrus part, th: thalamus, opt: optical tract, scr: superior corona radiata, IC: internal capsule)

4.2.2 Results

Using the sections of the *optic tract* and taking theoretical considerations about the influence of the wavelength discrepancy into account, it was possible to separate the influence the wavelength discrepancy, the lateral resolution, and the tissue heterogeneity.

Influence of the wavelength discrepancy. Using the 3D-PLI standard analysis, overall smaller retardation values were measured for the sections

of the *optic tract* with the LAP than with the PM. In Figure 4.7, the results of the measurements of the *optic tract* sections using the PM are plotted against the results obtained with the LAP. The amplitudes of the signals were determined by using the 3D-PLI standard analysis (green crosses), the proposed correction with the factor c_λ (red crosses) and the new approach employing the new Fourier coefficients (blue crosses). When using the standard 3D-PLI analysis, the measured retardation values of the same datasets are higher for the PM (ordinata) than for the LAP (abscissa), indicated by the fact that all data points are below the bisecting line (green crosses).

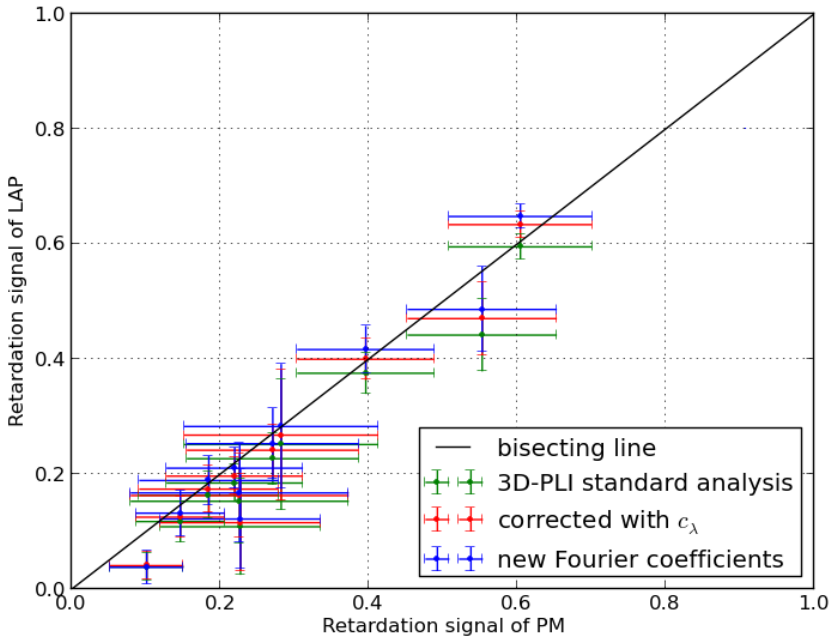

Figure 4.7: Measurements of the *optic tract*. Comparison of the measured retardation values for the PM and the LAP. The retardation values of the LAP were calculated employing the 3D-PLI standard approach (green) and using the new approach considering the wavelength discrepancy (blue). Furthermore, the retardation values obtained with the 3D-PLI standard analysis were corrected by multiplying them with the correction factor c_λ (red).

Applying the correction factor $c_\lambda = 0.939$ (as described in Sec. 4.1.1) to the LAP data, higher retardation values are obtained (red points). The application of the correction factor affects high retardation values more than low retardation values. The measured representative retardation value for

a sample with a section thickness containing flat fibers (e.g., $t = 70\,\mu\text{m}$, $\alpha = 0\,^\circ$) was increased from 0.721 to 0.767 due to application of the correction factor c_λ. In contrast, low retardation values were hardly affected by the correction factor. The evaluation of the measured signals considering a retardance of $\delta = 2\pi \cdot 142/529$ results in even higher retardation values than the application of the factor c_λ (cp. Fig. 4.7, red versus green crosses). Compared to the application of c_λ, the new analysis had the largest impact on medium retardation values ($0.3 < r < 0.6$). Within this range, the retardation values obtained with the new Fourier coefficients were up to $\Delta r = 0.035$ higher than the ones calculated with c_λ. The new analysis had no impact on the extraction of very low retardation values. The increase of the measured retardation values for values larger than $r > 0.6$ was small compared to the induced change by the correction factor.
However, it was not possible to cover the full dynamic range of the theoretically possible retardation values between $r_{\text{min}} = 0$ and $r_{\text{max}} = 1$ neither with the PM nor with the LAP. The available dynamic range of the systems are $\text{DR}_{\text{PM}} = 0.841$ and $\text{DR}_{\text{LAP}} = 0.693$ (new: $\text{DR}_{\text{LAP}} = 0.748$) for the PM and LAP, respectively.
The investigation of the *optic tract* section cut under an angle of $30\,^\circ$ with respect to the main fiber direction (displayed in Figure 4.8), confirmed the results of Figure 4.7. The measurements executed with the PM and interpreted with the 3D-PLI standard analysis (blue line) yielded a peak inclination angle of $48.0\,^\circ$. When employing the standard 3D-PLI analysis (red line) for the evaluation of the LAP data, slightly higher inclination angles were measured than with the PM. Due to the application of the correction factor, the spatial distribution is clearly shifted to smaller inclination angles (yellow line). The analysis considering the wavelength discrepancy (cp Eq. (4.6) results in even smaller inclination angles than the other methods. Based on these results, the highest accordance of the inclination angle is achieved with the correction factor c_λ. In this case, the same inclination angle is measured with the LAP and with the PM.

Influence of resolution. It is expected that due to the lower resolution of the LAP compared to the PM, the measured data is more affected by partial volume effects.
First, the influence of different resolutions was investigated using the sec-

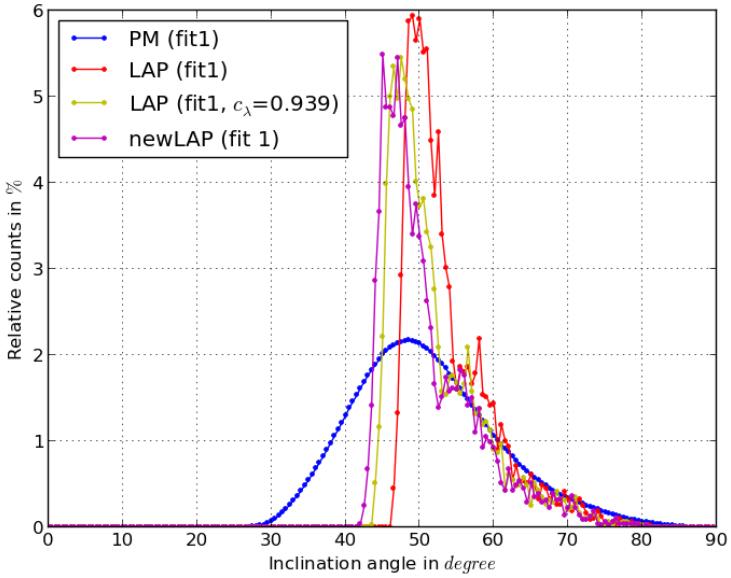

Figure 4.8: Retardation-inclination-correlation. Comparison of inclination angles for measurements obtained with the PM (blue) and the LAP (red) of an *optic tract* section with $\alpha = 30\,^\circ$ and $t = 70\,\mu\text{m}$, calculated using (A) $t_{\text{rel}} = 0.96$ and (B) $t_{\text{rel}} = 1$ and $c_\lambda \cdot c_{xy} = 0.8$.

tions of the *optic tract*, which were cut under $0\,^\circ$ with respect to the main fiber direction. The values in Figure 4.9 were normalized with the total number of counts in order to make them comparable to one another. The data obtained with the PM showed a peak retardation at $r_{\mathrm{PM,peak}}(0\,^\circ) = 0.907$. The measured probability distribution for the PM (cp. Fig. 4.9 A, blue line) is unsymmetrical with a slow increase in counts towards the peak value and a sudden drop towards higher retardation values. The highest value measured with the PM is $r_{\mathrm{PM,max}}(0\,^\circ) = 0.962$.
With an increase of the averaging of the data, the peak retardation shifts slightly towards lower retardation values and the peak broadens. With the degree of downsampling, the amount of extremely high and low retardation values is decreased, while the amount of medium retardation values is increased. The usage of a moderate downsampling algorithm (see Fig. 4.9 B, $\mathrm{PM}_2 \rightarrow$ magenta curve) has the largest influence on the data, changing the mean value from $r_{\mathrm{PM}}(0\,^\circ) = 0.733$ to $r_{\mathrm{PM}*_2}(0\,^\circ) = 0.727$. Further downsampling has a smaller impact as shown in Figure 4.9 B. For example, increasing the diameter of the Gaussian filter and increasing the pixel size by a factor of four ($\sigma_2 \rightarrow \sigma_8$) changes the mode value to $r_{\mathrm{PM}^*8}(0\,^\circ) = 0.726$. Applying the downsampling algorithms with σ_8 (light blue curve) and σ_{16} (purple curve) yields nearly identical probability distributions.
By increasing the applied downscaling factor, the interpretation of the measurements became increasingly difficult as for low numbers of pixels, the number of counts per retardation tended to vary strongly. For example, for the analysis of the LAP and consequently for the downsampled data of the PM (with $\mathrm{PM}_{\mathrm{LAP}}$) for sections cut under $0\,^\circ$, only about 15,000 pixels were available. Thus, the resulting histograms in Figure 4.9 A for the downsampled PM with $\mathrm{PM}_{\mathrm{LAP}}$(red curve) and the LAP (green curve) appear noisy. The previously observed trend that the peak retardance shifts towards lower values after the application of a downsampling procedure is also visible for the downsampling with a Gaussian filter using $\sigma_{\mathrm{LAP}} = 20$ and a scaling of f_{sc}=1/48. The highest measured value was $r_{\mathrm{PM}^*,\mathrm{max}}(0\,^\circ) = 0.916$ instead of $r_{\mathrm{PM,max}}(0\,^\circ) = 0.960$ for the original PM measurement. The same tendency was observed for the mode values, which were $r_{\mathrm{PM}}(0\,^\circ) = 0.882$ and $r_{\mathrm{LAP}}(0\,^\circ) = 0.858$ for the measurements with the PM and LAP, respectively. The downsampled PM data had a broader peak of $\Delta r_{\mathrm{PM}^*}(0\,^\circ) = 0.67 - 0.87$ that made it impossible to determine the peak value (see Fig. 4.9 A, red

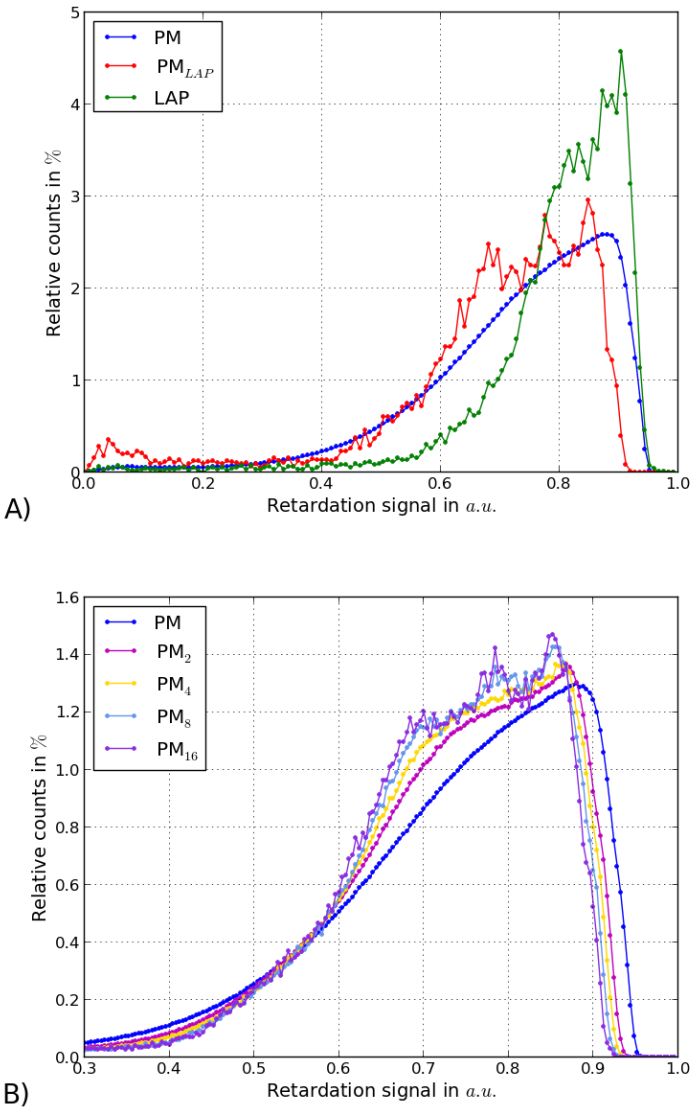

Figure 4.9: Downsampling of *optic tract* sections with $\alpha = 0\,^\circ$ and $t = 70\,\mu\text{m}$. (A) Cumulative histogram of the retardation values measured with the PM (blue curve) and with the LAP (green curve) in comparison to the downsampled PM data (red curve). The PM data was downsampled with $\sigma_{\text{LAP}} = 20$ and $f_{\text{sc}} = 48$. (B) Cumulative histogram of measurements with PM (blue curve) and artificially downsampled PM data.

curve). The probability distribution of the downsampled PM data and of the LAP are similar. Even though the LAP curve appears to be compressed in the x-direction in comparison to the downsampled PM data, the slopes of both curves are alike.

The investigation of the sections cut under 90 ° with respect to the main fiber direction shows the same trend as the 0 °-sections. A slight shift of the peak towards lower retardation values caused by a moderate downsampling (cp. Fig. 4.10, $PM_2 \rightarrow PM$) was measured. The peak retardation value is shifted from $r_{\mathrm{PM}}(90\,^\circ) = 0.232$ to $r_{PM*_2}(90\,^\circ) = 0.0164$. The measured retardation distribution for PM_2 is similar to the distribution obtained for PM_{LAP} (cp. Fig. 4.10). The frequency distribution for these configurations only differ in their smoothness.

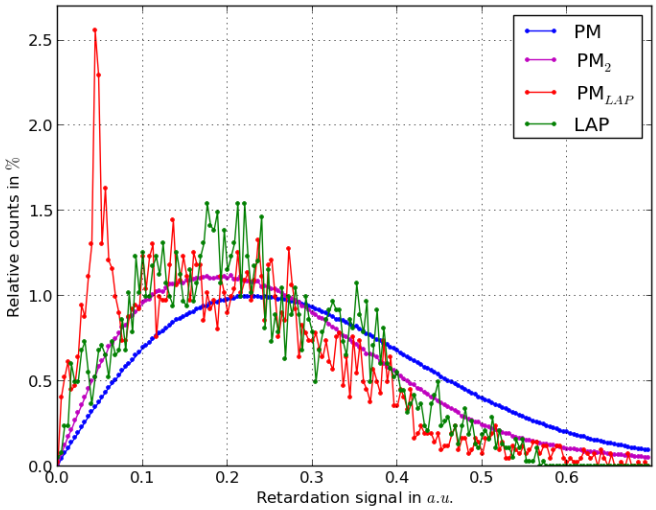

Figure 4.10: Downsampling of *optic tract* sections with $\alpha = 90\,^\circ$ and $t = 70\,\mu\mathrm{m}$. Cumulative histograms of microscopic measurements (blue curve), artificially downsampled microscopic data with σ_2 and $f_{\mathrm{sc}} = 2$ (purple curve), downsampled PM data with σ_{LAP} and $f_{\mathrm{sc}} = 48$ (red curve) and LAP measurement (green curve).

The histograms of the artificially downsampled PM data ($\sigma_{\mathrm{LAP}} = 20, f_{\mathrm{sc}} = 1/48$) and the LAP data are very similar (Fig. 4.10, red and green curve).

In Figure 4.9 A, almost the same retardation values were measured with the LAP as with the PM. With the PM, a retardation value of $r(0\,^\circ, 70\,\mu\mathrm{m})$=0.988 was measured, while a value of $r'_{\mathrm{LAP}}(0\,^\circ, 70\,\mu\mathrm{m})$=0.981 was measured with the LAP. The difference in retardation values is marginal and can be ne-

glected. Thus, the introduction of a correction factor to compensate for partial volume effects of almost parallel fibers is not necessary.
The comparison of the retardation values measured with the LAP and the mean retardation value of the corresponding 48×48 PM pixels revealed that in most cases the averaged PM value is higher than the LAP value (clustering of scatter dots above the bisecting line (purple line) in Fig. 4.11). Especially, for low retardation values for a high number of pixels (77 %), the mean value of the PM pixels is (significantly) higher than the value of the LAP. With an increasing retardation value, the number of pixels with $\hat{r}_{PM}(48\,\text{px} \times 48\,\text{px}) \geq r_{\text{LAP}}(1\,\text{px} \times 1\,\text{px})$ decreases constantly down to 18.3 %. Considering the noise of the retardation of $\sigma(r) = 0.008$ about 17 % of all pixels in the white matter show the same value for the averaged PM measurement and the LAP measurement.

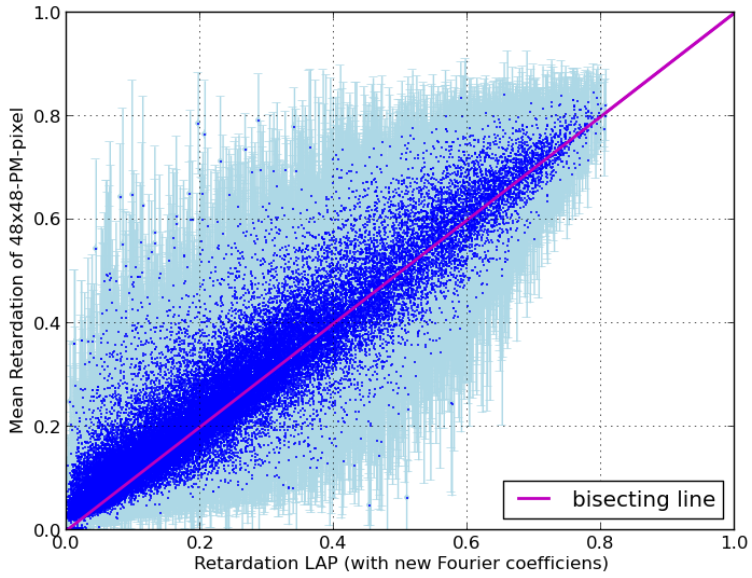

Figure 4.11: Influence of lateral partial volume effects. The averaged retardation values $\hat{r}_{PM}$ of 48×48 PM pixels are plotted against the retardation value determined with the LAP r'. The standard deviation of the averaged retardation values is indicated by the light blue error bars.

Comparison of the retrieved fiber orientations. The influence of the new approach was investigated further by analyzing the determined fiber

orientation using both polarimeters and a Vervet brain section. The fiber direction and inclination angles measured with the PM and the LAP were compared employing differential maps and scatterplots (cp. Fig. 4.12). The scatterplot in Fig. 4.12 B visualizes for each pixel individually the correlation between the value of the in-plane fiber direction measured with the LAP (x-axis) and the PM (y-axis). For the values along the bisecting line (magenta line), exactly the same value was measured with the PM and the LAP. The polynomial fit of the first order through the scatterplot (dotted cyan line) is almost identical to the bisecting line. For most pixels, the in-plane fiber directions measured with the PM and the LAP were consistent. Over 40 % of all pixels in the white matter show a deviation of less than 1 ° from the linear fit. Higher deviations occured only in areas containing heterogeneous fiber orientations such as the thalamus and optical tract (cf. Fig. 4.12 A). The highest deviations (up to 180 °) appeared in areas where the fibers were parallel to the x-axis and the measured angle switches between 0 ° and 180 ° (e.g. right side of the corpus callosum).

The calculation of the inclination angle (according to Eq. (2.15)) confirmed that the observed wavelength discrepancy has an influence on the reconstruction of the fiber orientation (Fig. 4.13 B). Without the correction for the wavelength discrepancy, the inclination angles derived from the measurement with the LAP are higher than with the PM (correlation is indicated by the dotted blue line). The bisecting line indicates the pixels for which the same inclination was measured with both systems. The displayed scatterplot and differential map were obtained by employing the standard 3D-PLI analysis for the PM data and the new mathematical description for the LAP data. For the LAP data a retardance of $\delta = 2\pi \cdot 137/529$ was assumed. The fit through the data points is shown as a cyan dotted line. The inclination angles of the LAP determined with this retardance are similar to the ones measured with the PM. In contrast, the inclination angles evaluated according to the standard analysis (dark blue line) tend to be lower than the inclination angles calculated from the downsampled PM data. With decreasing inclination angle, the absolute difference between the values measured with the LAP and the PM increased as indicated by the higher slope of the fit function in Fig. 4.13 B. When using the correct mathematical approach and assuming a retardance of $\delta = 2\pi \cdot 142/529$ to interpret the LAP measurements, the determined inclination angles with the LAP tend to be lower

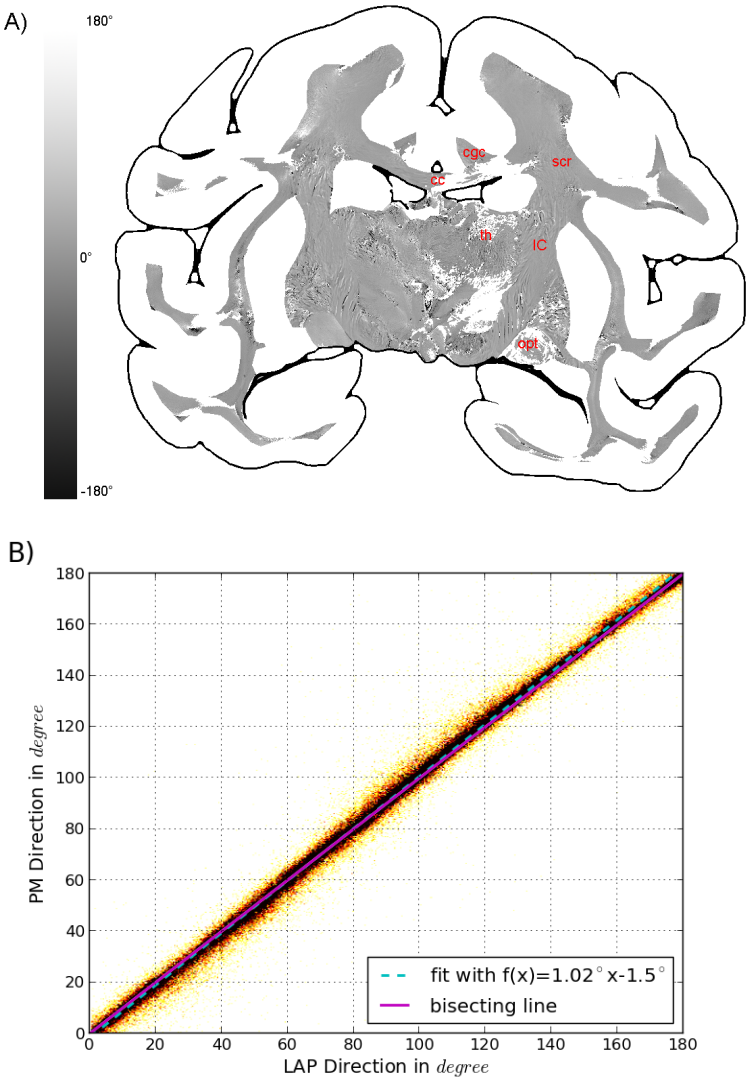

Figure 4.12: Consistency of the measured in-plane direction. (A) displays a differential map of the fiber direction. It highlights in which areas the largest differences of the measured fiber directions occur. (B) shows a scatterplot displaying a direct comparison of the measured fiber direction angles. (cc: corpus callosum, cgc: cingulum, scr: superior coronar radiata, IC: inferior, colliculus, th: thalamus, opt: optical tract)

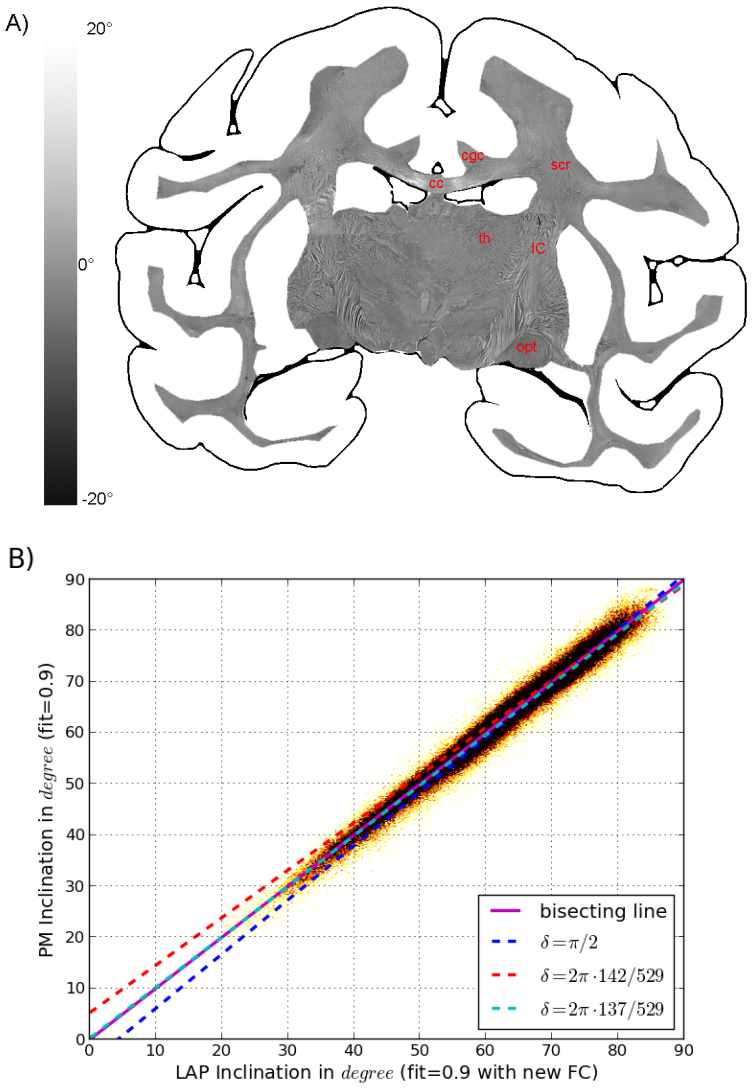

Figure 4.13: Consistency of the measured and corrected inclination angle with the LAP and the measured inclination angle of the PM. (A) shows a differential map and highlights in which areas the largest differences occur. (B) displays a direct comparison of the different approach to calculate the inclination angles. The LAP measurements were interpreted employing the standard analysis (dark blue line), the correct mathematical description assuming a retardance of $\delta = 2\pi \cdot 142/529$ for the retarder (red line), and the correct mathematical description assuming a retardance of $\delta = 2\pi \cdot 137/529$ for the retarder (cyan line).(cc: corpus callosum, cgc: cingulum, scr: superior coronar radiata, IC: inferior, colliculus, th: thalamus, opt: optical tract)

than the ones with the PM (red dotted line). Only when assuming a retardance of $\delta = 2\pi \cdot 137/529$ the same inclination angles were measured with both systems.
The measured differences, displayed in Fig. 4.13 A, are small. Most inclination angles determined with the LAP only differ up to $2\,^{\circ}$ from the downsampled PM value. High differences were only visible in areas with a heterogeneous fiber populations such as the thalamus, internal capsule, and superior corona radiata.

4.3 Discussion

Based on the measurements of the PECF, it was hypothesized that the wavelength discrepancy influences the measurements of the retardation. The measurements of the *optic tract* and theoretical considerations using the Jones matrix formalism, confirmed this. Both approaches, the one employing the correction factor c_λ and the exact mathematical description considering the wavelength discrepancy proved to be feasible to correct the wavelength discrepancy. The difference between the retardation values obtained with the exact mathematical solution and the values determined with the correction factor c_λ is small. Thus, with the correction factor $c_\lambda = 0.939$ it is possible to correct old measurements for which it is no longer possible to determine the correct five Fourier coefficients. The measurements confirmed that the error induced by the correction factor is maximal for medium inclination angles around $\alpha = 45\,^\circ$.

The errors induced when determining the peak retardation values of the *optic tract* datasets, which were measured with the LAP and with the PM, were caused by the heterogeneity of the tissue. Despite the assumption that the *optic tract* contains only parallel fibers with the same myelination, it is still biological tissue that is naturally imperfect in terms of homogeneity, i.e., the fibers are not perfectly aligned, which causes a deviation of the measured retardation values from the peak value. Even though the fibers in the *optic tract* are not perfectly parallel, they can be considered as almost parallel as shown by the downsampling approach. The induced partial volume effect was minimal when downsampling the measurements of the *optic tract*. If the fiber alignment would have been strongly heterogeneous, stronger partial volume effects would have been measured. Thus, the assumption that the *optic tract* is mainly composed of parallel fibers is valid and it was the optimal model to investigate the minimal partial volume effect.

Furthermore, the considerations of the influence of the averaging of sinusoidal signals in Section 4.1.2 proved to be appropriate. It was proposed that the averaging of sinusoidal signals with a similar phase and similar amplitude results in an averaging of the amplitudes, such as was observed when downsampling the $0\,^\circ$-sections. Consequently, for the $90\,^\circ$-sections, where the phases of neighboring pixels become arbitrary, a shift towards lower retardation values was measured. The heterogeneity of the tissue is

the reason that for 90 °-fibers higher values were measured than proposed by Equation (2.15). Furthermore, it was difficult to control the exact cutting angle in reference to the fiber direction as the *optic tract* was slightly twisted (cp. Fig. 4.4 A). Thus, it is very likely that the actual cutting angle differed slightly from the intended 90 °, resulting in higher retardation values. Furthermore, it is possible that in this case the measured light retardance is not induced by myelin, but by birefringent neurofilaments. The neurofliaments only induce a small retardance, which can be neglected for in-plane fibers, but could have an influence when measuring 90 °-fibers. This influence of the birefringence of neurofilaments regarding 3D-PLI measurements should be further investigated. The outlier for small values from the downsampled 90 °-sections, is caused by slight deviations of the segmentation. As the background has a retardation close to zero, averaging the pixels at the border of the section with the background pixels, resulted in a significant decrease of the retardation signal. Apart from this outlier the influence of the lateral partial volume effect in the LAP was well modeled with the downsampling approach.

In contrast, for 0 °-sections it was only partially possible to model the influence of the resolution. Even though for 0 °-sections the proposed shift of the peak value towards lower values was observed, the distribution of the downsampled PM data appeared broadened in comparison to the LAP data. This deviation is attributed to the fact, that the employed downsampling algorithm represents a simplified approach to model the imaging procedure. For the employed downsampling algorithm, the respective pixel size and lateral resolution limit are considered. Replacing the Gaussian filter with the actual system responses would improve the accuracy of the downsampling approach. Describing the influence of the lens as a convolution of the object with a Gaussian distribution is a simplification that disregards image aberrations and that different spatial frequencies are transmitted differently. Furthermore, the differing quality of the polarization filters (cf. Chapter 3), also affects the image quality. This influence was not considered in the current downsampling algorithm. However, the purpose of the designed downsampling procedure was to get an approximation of the influence of the image resolution on the lateral partial volume effect.

By considering the retardation values obtained with the LAP in comparison to the values retrieved when averaging the PM data, it was further shown

that the downsampling procedure is indeed the correct approach to model the influence of lateral partial volume effects. Averaging the 48×48 pixels of the PM retardation map yielded in most cases higher values than were determined with the LAP. This is due to the fact that sinusoidal signals are mixed. The large error bars are due to the inhomogeneity of the tissue. The fact that to most averaged retardation values a large standard deviation is assigned indicates that most LAP pixels are measured with a large lateral partial volume effect. As the signals have differing phase shifts, the LAP value differs from the average values of the amplitudes as previously proposed. This measurement proves that 3D-PLI measurements are indeed inflicted by lateral partial volume effects. However, the downsampling of the $0\,^{\circ}$-fibers showed that not all measurements with the LAP are affected by lateral partial volume effects. For fiber bundles that contain almost parallel fibers such as the optic tract the measurements seem not to be affected by lateral partial volume effects. A minor difference was observed, but it was not significant as it was within the range of the uncertainty of the measured retardation signal. Thus, it is not possible to determine a correction factor for minimal, lateral partial volume effects based on these measurements . However, the introduction of a general correction function to compensate for lateral partial volume effects is still necessary. To determine the main fiber orientation of an investigated pixel is especially important when mapping different brain regions. So far, the mapping of brain regions is by default executed on cytoarchitectonic datasets. By distinguishing the occurrence of certain cell types and their probability different brain regions can be identified.

The comparison of the fiber orientations retrieved with both systems shows that it is essential to consider both effects, the actual retardance of the implemented retarder as well as the lateral partial volume effects to realize a multiscale approach. The scattering of the data points is caused by inhomogeneities of the tissue. Especially, areas with crossing fiber bundles induced large deviations.

Furthermore, the actual retardance of the retarder in the LAP seems to differ from the assumed $\delta = 2\pi \cdot 142/529$. Based on Figure 3.11, a linear correlation between the relative wavelength and the retardance was assumed as no specifications of the implemented retarder were available. However, the retardance induced by the retarder seems to be smaller than that. The

determined value $\delta = 2\pi \cdot 137/529$ is between the intended $\delta = \pi/2$ and the assumed retardance of $\delta = 2\pi \cdot 142/529$.

Chapter 5

Application of the Transmittance Signal to Improve the Extraction of the Inclination Angle

The previous chapter demonstrated an empirical approach to compensate for deviations of the measured signal caused by the differing system properties of the PM and the LAP. To enable the intended multiscale analysis, it is critical to compensate for the influence of the specific properties of the employed systems. Apart from investigating the connectivity of the brain at different scales, it is also highly relevant to trace the orientation of nerve fibers from their initial segment to their terminal layer in the gray matter. In order to realize this, an additional extension of the standard 3D-PLI analysis is necessary. The standard analysis (see Eq. (2.15)) assumes that the product of the section thickness and the birefringence of the tissue is constant across a brain section ($t \cdot \Delta n = \text{const.} \rightarrow$ cp. Sec. 2.4.5). In reality, however, the section thickness and the birefringence of tissue are variable. The birefringence detected with the employed polarimeters depends on the degree of myelination of the nerve fibers (i.e., the thickness of the myelin sheaths and the number of wrappings), the thickness of fibers, and the fiber density [74–76]. It is reported that these properties vary for different brain areas and types of imaged fibers (cp. Chap. 1). This circumstance is problematic as the standard signal interpretation of 3D-PLI does not consider

this variation. For example, a low retardation signal can be the result of a high inclination angle, a low degree of myelination, a combination of both or crossing fibers.

Especially at the intersection of the white and grey matter, the amount of myelin changes significantly due to the fanning out of fibers [74]. Employing the standard analysis (see Eq. (2.15)), the orientation of nerve fibers appears to suddenly change at the border of the white matter. More specifically, the nerve fibers seem to change their inclination angle and become steeper when fanning out at the white-gray-matter intersection. This is inconsistent with independent studies. The fibers in the gray matter appear to have a high inclination angle (cp. Fig. 2.6, fibers in the gray matter appear blue) which does not match histological findings. However, instead of changing their orientation, the fiber density decreases considerably when the fiber bundles leave the white matter since the fibers have their origin and destination in different cortical layers [74, 76]. The lower fiber density results in a lower myelin density, inducing a lower retardance of the light, which is according to Equation (2.15) falsely interpreted to correspond to fibers with a high inclination angle.

The aim of this chapter is to interpret the measured retardation reliably. Finding a measure to quantify the amount of myelin and incorporating this into the 3D-PLI analysis would solve this problem. The transmittance signal seems to be a feasible measure for this purpose as the attenuation of the light is significantly higher for myelinated axons than for the non-axonal components of the gray matter [26, 30, 32, 33]. The idea that the light attenuation is mainly caused by myelin is further corroborated by a study that describes the possibility to use lightfield microscopy of unstained brain sections as a myelin measure [77]. Thus, a new approach to interpret the measured retardation signal under the consideration of the transmittance signal has been developed. It is based on the assumption that the transmittance signal, i. e. the attenuation of light, is a measure of the myelination and that it is independent of the orientation of the imaged nerve fibers. This assumption was investigated by comparing the transmittance images obtained with 3D-PLI to sections that were specifically stained for myelin. Additionally, the correlation between the transmittance signal and the amount of myelin were analyzed by imaging sections of a human optic tract which was cut into section with different thicknesses. The assumption concerning the

independence of the transmitted light on the nerve fiber orientation was investigated using sections of the same human optic tract which were, in this case, cut under different sectioning angles. It was investigated how this new approach affects the calculated inclination angle of the fibers in comparison to the 3D-PLI standard analysis.

5.1 Transmittance-weighting Approach

For the following considerations it was assumed that the employed retarder in the used polarimetric setup induces a phase shift of $\delta = \pi/2$. Thus, the equations introduced in Chapter 2 are valid.
As pointed out previously, the local change of myelination influences the measured retardation signal. However, this circumstance is not considered in the standard analysis of 3D-PLI, so far. As the attenuation of light is mainly influenced by the absolute amount of myelin in the measured voxel and not by the degree of myelination, only the amount of myelin will be accounted for in the following considerations.
For further investigations, the different components which constitute the gray matter are not going to be discriminated. In accordance with most studies concerning the optical properties of brain tissue [72,78,79], the optical properties of the components of the gray matter are going to be evaluated conjointly. Throughout this thesis, white matter will be referred to as *myelin* with the index m. The neuronal somata and glial cells which mainly constitute the gray matter will be referred to as *non-myelin* with the index $\bar{m}$. In general, the content of each voxel is described as the ratio between the amount of *myelin* (t_m/t_t) and the amount of *non-myelin* components ($t_{\bar{m}}/t_t$). Thus, the total section thickness t_t is given by:

$$\begin{aligned} 1 =& \frac{t_m}{t_t} + \frac{t_{\bar{m}}}{t_t} \\ \Rightarrow t_t =& t_m + t_{\bar{m}} \end{aligned} \tag{5.1}$$

Further on, it is assumed that the myelin sheaths are the only birefringent components in the neuronal tissue ($\Delta n = \Delta n_m$, $\Delta n_{\bar{m}} = 0$). This assumption is commonly used and disregards the minor contribution of microtubuli and neurofilaments to the birefringent net effect [80]. Under consideration of

this assumption, Equation (2.15) can be modified to:

$$\begin{aligned} r &\equiv \left| \sin\left(2\pi \frac{t_t \Delta n}{\lambda} \cos^2(\alpha)\right) \right| \\ &= \left| \sin\left(2\pi \frac{t_m \Delta n_m}{\lambda} \cos^2(\alpha)\right) \right|. \end{aligned} \tag{5.2}$$

The attenuation of light within a certain medium depends on the thickness of the passed medium (t) and special material constants such as the attenuation coefficient (μ). The light attenuation in a transparent medium can be described by the Lambert-Beer-law [81]:

$$I = I_0 e^{-\mu t}. \tag{5.3}$$

If the light passes through brain tissue, the intensity will be attenuated by *myelin* and by *non-myelin* alike:

$$I = I_0 e^{-\mu_t t_t} = I_0 e^{-(\mu_m t_m + \mu_{\bar{m}} t_{\bar{m}})}, \tag{5.4}$$

where μ_m and $\mu_{\bar{m}}$ are the specific attenuation coefficients for the *myelin* and the *non-myelin* components in brain tissue. In order to determine the attenuation coefficients of the *non-myelin* components and the *myelin*, the extreme cases of light attenuation caused only by the *myelin* and only by the *non-myelin* components have to be considered.
If a voxel contains only myelinated axons, the section thickness will coincide with the *myelin* thickness ($t_m = t_t, t_{\bar{m}} = 0$), the retardation signal will be maximal ($r = \max$), and the normalized transmittance signal will be minimal ($I/I_0 = I_m/I_0 = \min$). Thus, Equation (5.3) can be expressed as:

$$\begin{aligned} I = I_0 e^{-\mu_m t_t} &\equiv I_m \\ \Rightarrow t_t \mu_m &= -\ln\left(\frac{I_m}{I_0}\right). \end{aligned} \tag{5.5}$$

Accordingly, if a voxel does not contain any *myelin* ($t_{\bar{m}} = t_t, t_m = 0$), the retardation signal is expected to be zero ($r = 0$) and the normalized transmittance signal to be maximal ($\frac{I}{I_0} = \frac{I_{\bar{m}}}{I_0} = \max$). Hence, the light attenuation is only affected by the thickness of the *non-myelin* part of the tissue and its specific attenuation coefficient. Then, the Lambert-Beer-law

(Eq. (5.3)) is:

$$\begin{aligned} I &= I_0 e^{-\mu_{\bar{m}} t_t} \equiv I_{\bar{m}} \\ \Rightarrow t_t \mu_{\bar{m}} &= -\ln\left(\frac{I_{\bar{m}}}{I_0}\right). \end{aligned} \tag{5.6}$$

To ensure a better flow of reading the index N is introduced for normalized intensities: $\frac{I}{I_0} = I_N$.
The following equation can be solved for the thickness of *myelin*(t_m). The two unknown factors t_m and $t_{\bar{m}}$ can be eliminated by employing the two parameters I_{Nm} and $I_{N\bar{m}}$:

$$\begin{aligned} I_N &\overset{(5.4)}{=} e^{-\mu_t t_t} = e^{-(\mu_m t_m + \mu_{\bar{m}} t_{\bar{m}})} \\ \Leftrightarrow \mu_t t_t &= \mu_m t_m + \mu_{\bar{m}}(t_t - t_m) \\ &= \mu_m t_m + \mu_{\bar{m}} t_t - \mu_{\bar{m}} t_m \\ \Leftrightarrow t_m &= \frac{\mu_t t_t - \mu_{\bar{m}} t_t}{\mu_m - \mu_{\bar{m}}} \\ &\overset{(5.5,5.6)}{=} t_t \frac{(-\ln(I_N) + \ln(I_{N\bar{m}}))}{-\ln(I_{Nm}) + \ln(I_{N\bar{m}})}. \end{aligned} \tag{5.7}$$

Inserting Equation (5.7) into Equation (5.2) results in:

$$r = \left| \sin\left(2\pi \frac{\Delta n_m}{\lambda} \cos^2(\alpha) t_t \frac{\ln(I_{N\bar{m}}) - \ln(I_N)}{\ln(I_{N\bar{m}}) - \ln(I_{Nm})}\right)\right|. \tag{5.8}$$

As can be seen in Equation (5.8), the birefringent signal depends on the total thickness (t_t), birefringence of *myelin* (Δn_m), wavelength of the incident light (λ), inclination angle of the mapped fiber (α) as well as on the actual transmittance signal (I_N), the light attenuation caused only by the *non-myelin* components ($I_{N\bar{m}}$), and the light attenuation caused by *myelin* (I_{Nm}).
As previously mentioned, the amount of *myelin*, the birefringence of *myelin*, and the wavelength can vary. Therefore, the relative thickness (t_{rel}) has been introduced earlier (Chap. 2 $\rightarrow$ cp. Eq. (2.24)). In order to determine the appropriate value for t_{rel}, the retardation value of in-plane fibers with an inclination angle of $\alpha = 0\,^\circ$ (inducing a phase shift of $\delta = \pi/2$) has to be measured. In this case $t_t \rightarrow t_{\lambda/4}$ and $I_N \rightarrow I_{Nm}$ is valid. The derivation is

according to the derivation of Equation (2.24):

$$\begin{aligned} \frac{\pi}{2} &= 2\pi \frac{\Delta n_m}{\lambda} \cdot t_{\lambda/4} \cdot \frac{\ln(I_{N\bar{m}}) - \ln(I_{Nm})}{\ln(I_{N\bar{m}}) - \ln(I_{Nm})} \\ \Leftrightarrow t_{\lambda/4} &= \frac{1}{4} \frac{\lambda}{\Delta n_m}. \end{aligned} \tag{5.9}$$

As mentioned previously in Section 2.4.5, the relative thickness t_{rel} is the ratio between the actual section thickness t_t and the optimal thickness $t_{\lambda/4}$:

$$\begin{aligned} t_{\text{rel}} &= \frac{t_t}{t_{\lambda/4}} \\ \Rightarrow t_t &= t_{\text{rel}}\, t_{\lambda/4} \\ &\overset{5.9}{=} t_{\text{rel}} \frac{\lambda}{4\Delta n_m}. \end{aligned} \tag{5.10}$$

Inserting t_t (5.10) into Equation (5.8) results in:

$$\begin{aligned} r &= \left| \sin\left(2\pi \frac{\Delta n_m}{\lambda} t_{\text{rel}} \frac{1}{4} \frac{\lambda}{\Delta n_m} \cdot \frac{\ln(I_{N\bar{m}}) - \ln(I_N)}{\ln(I_{N\bar{m}}) - \ln(I_{Nm})} \cos^2(\alpha) \right) \right| \\ &= \left| \sin\left(\frac{\pi}{2} t_{\text{rel}} \frac{\ln(I_N) - \ln(I_{N\bar{m}})}{\ln(I_{Nm}) - \ln(I_{N\bar{m}})} \cos^2(\alpha) \right) \right|. \end{aligned} \tag{5.11}$$

The value for I_N is the measured transmittance at each pixel. Thus, each pixel is corrected individually by the measured light attenuation. This modified approach will be referred to as the transmittance-weighting approach in the following.

This modified term for r considers the amount of *myelin* within each voxel individually and corrects the determined value for the relative thickness accordingly. For example, if the measured voxel is located within the white matter where $I = I_m$, the coefficient is one and the calculation of the inclination angle is not affected by the correction. However, if the pixel lies within a gray matter region, the measured value for the transmittance will be smaller than I_m, resulting in a coefficient smaller than one, and thus reducing the effective t_{rel}. Hence, the proposed correlation according to Equation (5.11) only affects the white matter, where the myelination is decreased in comparison to the determined reference value and strongly influences the calculation of the fiber orientation of fibers within the gray matter.

To validate this approach, the PM is used as its measurements are less af-

fected by lateral partial volume effects than the ones of the LAP, and no discrepancy between the peak wavelength of the spectrum and the specified wavelength of the quarter wave retarder were measured.

5.2 Materials and Methods

The transmittance-weighting approach assumes that the light is mostly attenuated by myelin and that the transmittance is independent from the fiber inclination angle. These underlying assumptions are going to be validated in this chapter.

Myelination. In order to evaluate whether the transmittance signal reflects the myelination, brain sections were stained with myelin specific agents. The sections were stained according to a modified Heidenhain-Woelcke technique [9,82] and the Gallyas staining procedure [83], which are both standard procedures to investigate the myelination of brain fibers and allow a qualitative investigation of the amount of myelin [77]. The Heidenhain-Woelcke procedure enables the differentiation of grades of myelination in the white matter, while the Gallyas staining allows the investigation of myelination in the gray matter. The stained sections originated from two different human brains. They were cut with a thickness of 20 µm and imaged employing the TISSUEscope HS scanner by *Huron Digital Pathology Inc.* Due to the limited field of view, the sections were scanned in three line segments and digitally stitched.
For the comparison of the transmittance signal with the sections stained for myelin and to validate the transmittance-weighting approach, the temporal pole of a human brain was prepared according to the standard procedure (cp. Sec. 2.2). The pole was cut frontally into sections with a thickness of 70 µm. The sections were selected to contain comparable brain regions as the myelin stained sections.
Dependency of the transmittance signal. The dependency of the transmittance on the section thickness was investigated employing sections of the optic tract. The same sections as used for the evaluations in Chapter 4 were analyzed. The samples were chosen to have differing section thicknesses and different inclination angles.
It was investigated whether the prerequisite for the transmittance-weighting

approach is fulfilled namely that the transmittance signal is independent of the fiber inclination. For this purpose, the human optic tract was cut under different sectioning angles with respect to the main orientation of the fiber bundle. The sections were imaged with the PM and analyzed according to the 3D-PLI standard procedure.

The images of each section were individually segmented so that only parallel fibers were used for the subsequent evaluation. For the analysis, the normalized transmittance signal was calculated by dividing the measured transmittance image by the background intensity. As described in Chapter 4, the sections for each dataset (same inclination angle and same section thickness) were investigated simultaneously. For each dataset, a histogram was computed and the most frequent value (= mode value), representing the transmittance signal for a certain dataset, was determined. The mode value was chosen as a measure for the representative transmittance value as it is not affected by individual outliers.

Application of the transmittance-weighting approach. After the validation of the assumptions that were made to develop the transmittance-weighting approach, its influence was measured by applying it to whole brain sections. For this purpose, the sections of the temporal pole were measured with the PM according to the 3D-PLI standard procedure. For each tile, the retardation, transmittance and direction images were calculated according to Equations (2.21), (2.23) and (2.22). Then, the individual tiles were stitched and the map of the fiber inclination angle according to Equation (2.24) was calculated. The values for I_m and $I_{\bar{m}}$ were determined manually by observing the transmittance signal for structures with the highest myelin density ($\rightarrow I_m$) and structures that only contain cells and no myelinated axons ($\rightarrow I_{\bar{m}}$). The value for the relative thickness was determined as described in Section 2.4.5. The used value for the relative thickness is $t_{\text{rel}} = 0.9$.

Even though the following considerations were made for several sections, the results shown in this chapter were only retrieved from one section. To visualize the influence of the transmittance-weighting approach for each individual pixel, the measured retardation signal was plotted against the calculated inclination angle. Furthermore, to enable a more quantitative analysis of the influence of the new approach, the inclination angles of fibers running from the main fiber tract into the gray matter were investigated. For this pur-

pose, a line profile across the course of one exemplary fiber was measured with *Fiji* [64]. The evaluation was focused on one fiber. At first, the inclination angle of the fibers was calculated by employing the standard analysis (Eq. (2.24) with a t_{rel} of 0.9). Then, the inclination angle was calculated with the transmittance-weighting approach considering the light attenuation with the previously determined values for I_m and $I_{\bar{m}}$ and $t_{\mathrm{rel}} = 0.9$ (Eq. (5.11)). The profile was measured over a distance of 2000 px.
To emphasize the difference between the current and the transmittance-weighting approach, an ROI displaying the intersection between the white and gray matter in an RGB-FOM was selected. In the RGB-FOM, the fibers that are oriented parallel to the x-axis are labeled in red, fibers oriented parallel to the y-axis in green and fibers parallel to the z-axis in blue (cp. Sec. 2.5). This visualization assumes that all investigated pixels contain fibers. Thus, if a pixel does not contain fibers, the measured retardation signal will be close to zero and will be labeled in blue is according to Equation (2.27). Furthermore, to visualize how the transmittance approach affects the calculation of the inclination angle in comparison to the standard analysis, the difference between the two inclination maps is calculated for each pixel individually:

$$\Delta\alpha = \alpha(r, t_{\mathrm{rel}}) - \alpha(r, t_{\mathrm{rel}}, I_{Nm}, I_{N\bar{m}}). \tag{5.12}$$

5.3 Results

Myelination. In Figure 5.1 3D-PLI transmittance images (A, C) of a coronal human brain section are opposed to myelin stained sections (B, D). In all cases, the light was stronger attenuated in the white matter than in the gray matter. The appearance of the section stained according to the modified Heidenhain-Woelcke protocol [9] (B) and the 3D-PLI transmittance image (A) are very similar regarding the texture of the white matter. For example, the contrast of the capsula extrema (green ellipse, bright line) and the surrounding appear very bright in both modalities. The appearance of the centrum semi ovale (blue circle) is similar within the stained image and the transmittance image. In both cases, the circled area appeared bright, while lower intensities were observed closer to the white-gray-matter-intersection. Despite these similarities, there also appeared to be gradients of the gray value in the white matter. The red ellipse points out such differences. In this case, the cingulum (cg) appears darker than the corpus callosum (CC) in the 3D-PLI transmittance image, while within the stained image the intensities of the two brain areas are reversed. Furthermore, within the stained section (B), a gradual decrease in intensity towards the bottom of the section is visible, which is not apparent in the 3D-PLI transmittance image.
While the Heidenhain-Woelcke stained section provides enough contrast to investigate the amount of myelin in the white matter, it does not provide enough information in the gray matter. In opposition to the Heidenhain-Woelcke stained images, display the contrast enhanced 3D-PLI transmittance image and the Gallyas stained section (shown in Fig. 5.1 C and D) a gradual decrease in myelination towards the surface of the brain. The change of myelin is more clearly visible in the Gallyas stained section than in the 3D-PLI transmittance image. Nevertheless, the stripe of Baillarger (magenta arrows in C and D) is visible in both modalities.
Dependency of transmittance signal. The analysis of the sections with the optic tract cut under different section thicknesses also shows a correlation between the amount of myelin in the light path and the measured transmittance signal. The transmittance signal increases with decreasing section thickness (Fig. 5.2). This trend is observable for all investigated inclination angles. The lowest transmittance signal was measured for a section thickness of 100 µm, while the highest was measured for 20 µm.

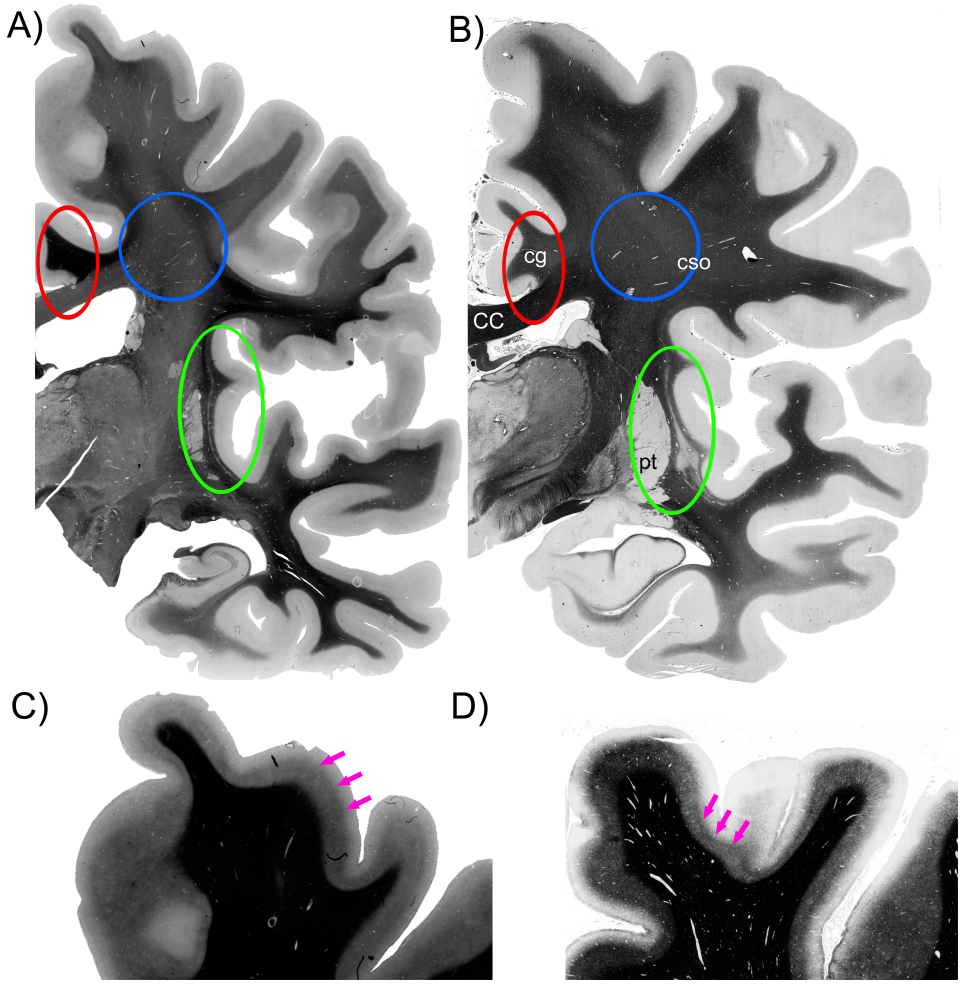

Figure 5.1: Distribution of myelin. Visual comparison of sections stained according to the Heidenhain-Woelcke (B) and the Gayllas (D) procedure with transmittance images obtained with the PM (A, C). The blue and green ellipses emphasize similarities of the two modalities while the red ellipse points out differences. The Gayllas and the contrast enhanced transmittance image (C, D) show the Baillarger stripe (magenta arrows). (CC - corpus callosum, cg - cingulum, cso - centrum semi ovale, pt - putamen).

The analysis of the optic tract sections revealed no explicit dependency of the amount of transmitted light on the inclination angle of the imaged fibers. The error in the measurements of the transmittance signal were independent from the section thickness and the inclination angle of the investigated section.

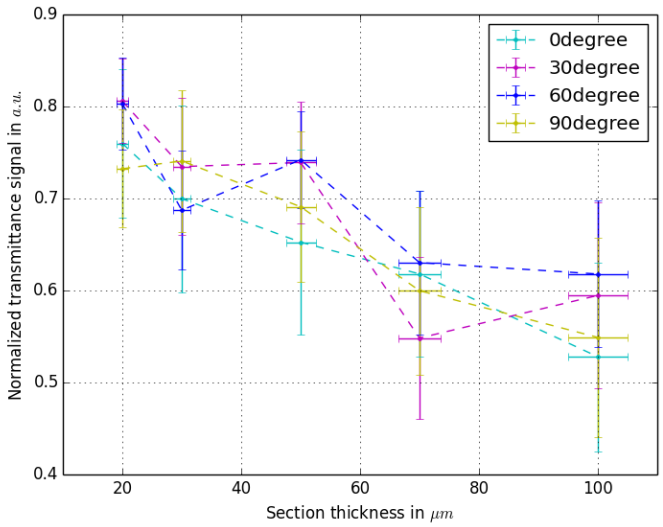

Figure 5.2: Dependency of the transmittance signal on the section thickness and fiber inclination angle measured with the PM, employing the sections of the optic tract.

Application of the transmittance-weighting approach. The previous measurements were executed to verify that the prerequisites for the transmittance-weighting approach are given. The further studies were performed on whole brain sections to investigate the influence of this approach on the reconstruction of nerve fiber orientations. Figure 5.3 shows the measured retardation values versus the calculated inclination angles which were obtained using the standard analysis (Eq. (2.15)) and the inclination angles calculated using the transmittance-weighting approach (Eq. (5.11)). The standard analysis assigns one measured retardation value to a distinct inclination angle (pink line). In contrast, the transmittance-weighting approach enables the correlation of different retardation values to one inclination angle (area under the pink line). For example, for the standard analysis, fibers with an inclination angle of $\alpha = 50\,^\circ$ correspond to a retardation value of $r = 0.45$. This is a fixed correlation. A certain retardation value always

corresponds to a certain inclination angle. Employing the transmittance-weighting approach, it is possible to correlate multiple retardation values to a certain inclination angle. Thus, depending on the myelination of fibers with an inclination of $\alpha = 50\,^{\circ}$, a retardation value between 0.0 and 0.45 is measured. Still, a value close to 0.45 is more likely to be measured than 0.0, as indicated by the color coding.
Within the scatterplot (Fig. 5.3), two major areas are visible where the data points are accumulated. The lower part was caused by measurements of fibers in the gray matter, which induced a low retardation signal ($r < 0.2$). The majority of fibers have an inclination angle of $20\,^{\circ}$ or steeper. In contrast, the upper part was caused by values in the white matter. The fibers in the white matter resulted in retardation values between 0.0 and 0.7, corresponding to fiber inclination angles from $0\,^{\circ}$ to $90\,^{\circ}$.

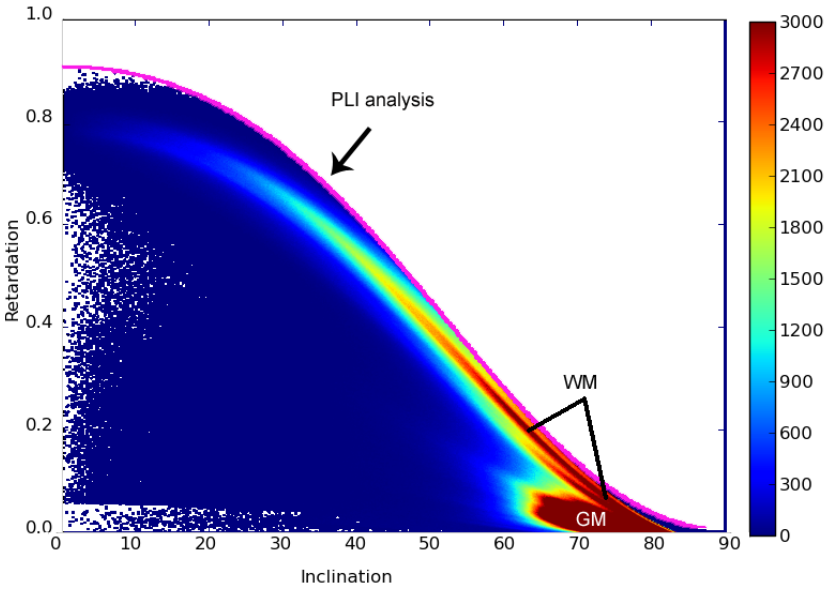

Figure 5.3: Scatterplot visualizing the correlation between the measured retardation value and the calculated fiber inclination angle employing the standard analysis (purple line) and the transmittance-weighting approach (area under the curve). The frequency of the occurring data pair (retardation-inclination) were color coded. The white matter (WM) and the gray matter (GM) show distinct frequencies for the occurring data pairs.

The change of retardation signal and the consequence for the retrieved fiber inclination angle is demonstrated in Figure 5.4. The retardation signal de-

creases continuously from the white matter to the gray matter (Fig. 5.4 A). At the border of the white matter, the single fibers fan out. Using the standard analysis, the inclination angle of the fibers seem to increase continuously from $\alpha = 50\,^\circ$ up to $\alpha = 80\,^\circ$ over a distance of 2000 px $\hat{=}$ 2.66 mm (Fig. 5.4 B, green line). Using the information of the transmittance and weighting the retardation with it, the calculated inclination angle fluctuated around 40 ° (Fig. 5.4 B, red line). No distinct increase of the inclination angle was measured. The profile retrieved with the transmittance-weighting approach is noisier than the profiles calculated with the standard analysis.

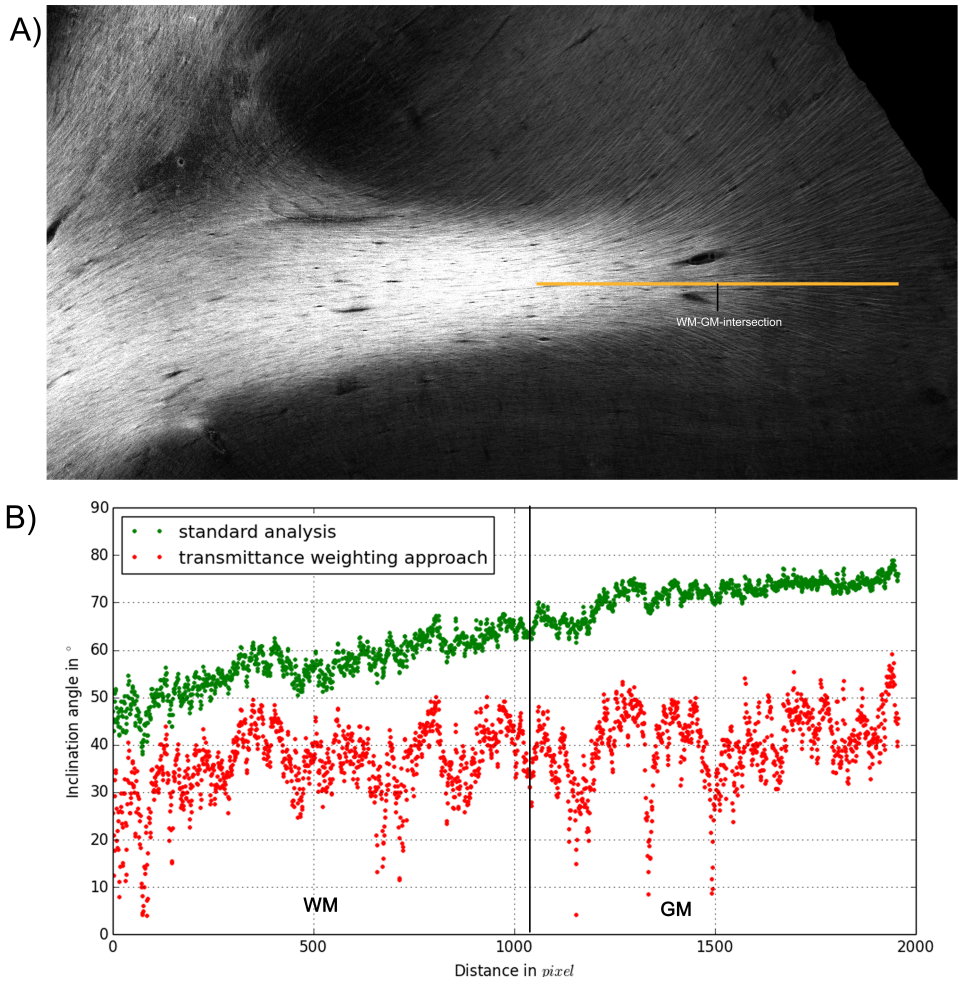

Figure 5.4: Comparison of the inclination angle calculated with the standard analysis and the transmittance-weighting approach at the white-gray-matter intersection. (A) Within the retardation image, the course of the fibers can be seen. (B) Profile of fiber inclination angle reconstructed with standard analysis (green line) and the transmittance-weighting approach (red line).

In Figure 5.5, the orientations of the fibers of the same region of interest as shown in Figure 5.4 are shown employing the introduced color coding (cp. Sec. 2.5). The orientations were reconstructed with the standard analysis (Fig. 5.4 A) and the transmittance-weighting approach (B). The RGB-FOM reflects the information about the fiber orientation. For example, fibers in area 1 have a low inclination angle and are parallel to the x-axis, hence they are labeled red. Employing the standard analysis, the reconstructed fibers appear to change their orientation when leaving the main fiber bundle and run along the z-axis (area 2). Applying the transmittance-weighting approach, the orientation of the fibers were labeled red indicating that the fibers are parallel to the x-axis. The fibers in areas 3 and 4 still appear to have a high inclination angle and hardly are affected by the transmittance-weighting approach. Only a pale shade of red and green appears there, denoting a high inclination angle.
Figure 5.5 C demonstrates where and how the transmittance-weighting approach changes the interpretation of the retardation signal. Modest differences of the calculated inclination angle with the standard analysis and with the transmittance-weighting approach are visible in the white matter. Here, the calculated angle maximally changed by 30 °. All inclination angles measured with the transmittance-weighting approach are similar or smaller than those calculated with the standard analysis.
The closer the investigated fibers were to the surface of the brain, the stronger the fiber orientation reconstruction was affected by the transmittance. In the gray matter, the inclination angle was changed up to 50 °. With the current approach, inclination values around 72 ° were measured (bright green area), while with the transmittance-weighting approach, inclination angles around 38 ° are calculated. Figure 5.5 C illustrates the transmittance-weighting approach has the largest impact in the reconstruction of fibers in the gray matter and only a small impact on fiber tracts within the white matter as intended by design.

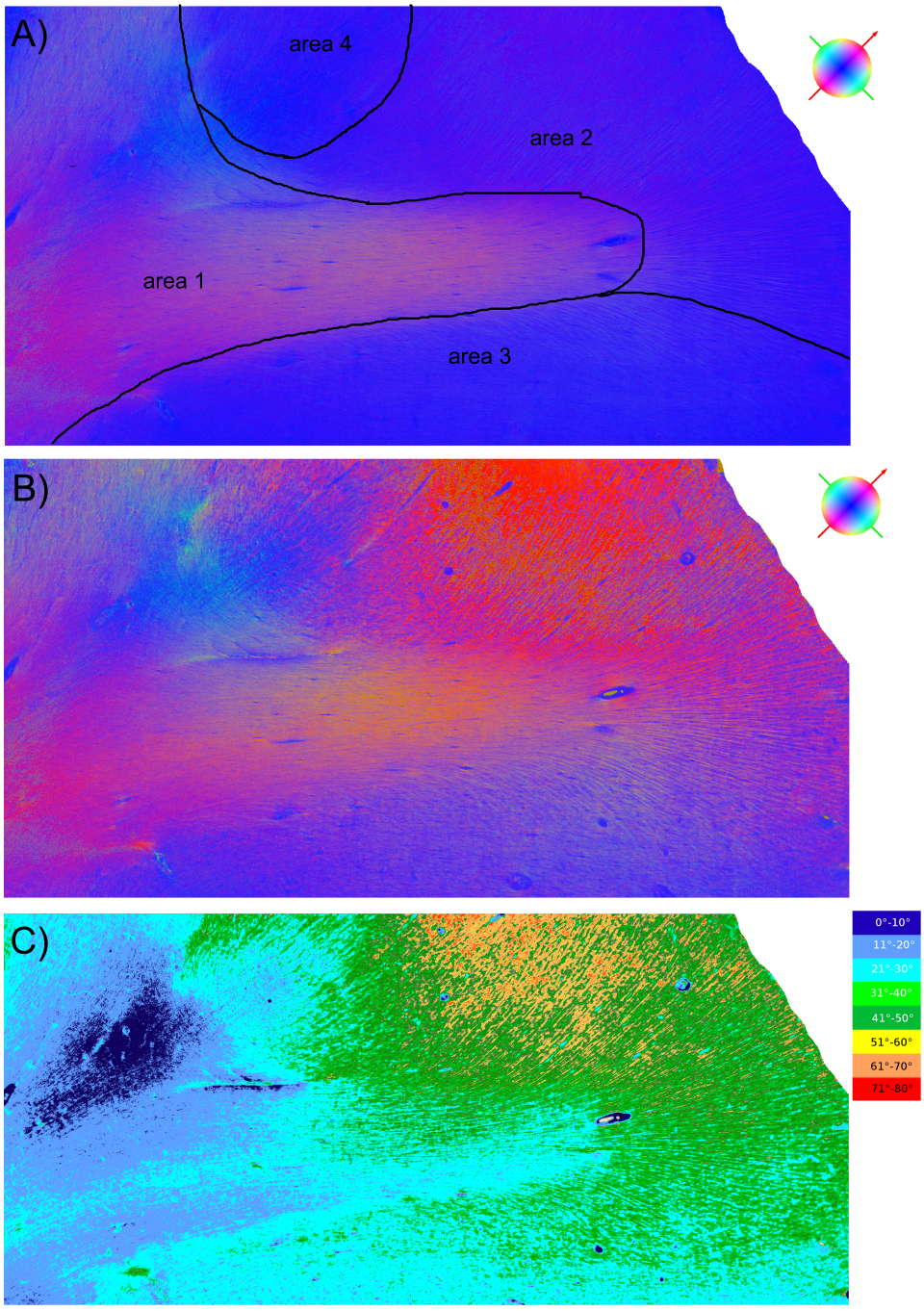

Figure 5.5: Fiber orientation maps. The fiber orientations were reconstructed with standard analysis (A) and the transmittance-weighting approach (B). (C) displays the difference of the fiber inclination angle calculated according to the standard analysis and the transmittance-weighting approach.

5.4 Discussion

The comparison of the myelin stained sections and the 3D-PLI transmittance images confirmed the assumption that the light attenuation is mainly caused by myelin. Even though the staining of postmortem sections is a standard procedure to investigate the myelination, it is only a qualitative method [9] since staining techniques are sensitive to tissue quality, preparation procedure, and immersion time.
The overall light attenuation in the transmittance image depends indeed on the amount of myelin, even though differences between the images of the stained sections and the transmittance obtained with 3D-PLI are apparent. It was ensured that the majority of the imaged brain structures were visible in all of the three displayed sections, although it was not possible to match the sections perfectly. Some of the observed differences are caused by the inter-individual variety of the shape of brain structures and slightly different sectioning planes. Furthermore, the staining techniques are flawed and lead to visible variations (cp. Fig. 5.1 B) where the myelin content seems to decrease gradually towards the bottom of the section. This gradual decrease was not evident in neighboring sections and proved to be caused by an inhomogeneous distribution of the used dye rather than a change of the amount of myelin.
The measurements with the optic tract further affirm that the light attenuation is strongly influenced by the amount of myelin. The rather large deviations of the normalized transmittance signals from the mode value were caused by the inhomogeneities of the tissue as discussed in detail in Chapter 4.
Furthermore, it was confirmed that the measured signal does not depend on the nerve fiber inclination with the performed studies. The measured transmittance signal was similar for all inclination angles. The measured deviations were within the margins of error. As far as the 3D-PLI measurements and the employed tissue preparation are concerned, the transmitted intensity only depends on the section thickness and not on the fiber inclination angle. In contrast, Hebeda et al. [29] observed a high variation of light attenuation up to 70 % depending on the fiber orientation, which was not observed within the studies performed in this work. The studies performed by Hebeda et al. differed from the ones executed within this thesis. They

used laser light with $\lambda = 633\,\text{nm}$ and a small volume of postmortem brain tissue. They inserted an optical fiber parallel to the brain fibers. The nerve fibers as such seemed to work as light conductors, transporting the light along the nerve fiber. A higher amount of light was transmitted parallel to the fiber axes rather than perpendicular to it. In 3D-PLI diffuse light is employed, prohibiting that a significant amount of light is conducted through $90\,°$-fibers.

The previous measurements have proved that all requirements are fulfilled to apply the transmittance-weighting approach. The further studies concentrated evaluating the effect of this approach concerning the reconstruction of the nerve fiber orientation in comparison to the standard analysis. The standard analysis assumed a constant relative thickness t_{rel} across a brain section (cp. Sec. 2.4.5). According to Equation (2.15), a certain fiber inclination angle corresponds to a distinct retardation value. In this case, a low retardation value always corresponds to a high inclination angle, although a low myelination could be the cause of the low signal. For example, at the white-gray-matter intersection, a gradual decrease of the retardation values is measured due to the fanning out of the fibers. With the standard analysis, this change of retardation value is interpreted as a change of fiber inclination. This phenomenon is observed for the complete gray matter. However, in reality, the fibers do not severely change their orientation when fanning out. The decrease of the retardation signal is not caused by the change of inclination angle but rather by the change of fiber density resulting in different amounts of myelin per voxel.

Employing the transmittance-weighting approach, it is possible to consider such changes in fiber density and myelination. This enables the tracing of nerve fibers to their terminal layers, as displayed with the profiles visualizing the inclination angles of fibers at the gray-white-matter intersection. Considering the amount of myelin, the inclination angle of the nerve fibers did not change. Furthermore, the calculation of the inclination angle with the transmittance-weighting approach is more affected by noise than the one with the standard analysis, as visible in the line profile (cp. Fig. 5.4). When employing the transmittance-weighting approach, the inclination angle is calculated considering two instead noise affected measures, which increases the uncertainty of the inclination angle as compared to the standard 3D-PLI approach.

The observation of a constant fiber inclination angle is consistent with previous observations [74, 76]. In general, the application of the transmittance-weighting approach to reconstruct the fiber inclination proved that employing the transmittance as a measure of myelin significantly improves the reconstructed fiber orientation and enables the tracing of nerve fibers from the white matter into the gray matter.
The RGB-FOMs (Fig. 5.5) visualized the difference of the fiber orientation retrieved with the standard analysis and the transmittance-weighting approach for a larger region of interest. The transmittance-weighting approach induces small changes of the fiber orientation in the white matter in comparison to the standard analysis. The transmittance-weighting approach has its largest impact on fiber tracts with a different amount of myelin compared to the white matter, as seen in Figure 5.5 B area 2. However, within the brain, crossing fibers also decrease the measured retardation signal. This influence on the other hand cannot be compensated with the transmittance-weighting approach. Such areas were visible in Figure 5.5 B area 3 and 4. Furthermore, as intended, only brain structures containing fibers are affected by this approach.
The new approach enables a more reliable estimation of the nerve fiber orientation in the gray matter and preserves the information of fibers which constitute the white matter as intended by design.

Chapter 6

Conclusion

The aim of this work was to enhance the quality and analysis of 3D-PLI signals. The introduced corrections enable a multiscale analysis of nerve fiber architecture of the brain. It is now possible to employ both polarimetric setups which have different optical resolutions and to obtain the comparable orientations of the measured fibers. By combining the knowledge gained by employing both systems it is possible to investigate single fibers as well as bundles of fibers. These further developments of 3D-PLI provide the opportunity to gain a more comprehensive knowledge about the nerve fiber architecture of the human brain. This provides the possibility of new diagnostics and treatments of brain diseases.

The optimization and characterization of the employed 3D-PLI setups were essential for solving the multiscale challenge and to enable the transmittance-weighting approach. The measurements for the characterization showed that the components of the PM are perfectly suited for 3D-PLI. The signal quality of the LAP could be improved by replacing the illumination wavelength and the polarization filters. In the future, it is highly desirable to match the illumination wavelength with the quarter-wave retarder to simplify the extraction of the retardation and transmittance measurements.

Replacing the filters with higher quality components is difficult due to their unusual large size. The characterization of the filters revealed that the light after the first linear polarizer is not completely polarized. This causes uncertainties in the measurements as the Jones matrix formalism is only correct for fully polarized light. This should further be investigated. By employing Mueller instead of Jones matrices it would possible to retrieve a correct de-

scription of the optical components and reduce this uncertainty.
The performed characterization further provides the foundation to easily integrate an additional polarimeter if desired. By developing an additional one-shot polarimeter with a smaller field of view, it is possible to increase the efficiency of mapping the nerve fiber architecture of smaller brains, such as rodent brains. The integration of such an additional polarimeter into the workflow can be realized by measuring the PECF and the optical lateral resolution limit. This is only feasible as the multiscale analysis, incorporating different polarimeters, was successfully realized. It is now possible to link the gained knowledge about the microscopical fiber architecture in particularly interesting brain regions such as the hippocampus with the macroscopical brain architecture.
By employing the correct mathematical description that considers the actual retardance that the retarder implemented in the LAP induces, the comparability of the data obtained with the LAP and the PM is ensured. With the current setups the transmittance-weighting approach can only be applied to the data obtained with the PM. The implementation of the transmittance-weighting approach for the LAP should be realized within the near future. Instead of adapting the transmittance-weighting approach to the different analysis which is necessary to interpret the LAP measurements, it is highly desirable to eliminate the wavelength discrepancy. This could be done by either using a suited bandpass filter or replacing the current retarder or the current light source.
For a complete brain reconstruction a detailed understanding of the partial volume effects is necessary. The performed studies within this thesis represent the first reported approach to evaluate and compensate the influence of the partial volume effects on 3D-PLI measurements. The proposed correction function to compensate for lateral partial volume effects could be realized by employing Stokes parameters. These parameters were proposed by Rieppo et al. to be able to describe different constellations of fiber tissue [84].
The performed studies showed that an experimental investigation of the partial volume effects is challenging due to the heterogeneity of biological tissue. Thus, in future studies, measurements of phantoms containing artificially grown fibers, which are not available yet, in combination with extensive simulations, have to be performed. This approach is essential to

enable the mapping of brain regions based on the orientation and distribution of nerve fibers. However, the knowledge gained by the downsampling experiments provides further possibilities. So far, with 3D-PLI it is possible to assign a single predominant/prevailing fiber orientation to a measured voxel. If fibers with different orientations are present within one voxel, the measured signal is difficult to interpret. The comparison of LAP data with averaged PM data could be used to gain knowledge about the homogeneity of the fiber distribution measured within each LAP pixel. The larger the difference between the measured retardation values in the LAP is to the averaged value of the corresponding 48×48 pixels, the larger is the influence of lateral partial volume effects. Thus, the current description of a single fiber orientation per voxel has to be extended to account for the reality of multiple fibers per voxel. This modification is especially necessary for the measurements with the LAP. Such an extension could be realized by replacing the current model with optical density functions (ODFs). This approach could significantly improve the 3D-tracking of fibers basedn on 3D-PLI data. An additional accomplishment is the extraction of the orientation of single nerve fibers in the gray matter, which was not possible before. By means of the weighting of the retardation signal with the transmittance, different concentrations of myelin are considered. This improves the tracing of the nerve fiber architecture within the complete brain significantly. The biggest success of this approach was demonstrated in the gray matter, as the large error of the determined inclination angle of single fibers was significantly reduced. This approach could further be improved by utilizing the signal of the backscattered light. In contrast to the transmittance signal, where *myelin* and *non-myelin* reduce the incident light, only *myelin* contributes to the backscattered signal.

The presented work facilitates a multiscale analysis of the human brain. It paves the way to establish 3D-PLI as a bridging technology between microscopical and macroscopical imaging techniques. Further, it provides the first approach to trace fibers from the main fiber bundles to their terminal layers in the gray matter.

Bibliography

[1] "Human brain project - report," (2013).

[2] NIH, "Brain initative." http://www.nih.gov/science/brain/ (2013).

[3] Zilles, K. and Rehkaemper, G., [Funktionelle Neuroanatomie: Lehrbuch und Atlas], Springer, 3 ed. (1998).

[4] Kandel, E. R. and Jessel, T., [Principles of Neural Science], McGraw-Hill, 4th ed. (2000).

[5] Jurrus, E., Hardy, M., Tasdizen, T., Fletcher, T. P., Koshevoy, P., Chien, C.-B., Denk, W., and Whitaker, R., "Axon tracking in serial block-face scanning electron microscopy," Medical image analysis **13**, 180–188 (2009).

[6] Axer, H. and Keyserlingk, D., "Mapping of fiber orientation in human internal capsule by means of polarized light and confocal laser microscopy," J. Neursci. Methods **94**, 165–175 (2000).

[7] Li, A., Gong, H., Zhang, B., Wang, Q., Yan, C., Wu, J., Liu, Q., Zeng, S., and Luo, Q., "Micro-optical sectioning tomography to obtain a high-resolution atlas of the mouse brain," Science **330**, 1404–1408 (201).

[8] Buergel, U., Amunts, K., Hoemke, L., Mohlberg, H., Gilsbach, J., and Zilles, K., "White matter fiber tracts of the human brain: Three-dimensional mapping at microscopic resolution topography and intersubject variability," Neuroimage **29**, 1092–1105 (2006).

[9] Buergel, U., Mecklenburg, I., Blohm, U., and Zilles, K., "Histological visualization of long fiber tracts in the white matter of adult human brains," Journal of Brain Research **38**, 397–404 (1997).

[10] Koebbert, C., Apps, R., Bechmann, I., Lanciego, J. L., Mey, J., and Thanos, S., "Current concepts in neuroanatomical tracing.," Progress in Neurobiology **62**, 327–351 (2000).

[11] Galuske, R. A., Schlote, W., Bratzke, H., and Singer, W., "Interhemispheric asymmetries of the modular structure in human temporal cortex," Science **289**, 1946–1949 (2000).

[12] Tardif, E. and Clarke, S., "Intrinsic connectivity of human auditory areas: a tracing study with Dii," Eur J Neuroscience **13**, 1045–1050 (2001).

[13] Klingler, J., "Erleichterung der makroskopischen Praeparation des Gehirns durch den Gefrierprozess," Schweizer Archiv fuer Neurologie und Psychiatrie **36**, 247–256 (1935).

[14] Mori, S., [Introduction to Diffusion Tensor Imaging.], Elsevier B.V (2007).

[15] Mori, S. and Zhang, J., "Principles of diffusion tensor imaging and its applications to basic neuroscience research," Neuron **51**(5), 527–539 (2006).

[16] Peuskens, D., van Loon, J., Van Calenbergh, F., Van den Bergh, R., Goffin, J., and Plets, C., "Anatomy of the anterior temporal lobe and the frontotemporal region demonstrated by fiber dissection," Neurosurgery **55**, 1174 (2004).

[17] Tuere, U., Yasargil, M. G., Friedmann, A. H., and Al-Mefty, O., "Fiber dissection technique: lateral aspect of the brain," Neurosurgery **47**, 417–427 (2000).

[18] Johansen-Berg, H. and Behrens, T. E., [Diffusion MRI: From Quantitative Measurement to In vivo Neuroanatomy], Elsevier, 1st ed. (2009). ISBN: 978-0-12-374709-9.

[19] Roebroeck, A., Galuske, R., Formisano, E., Chiry, O., Bratzke, H., Ronen, I., Kim, D., and Goebel, R., "High-resolution diffusion tensor imaging and tractography of the human optic chiasm at 9.4 T," Neuroimage **39(1)**, 157–68 (2008).

[20] Goethlin, G., "Die Doppelbrechenden Eigenschaften des Nervengewebes - Ihre Ursachen und ihre biologischen Konsequenzen," Kungl. Svenska Vetenskapsakad. Handl. **51**, 1–92 (1913).

[21] Schmidt, W., "Zur Doppelbrechung des Nervenmarks," Zeitschrift fuer wissenschaftliche Mikroskopie und mikroskopische Technik **41**, 29–38 (1923).

[22] Schmitt, F. and Bear, R., "The optical properties of vertebrate nerve axons as related to fiber size," Journal of Cellular and Comparative Physiology **9**(2), 261–273 (1937).

[23] Wolman, M., "Polarized-light microscopy as a tool of diagnostic pathology - Review," Journal of Histochemistry and Cytochemistry **23**(1), 21–50 (1975).

[24] Hildebrand, C., Remahl, S., Persson, H., and Bjartmar, C., "Myelinated nerve fibres in the CNS," Progress in Neurobiology **40**(3), 319 – 384 (1993).

[25] Campbell, N., Reece, J. B., and Markel, J., [Biologie], vol. 6th, Spektrum Akademischer Verlag, Heidelberg-Berlin (2003).

[26] Eggert, H. and Blazek, V., "Optical properties of human brain tissue, meninges, and brain tumors in the spectral range of 200 to 900 nm," Neurosurgery **Oct;21(4)**, 459–64 (1987).

[27] Sterenborg, H. J. C. M., Van Gemert, M. J. C., Kamphorst, W., Wolbers, J. G., and Hogervorst, W., "The spectral dependence of the optical properties of human brain," Lasers in Medical Science **4**, 221–227 (1989,).

[28] van der Zee, P., Essenpreis, M., and Delpy, D. T., "Optical properties of brain tissue," Proc. SPIE 1888, Photon Migration and Imaging in Random Media and Tissues **454** (1993).

[29] Hebeda, K. M., Menovsky, t., Beek, J., Wolbers, J., and van Gemert, M., "Light propagation in the brain depends on nerve fiber orientation," Neurosurgery **11**, 35(4):720–2 (1994).

[30] Schwarzmaier, H.-J., Yaroslavsky, A. N., Yaroslavsky, I. V., Goldbach, T., Kahn, T., Ulrich, F., Schulze, P. C., and Schober, R., "Optical properties of native and coagulated human brain structures," Proc. SPIE 2970, Lasers in Surgery: Advanced Characterization, Therapeutics, and Systems VII **492** (1997).

[31] Johns, M., Giller, C., and H., L., "Computational and in vivo investigation of optical reflectance from human brain to assist neurosurgery.," Journal of Biomedical Optics **3(4)**, 437–45 (1998).

[32] Wang, H., Black, A. J., Zhu, J., Stigen, T. W., Al-Qaisi, M. K., Netoff, T. I., Abosch, A., and Akkin, T., "Reconstructing micrometer-scale fiber pathways in the brain: Multi-contrast optical coherence tomography based tractography," NeuroImage **58**, 984–992 (2011).

[33] Svaasand, Lars, O. and Ellingsen, R., "Optical properties of human brain," Photochemistry and Photobiology **38**(3), 293–299 (1983).

[34] Quarles, R. H., Macklin, W., and Morell, P., [Basic Neurochemistry: Molecular, Cellular and Medical Aspects], ch. 4 - Myelin Formation, Structure and Biochemistry, 51–71, Elsevier Inc., 7th ed. (2006).

[35] Huang, X.-R. and Knighton, R., "Microtubules contribute to the birefringence of the retinal nerve fiber layer," Investigative Ophthalmology and Visual Science **46(12)**, 4588–4593 (2005).

[36] Bear, R., "The structure of the myelin sheath. optical studies," Neurosciences Research Program bulletin **9**, 507–510 (1971).

[37] Martenson, R. E., [Myelin: Biology and Chemistry], CRC Press, USA (1992).

[38] Buller, S., "Brain Tissue Preparation for Polarized Light Imaging," Minor thesis (October 2013).

[39] Axer, M., Amunts, K., Graessel, D., Palm, C., Dammers, J., Axer, H., Pietrzyk, U., and Zilles, K., "A novel approach to the human connectome: Ultra-high resolution mapping of fiber tracts in the brain," NeuroImage **54**(2), 1091–1101 (2011).

[40] Schober, M., Schloemer, P., Cremer, M., Mohlberg, H., Huynh, A.-M., Schubert, N., Zilles, K., and Amunts, K., "How to generate a reference volume for subsequent 3d-reconstruction of histological sections," Proceeding BVM (2015).

[41] Wood, I. G. and Glazer, A. M., "Ferroelastic phase transition in BiVO4. I. birefringence measurements using the rotating-analyser method," Journal of Applied Crystallography **13**, 217–223 (1980).

[42] Glazer, A. M., Lewis, J. G., and Kaminsky, W., "An automatic optical imaging system for birefringent media," Proceedings of the Royal Society A **452**, 2751–2765 (1996).

[43] Mueller, H., "Memorandum on the polarization optics of the photoelastic shutter." Report No. 2 of the OSRD project OEMsr-567 (1943).

[44] Larsen, L., Griffin, L. D., Graessel, D., Witte, O. W., and Axer, H., "Polarized light imaging of white matter architecture," Microscopy research and technique **70**(10), 851–863 (2007).

[45] Axer, M., Graessel, D., Kleiner, M., Dammers, J., Dickscheid, T., Reckfort, J., Huetz, T., Eiben, B., Pietrzyk, U.and Zilles, K., and Amunts, K., "High-resolution fiber tract reconstruction in the human brain by means of three-dimensional polarized light imaging," Frontiers in NEUROINFORMATICS **5**(34), 1–13 (2011).

[46] Demtroeder, W., [Experimentalphysik 2 - Elektrizitaet und Optik], Springer-Verlag Berlin Heidelberg (2009).

[47] Jones, R., "A new calculus for the treatment of optical systems I. description and discussion of the calculus," Journal of the Optical Society of America **31**(7), 488–493 (1941).

[48] Jones, R., "A new calculus for the treatment of optical systems IV," Journal of the Optical Society of America **32**, 486–493 (1942).

[49] de Visser, S., Bowden, J., Wentrup-Byrne, E., Rintoul, L., Bostrom, T., Pope, J., and Momot, K., "Anisotropy of collagen fibre alignment in bovine cartilage: comparison of polarised light microscopy and spatially resolved diffusion-tensor measurements," Osteoarthritis and Cartilage **16**(6), 689 – 697 (2008).

[50] Jones, D. K. and Pierpaoli, C., "Confidence mapping in diffusion tensor magnetic resonance imaging tractography using a bootstrap approach," Magnetic Resonance in Medicine **53**(5), 1143–1149 (2005).

[51] Jellison, B. J., Field, A., Medow, J., Lazar, M., Salamat, M., and A.L., A., "Diffusion tensor imaging of cerebral white matter: A pictorial review of physics, fiber tract anatomy and tumor imaging patterns," American Journal of Neuroradiology **25**, 356–369 (2004).

[52] Oldenbourg, R. and Shribak, M., [Handbook of Optics - Volume I - Geometrical and Physical Optics, Polarized light, Components and Instruments], vol. 1, ch. 28 - Microscopes, 28.1 – 28.24, The McGraw-Hill companies (2010).

[53] Paul, R., [Halbleiterdioden - Grundlagen und Anwendungen], Dr. Alfred Huethig Verlag Heidelberg (1976).

[54] Dammers, J., Axer, M., Graessel, D., Palm, C., Zilles, K., Amunts, K., and Pietrzyk, U., "Signal enhancement in polarized light imaging by means of independent component analysis," NeuroImage **49**(2), 1241–1248 (2010).

[55] Land, Edwin, H., "Some aspects of the development of sheet polarizers," Journal of optical society of America **41**(12), 957–962 (1951).

[56] Bennet, J. H., [Handbook of Optics - Volume I - Geometrical and Physical Optics, Polarized light, Components and Instruments], vol. 1, ch. 13 - Polarizer, The McGraw-Hill companies (2010).

[57] Optics, E., "Introduction to polarization," tech. rep., Edmunds optics world wide (2014).

[58] cvi Melles Griot, "Waveplates," product guide, cvi Melles Giot (2009).

[59] Chipman, R. A., [Handbook of Optics - Volume I - Geometrical and Physical Optics, Polarized light, Components and Instruments], vol. 1, ch. 15.23 Dual rotating retarder polarimeter, 15.16, The McGraw-Hill companies (2010).

[60] Oldenbourg, R., Salmon, E., and Tran, P., "Birefringence of single and bundled microtubules," BIOPHYSICAL JOURNAL **74**(1), 645–654 (1998).

[61] Hecht, E., [Optik], vol. 4th, Oldenbourg Wissenschaftsverlag GmbH (2005).

[62] Michelson, A., "Studies in optics," Studies in optics **1** (1927).

[63] Burger, W. and Burge, M. J., [Principles of Digital Image Processing - Fundamental Techniques], Springer (2009).

[64] Schindelin, J., Arganda-Carreras, I., Frise, E., Kaynig, V., Longari, M. Pietzsch, T., Preibisch, S. Rueden, C., Saalfeld, S., Schmid, B., Tinevez, J.-V., White, D. J., Hartenstein, V., Eliceiri, K., Tomancak, P., and Cardona, A., [Fiji: an open-source platform for biological-image analysis], vol. 9 (2012).

[65] Kleiner, M., Axer, M., Graessel, D., Reckfort, J., Pietrzyk, U., Amunts, K., and Dickscheid, T., "Classification of ambiguous nerve fiber orientations in 3d polarized light imaging," Proceeding Medical Image Computing and Computer Assisted Science (MICCAI) **7510**, 206–213 (2012).

[66] ISO, "ISO 14524:2009 Photography – Electronic still-picture cameras – methods for measuring opto-electronic conversion functions (OECFs)," tech. rep., ISO (2009).

[67] Kucacki, E., "Waveplates offer precise control of polarization," product guide, Institute of Physics and IOP Publishing Ltd (2006).

[68] Goldstein, D., [Polarized light], CRC Press Taylor & Francis Group 6000 Broken Sound Parkway NW, Suite 300 Boca Raton, FL 33487-2742, 3rd ed. (2011).

[69] Rousset, O. G., Ma, Y., and Evans, A. C., "Correction for partial volume effects in PET: principle and validation," J Nucl Med **39**, 904–11 (1998).

[70] Matsuda, H., Ohnishi, T., Asada, T., Li, Z.-J., Kanetaka, H., Imabayashi, E., Tanaka, F., and Nakano, S., "Correction for partial-volume effects on brain perfusion SPECT in healthy men," J Nucl Med **44(8)**, 1243–1252 (2003).

[71] Tournier, J.-D., Calamante, F., Gadian, D. G., and Connelly, A., "Direct estimation of the fiber orientation density function from duffusion-weighted mri data using spherical deconvolution," NeuroImage **23**, 1176–1185 (2004).

[72] Axer, H., Axer, M., Krings, T., and Graf v. Keyserlingk, D., "Quantitative estimation of 3-D fiber course in gross histological sections of the human brain using polarized light," Journal of Neuroscience Methods **105**, 121–131 (2001).

[73] Yoo, T., Ackerman, M., Lorensen, W., Schroeder, W., Chalana, V., Aylward, S., and et al., "Engineering and algorithm design for an image processing API: a technical report on ITK-the insight toolkit," Studies in health technology and informatics , 586–592 (2002).

[74] Vogt, O., "Zur anatomischen Gliederung des Cortex cerebri," J. Pychol Neurol **2**, 160–180 (1903).

[75] Braitenberg, V., "A note on myeloarchitectonics," J Comp Neurol **118**, 249–348 (1962).

[76] Nieuwenhuys, R., "The myeloarchitectonic studies on the human cerebral cortex of the vogt-vogt school, and their significance for the interpretation of functional neuroimaging data," Brain Stuct. Funct **218(2)**, 303–352 (2012).

[77] Richter, C. P. and Warner, C. L., "Comparision of weigert stained sections with unfixed, unstained sections for study of myelin sheaths," Proc. Nat. Acad. Sci. USA **71**, 598–601 (1974).

[78] Lin, C.-P., Wedeen, V. J., Chen, J.-H., Yao, C., and Tseng, W.-Y. I., "Validation of diffusion spectrum magnetic resonance imaging with manganese-enhanced rat optic tracts and ex vivo phantoms," NeuroImage **19**, 482–495 (2003).

[79] Richardson, S., Siow, B., Panagiotaki, E., Schneider, T., Lythgoe, M. F., and Alexander, D. C., "Viable and fixed white matter: Diffusion magnetic resonance ccomparison and contrasts at physiological temperature," Magnetic Resonance in Medicine **1**, 1–11 (2013).

[80] de Campos Vidal, B., Mello, M. L. S., Caseiro-Filho, A. C., and Godo, C., "Anisotropic properties of the myelin sheath," Acata histochem. **66**, 32–39 (1980).

[81] Born, M. and Wolf, E., [Principles of Optics - Electromagnetic Theory of Propagation, Interference and Diffraction of light], Cambridge University Press, 7th expanded ed. (2011).

[82] Wolecke, M., "Eine neue Method der Markscheidenfaerbung," Journal fuer Psychologie und Neurologie **51**, 199–204 (1942).

[83] Gallyas, F., "Silver staining of myelin by means of physical development," Neurological Research **1**(2), 203–209 (1979).

[84] Rieppo, J., Hallikainen, J., Jurvelin, J. S., Kiviranta, I., Helminen, H. J., and Hyttinen, M. M., "Practical considerations in the use of polarized light microscopy in the analysis of the collagen network in articular cartilage," Microscopy research and technique **71**, 279–287 (2008).

List of Symbols

6.1 Arabic letters

Variable	Explanation
a_k	Fourier coefficient associated with sine function
a'_k	new Fourier coefficient associated with sine function
A_k	amplitude of sinusoidal signal
b_k	Fourier coefficient associated with cosine function
b_k	new Fourier coefficient associated with cosine function
B	angle between the two filters of the PECF-sample
c_{xy}	correction factor for minimal partial volume effect
c_λ	factor to correct the wavelength discrepancy
d_{xy}	resolution limit in the x-y-plane (lateral resolution limit)
$d_{xy,\mathrm{LAP}}$	lateral resolution limit of the LAP
$d_{xy,\mathrm{PM}}$	lateral resolution limit of the PM
d_z	resolution limit in the z-plane (axial resolution limit)
$d_{z,\mathrm{LAP}}$	axial resolution limit of the LAP
$d_{z,\mathrm{PM}}$	measured axial resolution limit of the PM
$d'_{z,\mathrm{PM}}$	calculated axial resolution limit of the PM
$\mathrm{DR}_{\mathrm{LAP}}$	dynamic range of LAP
$\mathrm{DR}_{\mathrm{PM}}$	dynamic range of PM
$\vec{E}$	electric field vector
$\vec{E_T}$	transmitted electric field vector
$\vec{E_T}'$	transmitted electric field vector when considering the wavelength discrepancy
$\vec{E_0}$	electric field vector of unpolarized light
E_0	original electric field
E_x	x-component of the electric field vector
E_y	y-component of the electric field vector
f	spatial frequency
$f_c(\Gamma, \delta)$	function to correct wavelength discrepancy
f_{sc}	scaling factor for downsampling procedure

$\hat{I}$	mean intensity
I_0	incident light intensity
I_{0T}	transmitted light intensity including absorption
I_{ana}	intensity measured through analyzer
I_c	intensity measured through crossed linear polarizers
I_m	light intensity transmitted through *myelin*
$I_{\bar{m}}$	light intensity transmitted through *non-myelin*
I_{max}	maximal image intensity
I_{min}	minimal image intensity
I_N	normalized intensity ($I_N = I/I_0$)
I_{Nm}	normalized intensity for a voxel only containing *myelin*
$I_{N\bar{m}}$	normalized intensity for a voxel only containing *non-myelin*
I_p	intensity measured through parallel linear polarizers
I_{pol}	intensity measured through polarizer
I_{peak}	peak intensity
I_{ret}	intensity measured through retarder
I_T	transmitted/measured light intensity
I'_T	transmitted light intensity considering the wavelength discrepancy
ΔI	change of intensity
ΔI_{nc}	change of intensity for non-cooled LED panel
ΔI_{wc}	change of intensity for water-cooled LED panel
ΔI_{FWHM}	full width half maximum of intensity
Im	imaginary part
$\vec{J}$	Jones vector
k	magnitude of the wave vector
$\vec{M}$	magnetic field vector
M	lateral magnification
M_{fiber}	matrix representing the matrix that describes a fiber
M_{ret}	matrix of a wave retarder
N	number of measurements or photons
NA	numerical aperture of lens
n	refractive index (real part)
$n_e(\theta)$	extraordinary refractive index
n_o	ordinary refractive index
n_E	extraordinary refractive index for $\theta = 90°$
Δn	difference between ordinary and extraordinary refractive indices (birefringence)

Δn_m	difference between ordinary and extraordinary refractive indices for *myelin*
$\Delta n_{\bar{m}}$	difference between ordinary and extraordinary refractive indices for *non-myelin*
P_x	matrix of a linear horizontal polarizer
P_y	matrix of a linear vertical polarizer
r	retardation
$r_{\text{PM, max}}$	maximal retardation value determined with PM
$r_{\text{PM,peak}}$	peak retardation value determined with PM
$r_{\max}$	maximal retardation signal
$r_{\min}$	minimal retardation signal
r'	retardation value determined under consideration of the wavelength discrepancy
r'_c	retardation value corrected with c_λ
r'_{LAP}	retardation value determined with LAP under consideration of the wavelength discrepancy
r_{PM}	retardation value determine with PM
∂r	derivative of retardation
Δr	uncertainty of retardation value
$R(\psi)$	matrix describing a counter-clockwise rotation by an angle ψ
Re	real part
t	material thickness
$t_{\lambda/4}$	section thickness at which completly in-section fibers act as a quarter-wave retarder
t_m	thickness of *myelin*
$t_{\bar{m}}$	thickness of *non-myelin*
t_{rel}	relative section thickness
t_t	total section thickness
v	phase velocity

6.2 Greek letters

Variable	Explanation
α	out-of-section angle of nerve fiber = inclination angle
$\Delta\alpha$	difference of inclination angles or uncertainty of inclination angle
β	rotation angle ($\beta = \varphi - \rho$)
γ	phase shift along the fast axis of a wave retarder
Γ	retardance of an arbitrary retarder
Γ_1	retardance of fixed retarder (implemented in LAP)
Γ_1	retardance of non-fixed retarder (of PECF-sample)
δ	phase shift / retardation
$\partial\alpha$	derivative of inclination angle
ϵ_r	relative electric permittivity
$\tilde{\epsilon_r}$	relative permittivity tensor
$\tilde{\epsilon_r}'$	diagonal form of relative permittivity tensor
η_ρ	polarization efficiency
η_ρ(ana+pol)	polarization efficiency for analyzer and polarizer together
η_ρ(ana)	polarization efficiency for analyzer
η_ρ(pol)	polarization efficiency for polarizer together
θ	angle of incidence defined as the angle between the wave vector $\vec{k}$ and the optic axis of the medium
λ	wavelength of the light
$\lambda_{\text{LAP,ill}}$	wavelength of LAP illumination
$\lambda_{\text{LAP,ill, nc}}$	wavelength of LAP non-cooled illumination
$\lambda_{\text{LAP,ill, wc}}$	wavelength of LAP water-cooled illumination
$\lambda_{\text{LAP,ret}}$	specified wavelength of the LAP retarder at which the light is retarded a quarter wavelength
$\lambda_{\text{PM,ill}}$	wavelength of PM illumination
$\lambda_{\text{PM,ret}}$	specified wavelength of the PM retarder at which the light is retarded a quarter wavelength
$\Delta\lambda_{\text{LAP}}$	wavelength discrepancy between $\lambda_{\text{LAP,ill}}$ and $\lambda_{\text{LAP,ret}}$
μ	light attenuation coefficient
μ_m	light attenuation coefficient of *myelin*
$\mu_{\bar{m}}$	light attenuation coefficient of *non-myelin*
μ_r	relative permeability
μ_{sig}	averaged signal value
μ_t	light attenuation coefficient for complete tissue

ρ	rotation angle of filters
ρ_{cam}	rotation angle of the camera
ρ_{sample}	angle around which the sample is rotated
σ	image noise
σ_{LAP}	signal to noise ratio of the LAP
σ_{PM}	signal to noise ratio of the PM
$\sigma_{I,\text{LAP}}$	error of transmittance signal measured with the LAP
$\sigma_{I,\text{PM}}$	error of transmittance signal measured with the PM
σ_{φ}	error of direction angle
$\sigma_{\varphi,\text{fixed}}$	error of direction angle for fixed tissue sample measured with the LAP
$\sigma_{\varphi,\text{moved}}$	error of direction angle for moved tissue sample measured with the LAP
$\sigma_{\varphi,PM}$	error of direction angle measured with the PM
$\sigma_{r,\text{fixed}}$	error of retardation for fixed tissue sample measured with the LAP
$\sigma_{r,\text{moved}}$	error of retardation for moved tissue sample measured with the LAP
$\sigma_{r,PM}$	error of retardation value measured with the PM
σ_{sig}	standard deviation of signal
τ	time
ϕ	phase of sinusoidal signal
ϕ_1	phase of sinusoidal signal
φ	in-section angle of nerve fiber = direction angle
$\Delta\varphi$	uncertainty of direction angle
$\Delta\phi$	phase shift
ψ	rotation angle
ω	angular frequency

6.3 List of Abbreviations

Abbreviation	Explanation
3D-PLI	three dimensional polarized light imaging
BRAIN	brain research through advancing innovative neurotechnologies
CAB	cellulose acetobutyrate
CC	corpus callosum
CCD	charge-coupled device
cg	cingulum
CLSM	confocal laser scanning microscopy
dMRI	diffusion magnetic resonance imaging
DMSO	dimethyl sulfoxide
DR	dynamic range
FOM	fiber orientation map
FWHM	full width half maximum
GM	gray matter
LAP	large-area polarimeter
LED	light emitting diode
MI	Michelson contrast
MTF	modulation transfer function
MOST	micro-optical sectioning tomography
MR	magnetic resonance
MRI	magnetic resonance imaging
NIH	national institute of health
OECF	opto electronic conversion function
PECF	polarization electronic conversion function
PER	polarization extinction ratio
PM	polarizing microscope
pt	putamen
RGB-FOM	fiber orientation map using the RGB color space
ROI	region of interest
SNR	signal-to-noise ratio
WM	white matter

Appendix

A.1 Jones matrix formalism of the polarizing microscope

The second employed polarimetric system (referred to as "polarizing microscope") consists of a pair of linear polarizers ($\mathrm{P}(\rho)$ and P_y) and a quarter-wave retarder ($\mathrm{M}_{\mathrm{ret}}(\pi/2)$). In this setup, only the first linear polarizer (analyzer) is rotatable while the orientation of the quarter-wave retarder and the second linear polarizer are fixed (cp. Fig. 1). Thus, the mathematical description of the orientation of the quarter-wave retarder is with regards to the fixed second linear polarizer. The quarter-wave retarder is installed with its fast axis under an angle of $\psi = -45\,^\circ$ oriented with respect to the x-axis of the first linear polarizer (see Fig. 1):

$$M'_{\mathrm{ret}}(\delta = \pi/2, \psi = -\pi/4) \overset{(2.8),(2.9)}{=} \frac{1}{\sqrt{2}} \begin{pmatrix} 1 & -\mathrm{i} \\ -\mathrm{i} & 1 \end{pmatrix}.$$

Compared to the large-area polarimeter, the order of the polarizing filters in the polarizing microscope differs slightly. As depicted in Figure 3.1 B, the positions of the quarter-wave retarder and the object stage are switched in the PM as compared to the LAP. These modifications are reflected in the theoretical description with the Jones matrix formalism.
As previously explained in Section 2.4.3, the influence of the brain tissue can be described as a wave retarder [44]. As the fast axis is defined to be in

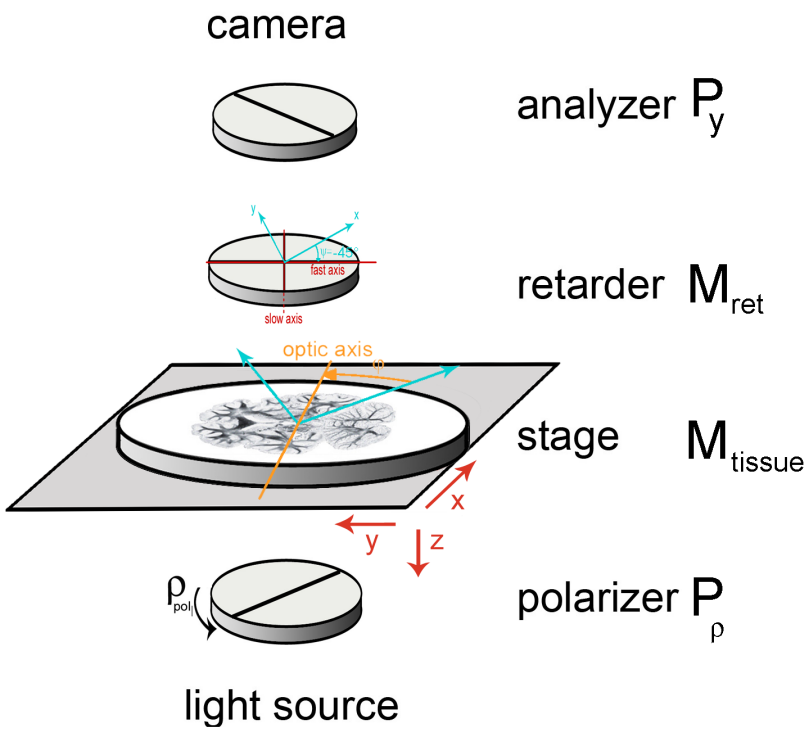

Figure 1: Polarimetric setup of the PM. The rotatable polarizer (P_ρ) enables the illumination of the tissue (M_{tissue}) with linearly polarized light whose orientation changes depending on the rotation angle ρ of the filter. The fast axis of the quarter-wave retarder (M_{ret}) is oriented at $\psi = -45\,^\circ$ with respect to the x-axis of the first linear polarizer. The induced change of the polarization state by the brain tissue is analyzed by the fixed quarter-wave retarder and the fixed analyzer (P_y). The brain tissue is described as an uniaxial birefringent medium with a single optic axis with in-plane direction angle φ.

direction of the optic axis of the fiber, the tissue can be described by:

$$M_{\text{fiber}}(\delta,\varphi) \overset{2.8,2.9}{=} R(\varphi)\cdot M_{\text{ret}}(\delta)\cdot R(-\varphi)$$
$$= \begin{pmatrix} \cos\left(\frac{\delta}{2}\right)+\mathrm{i}\sin\left(\frac{\delta}{2}\right)\cdot\cos(2\varphi) & \mathrm{i}\sin\left(\frac{\delta}{2}\right)\cdot\sin(2\varphi) \\ \mathrm{i}\sin\left(\frac{\delta}{2}\right)\cdot\sin(2\varphi) & \cos\left(\frac{\delta}{2}\right)-\mathrm{i}\sin\left(\frac{\delta}{2}\right)\cdot\cos(2\varphi) \end{pmatrix} \quad (1)$$

The light emitted by the employed light source is unpolarized and therefore cannot be described by the Jones matrix formalism. Thus, the electric field vector of the linearly polarized light after the first linear polarizer will be used as incident light:

$$\vec{E}(\rho) = E_{0T}\begin{pmatrix}\cos(\rho)\\ \sin(\rho)\end{pmatrix}, \quad (2)$$

where ρ describes the rotation angle of the first linear polarizer. Thus, using the Jones matrix formalism, the mathematical description of the measurements performed with the "polarizing microscope" is as follows:

$$\begin{aligned}
&\vec{E_T}(PM) = P_y\cdot M'_{\text{ret}}\left(\frac{\pi}{2}\right)\cdot M_{\text{fiber}}(\delta,\varphi)\cdot\vec{E}(\rho)\\
&=\begin{pmatrix}0&0\\0&1\end{pmatrix}\cdot\frac{1}{\sqrt{2}}\begin{pmatrix}1&-\mathrm{i}\\-\mathrm{i}&1\end{pmatrix}\cdot M_{\text{fiber}}(\delta,\varphi)\cdot\begin{pmatrix}E_{0T}\cos(\rho)\\E_{0T}\sin(\rho)\end{pmatrix}\\
&=\frac{E_{0T}}{\sqrt{2}}\begin{pmatrix}0&0\\-\mathrm{i}&1\end{pmatrix}\begin{pmatrix}\cos\left(\frac{\delta}{2}\right)+\mathrm{i}\sin\left(\frac{\delta}{2}\right)\cos(2\varphi) & \mathrm{i}\sin\left(\frac{\delta}{2}\right)\sin(2\varphi)\\ \mathrm{i}\sin\left(\frac{\delta}{2}\right)\sin(2\varphi) & \cos\left(\frac{\delta}{2}\right)-\mathrm{i}\sin\left(\frac{\delta}{2}\right)\cos(2\varphi)\end{pmatrix}\begin{pmatrix}\cos(\rho)\\\sin(\rho)\end{pmatrix}\\
&=\frac{E_{0T}}{\sqrt{2}}\Big[-\mathrm{i}\cos\left(\frac{\delta}{2}\right)\cos(\rho)+\sin\left(\frac{\delta}{2}\right)\cos(2\varphi)\cos(\rho)+\mathrm{i}\sin\left(\frac{\delta}{2}\right)\sin(2\varphi)\cos(\rho)\\
&\quad+\sin\left(\frac{\delta}{2}\right)\sin(2\varphi)\sin(\rho)+\cos\left(\frac{\delta}{2}\right)\sin(\rho)-\mathrm{i}\sin\left(\frac{\delta}{2}\right)\cos(2\varphi)\sin(\rho)\Big]\vec{e_y},
\end{aligned} \quad (3)$$

where $\vec{E_T}$ represents the electrical field vector of the transmitted light, P_y describes the second linear polarizer, $M'_{\text{ret}}\left(\frac{\pi}{2}\right)$ is the matrix describing the quarter-wave retarder, and $M_{\text{fiber}}(\delta,\varphi)$ represents the matrix of the brain tissue.

As the light intensity is proportional to the absolute square of the electric

field components, Equation (3) can be modified to:

$$
\begin{aligned}
I \sim & |\vec{E_T}(PM)|^2 \\
= & \frac{E_{0T}^2}{2}\Bigg[\cos^2\left(\frac{\delta}{2}\right)\cos^2(\rho) + \sin^2\left(\frac{\delta}{2}\right)\sin^2(2\varphi)\cos^2(\rho) \\
& + \sin^2\left(\frac{\delta}{2}\right)\cos^2(2\varphi)\sin^2(\rho) - 2\cos\left(\frac{\delta}{2}\right)\sin\left(\frac{\delta}{2}\right)\sin(2\varphi)\cos^2(\rho) \\
& + 2\cos\left(\frac{\delta}{2}\right)\sin\left(\frac{\delta}{2}\right)\cos(2\varphi)\cos(\rho)\sin(\rho) - 2\sin^2\left(\frac{\delta}{2}\right)\sin(2\varphi)\cos(2\varphi)\sin(\rho)\cos(\rho) \\
& + \sin^2\left(\frac{\delta}{2}\right)\cos^2(2\varphi)\cos^2(\rho) + \sin^2\left(\frac{\delta}{2}\right)\sin^2(2\varphi)\sin^2(\rho) + \cos^2\left(\frac{\delta}{2}\right)\sin^2(\rho) \\
& + 2\sin^2\left(\frac{\delta}{2}\right)\sin(2\varphi)\cos(2\varphi)\cos(\rho)\sin(\rho) + 2\sin\left(\frac{\delta}{2}\right)\cos\left(\frac{\delta}{2}\right)\cos(2\varphi)\cos(\rho)\sin(\rho) \\
& + 2\sin\left(\frac{\delta}{2}\right)\cos\left(\frac{\delta}{2}\right)\sin(2\varphi)\sin^2(\rho)\Bigg] \\
\\
= & \frac{E_{0T}^2}{2}\Bigg[\cos^2\left(\frac{\delta}{2}\right) + \sin^2\left(\frac{\delta}{2}\right)\sin^2(2\varphi) + \sin^2\left(\frac{\delta}{2}\right)\cos^2(2\varphi) - 2\cos\left(\frac{\delta}{2}\right)\sin\left(\frac{\delta}{2}\right) \\
& \cdot \sin(2\varphi)(\cos^2(\rho) - \sin^2(\rho)) + 4\cos\left(\frac{\delta}{2}\right)\sin\left(\frac{\delta}{2}\right)\cos(2\varphi)\cos(\rho)\sin(\rho)\Bigg] \\
= & \frac{E_{0T}^2}{2}\Bigg[\cos^2\left(\frac{\delta}{2}\right) + \sin^2\left(\frac{\delta}{2}\right) - \sin(\delta)\sin(2\varphi)\cos(2\rho) + \sin(\delta)\cos(2\varphi)\sin(2\rho)\Bigg] \\
= & \frac{E_{0T}^2}{2}\big[1 - \sin(\delta)\sin(2\varphi - 2\rho)\big] \\
= & \frac{E_{0T}^2}{2}\big[1 + \sin(\delta)\sin(2\rho - 2\varphi)\big] \\
\sim & \frac{I_{0T}^2}{2}\big[1 + \sin(\delta)\sin(2\rho - 2\varphi)\big]. \qquad (4)
\end{aligned}
$$

The derived formula is nearly identical to Equation (2.14) that describes the large-area polarimeter.

A.2 Theoretical description of the PECF measurement

The sample for the PECF-measurement is a combination of a retarder and a linear polarizer (cp. Sec. 3.4). The angle B between the two filters can be varied arbitrarily. For this measurement in the LAP, the first linear polarizer P_x and the quarter-wave retarder $M_{\text{ret}}(\Gamma_1, \psi = -45\,^\circ)$ stayed fixed and were not rotated. The fast axis of the quarter-wave retarder was oriented under an angle of $-45\,^\circ$ with respect to the transmission axis of the first linear polarizer. As previously stated in Section 2.4.3, the Jones vector $\vec{E_x}$ will be used to describe the polarized light after the first linear polarizer ($\vec{E_x} = P_x \cdot E_{\text{unpol}}$). In this experiment, only the second linear polarizer was rotated by the angle ρ. The performed measurement can be described by the Jones matrix formalism as follows:

$$\vec{E_T'}(\text{PECF}_{\text{LAP}}) = P_\rho \cdot \underbrace{M'_{\text{ret}}(\Gamma_2, B) \cdot P_y}_{\text{sample}} \cdot M'_{\text{ret}}(\Gamma_1) \cdot \vec{E_x}.$$

The employed sample for the PECF-measurement can be described by:

$$\begin{aligned} M'_{\text{ret}}(\Gamma_2, B) \cdot P_y =& R(B) \cdot M_{\text{ret}}(\Gamma_2) \cdot R(-B) \cdot P_y \\ =& \begin{pmatrix} \cos(\Gamma_2) + \mathrm{i}\sin(\Gamma_2)\cos(2B) & \mathrm{i}\sin(2B)\sin(\Gamma_2) \\ \mathrm{i}\sin(2B)\sin(\Gamma_2) & \cos(\Gamma_2) - \mathrm{i}\sin(\Gamma_2)\cos(2B) \end{pmatrix} \cdot \begin{pmatrix} 0 & 0 \\ 0 & 1 \end{pmatrix} \\ =& \begin{pmatrix} 0 & \mathrm{i}\sin(2B)\sin(\Gamma_2) \\ 0 & \cos(\Gamma_2) - \mathrm{i}\sin(\Gamma_2)\cos(2B) \end{pmatrix}, \end{aligned}$$

where $2\Gamma_2 = \delta_2$ describes the retardance induced by the foil retarder which is part of the PECF-sample. The rotatable linear polarizer is given by:

$$\begin{aligned} P_\rho =& R(\rho) \cdot P_y \cdot R(-\rho) \\ =& \begin{pmatrix} \cos(\rho) & -\sin(\rho) \\ \sin(\rho) & \cos(\rho) \end{pmatrix} \cdot \begin{pmatrix} 1 & 0 \\ 0 & 0 \end{pmatrix} \cdot \begin{pmatrix} \cos(-\rho) & -\sin(-\rho) \\ \sin(-\rho) & \cos(-\rho) \end{pmatrix} \\ =& \begin{pmatrix} \cos^2(\rho) & \cos(\rho)\sin(\rho) \\ \cos(\rho)\sin(\rho) & \sin^2(\rho) \end{pmatrix} \\ =& \begin{pmatrix} \cos^2(\rho) & \frac{1}{2}\sin(2\rho) \\ \frac{1}{2}\sin(2\rho) & \sin^2(\rho) \end{pmatrix}. \end{aligned}$$

The implemented retarder, which is oriented at an angle of $-45\,^\circ$ with respect to the first linear polarizer, is given by:

$$\begin{aligned} M'_{\mathrm{ret}}(\Gamma_1) =& R(-45\,^\circ)\cdot M_{\mathrm{ret}}(\Gamma_1)\cdot R(45\,^\circ) \\ =& \begin{pmatrix} \cos(\Gamma_1)+\mathrm{i}\sin(\Gamma_1)\cos(-90\,^\circ) & \mathrm{i}\sin(-90\,^\circ)\sin(\Gamma_1) \\ \mathrm{i}\sin(-90\,^\circ)\sin(\Gamma_1) & \cos(\Gamma_1)-\mathrm{i}\sin(\Gamma_1)\cos(-90\,^\circ) \end{pmatrix} \\ =& \begin{pmatrix} \cos(\Gamma_1) & -\mathrm{i}\sin(\Gamma_1) \\ -\mathrm{i}\sin(\Gamma_1) & \cos(\Gamma_1) \end{pmatrix}, \end{aligned}$$

where $2\Gamma_1 = \delta_1$ describes the retardance of the retarder implemented into the polarimetric setup.

$$\begin{aligned} \vec{E'_T}(\mathrm{PECF_{LAP}}) &= P_\rho \cdot \underbrace{M_{\mathrm{ret}}(\Gamma_2, B)\cdot P_y}_{\text{sample}} \cdot M'_{\mathrm{ret}}(\Gamma_1)\cdot \vec{E_x} \\ &= \begin{pmatrix} \cos^2(\rho) & \frac{1}{2}\sin(2\rho) \\ \frac{1}{2}\sin(2\rho) & \sin^2(\rho) \end{pmatrix} \cdot \begin{pmatrix} 0 & \mathrm{i}\sin(2B)\sin(\Gamma_2) \\ 0 & \cos(\Gamma_2)-\mathrm{i}\sin(\Gamma_2)\cos(2B) \end{pmatrix} \cdot M'_{\mathrm{ret}}(\Gamma_1)\cdot \vec{E_x} \\ &= \begin{pmatrix} 0 & \mathrm{i}\cos^2(\rho)\sin(2B)\sin(\Gamma_2)+\frac{1}{2}\sin(2\rho)\cos(\Gamma_2)-\frac{\mathrm{i}}{2}\sin(2\rho)\sin(\Gamma_2)\cos(2B) \\ 0 & \frac{\mathrm{i}}{2}\sin(2\rho)\sin(2B)\sin(\Gamma_2)+\sin^2(\rho)\cos(\Gamma_2)-\mathrm{i}\sin^2(\rho)\sin(\Gamma_2)\cos(2B) \end{pmatrix} \\ &\quad \cdot \begin{pmatrix} \cos(\Gamma_1) & -\mathrm{i}\sin(\Gamma_1) \\ -\mathrm{i}\sin(\Gamma_1) & \cos(\Gamma_1) \end{pmatrix} \cdot \begin{pmatrix} E_{0x} \\ 0 \end{pmatrix} \\ &= -\mathrm{i}\sin(\Gamma_1)E_{0x}\Big[\mathrm{i}\cos^2(\rho)\sin(2B)\sin(\Gamma_2)+\frac{1}{2}\sin(2\rho)\cos(\Gamma_2) \\ &\quad -\frac{\mathrm{i}}{2}\sin(2\rho)\sin(\Gamma_2)\cos(2B)\Big]\vec{e_x} - \mathrm{i}\sin(\Gamma_1)E_{0x}\Big[\frac{\mathrm{i}}{2}\sin(2\rho)\sin(2B)\sin(\Gamma_2) \\ &\quad +\sin^2(\rho)\cos(\Gamma_2)-\mathrm{i}\sin^2(\rho)\sin(\Gamma_2)\cos(2B)\Big]\vec{e_y} \end{aligned}$$

$$
\begin{aligned}
&= \sin(\Gamma_1) E_{0x} \Bigg[\vec{e_x} \Bigg(-\mathrm{i} \underbrace{\left(\frac{1}{2} \sin(2\rho) \cos(\Gamma_2) \right)}_{\mathrm{Im}_1} \\
&\quad + \underbrace{\cos^2(\rho) \sin(2B) \sin(\Gamma_2) - \frac{1}{2} \sin(2\rho) \sin(\Gamma_2) \cos(2B)}_{\mathrm{Re}_1} \Bigg) \\
&\quad + \vec{e_y} \Bigg(\underbrace{\frac{1}{2} \sin(2\rho) \sin(2B) \sin(\Gamma_2) - \sin^2(\rho) \sin(\Gamma_2) \cos(2B)}_{\mathrm{Re}_2} \\
&\quad - \mathrm{i} \underbrace{\sin^2(\rho) \cos(\Gamma_2)}_{\mathrm{Im}_2} \Bigg) \Bigg]. \qquad (5)
\end{aligned}
$$

As the light intensity is proportional to the absolute square of the electric field components, Equation (5) can be solved to:

$$
\begin{aligned}
&I_{T,\mathrm{PECF}}(\mathrm{PECF_{LAP}}) = |\vec{E_T'}(\mathrm{PECF_{LAP}})|^2 \\
&\quad = \mathrm{Re}_1^2(\vec{E_T'}(\mathrm{PECF_{LAP}})) + \mathrm{Im}_1^2(\vec{E_T'}(\mathrm{PECF_{LAP}})) \\
&\qquad + \mathrm{Re}_2^2(\vec{E_T'}(\mathrm{PECF_{LAP}})) + \mathrm{Im}_1^2(\vec{E_T'}(\mathrm{PECF_{LAP}})) \\
&\quad = \sin^2(\Gamma_1) E_{0x}^2 \Big[\cos^4(\rho) \sin^2(2B) \sin^2(\Gamma_2) + \frac{1}{4} \sin^2(2\rho) \sin^2(\Gamma_2) \cos^2(2B) \\
&\qquad - \cos^2(\rho) \sin(2\rho) \sin(2B) \cos(2B) \sin^2(\Gamma_2) + \frac{1}{4} \sin^2(2\rho) \cos^2(\Gamma_2) \\
&\qquad + \frac{1}{4} \sin^2(2\rho) \sin^2(2B) \sin^2(\Gamma_2) + \sin^4(\rho) \sin^2(\Gamma_2) \cos^2(2B) \\
&\qquad - \sin(2\rho) \sin^2(\rho) \sin(2B) \cos(2B) \sin^2(\Gamma_2) + \sin^4(\rho) \cos^2(\Gamma_2) \Big] \\
&\quad = \sin^2(\Gamma_1) E_{0x}^2 \Big[-\frac{1}{2} \sin(2\rho) \sin(4B) \sin^2(\Gamma_2) + \frac{1}{4} \sin^2(2\rho) \sin^2(\Gamma_2) \\
&\qquad + \cos^4(\rho) \sin^2(2B) \sin^2(\Gamma_2) + \frac{1}{4} \sin^2(2\rho) \cos^2(\Gamma_2) + \sin^4(\rho) \sin^2(\Gamma_2) \\
&\qquad \cdot \cos^2(2B) + \sin^4(\rho) \cos^2(\Gamma_2) \Big] \\
&\quad = \sin^2(\Gamma_1) E_{0x}^2 \Big[\sin^2(\Gamma_2) \Big(-\frac{1}{2} \sin(2\rho) \sin(4B) + \cos^4(\rho) \sin^2(2B) \\
&\qquad + \sin^4(\rho) \cos^2(2B) \Big) + \sin^4(\rho) \cos^2(\Gamma_2) + \frac{1}{4} \sin^2(2\rho) \Big] \qquad (6)
\end{aligned}
$$

The derived equation describes the intensity change depending on the retardances Γ_1 and Γ_2 of the two implemented retarders, the rotation angle ρ of the linear polarizer, and the angle B between the retarder and the linear polarizer that constitute the PECF-sample.

A.3 Jones matrix formalism of the LAP setup considering the wavelength discrepancy

A retarder with an arbitrary retardance (Γ) that is oriented $\psi = -45\,^\circ$ with respect to the axis of the first linear polarizer is described by:

$$
\begin{aligned}
M'_{\mathrm{ret}}(\Gamma, \psi = -\pi/4) &\overset{2.8,2.9}{=} R(-\pi/4) \cdot M_{\mathrm{ret}}(\pi/2) \cdot R(\pi/4) \\
&= \begin{pmatrix} \cos(-\pi/4) & -\sin(-\pi/4) \\ \sin(-\pi/4) & \cos(-\pi/4) \end{pmatrix} \cdot \begin{pmatrix} e^{\mathrm{i}\Gamma} & 0 \\ 0 & e^{-\mathrm{i}\Gamma} \end{pmatrix} \cdot \begin{pmatrix} \cos(-\pi/4) & \sin(-\pi/4) \\ -\sin(-\pi/4) & \cos(-\pi/4) \end{pmatrix} \\
&= \begin{pmatrix} \cos(\Gamma) & -\mathrm{i}\sin(\Gamma) \\ -\mathrm{i}\sin(\Gamma) & \cos(\Gamma) \end{pmatrix}. \qquad (7)
\end{aligned}
$$

Replacing the matrix for the quarter-wave retarder with a retarder that induces an arbitrary phase shift of Γ in Equation (2.13) results in:

$$
\begin{aligned}
\vec{E_T}' &= P_y \cdot M_{\mathrm{fiber}}(\delta, \beta) \cdot M'_{\mathrm{ret}}(\Gamma) \cdot \vec{E_x} \\
&= \begin{pmatrix} 0 & 0 \\ 0 & 1 \end{pmatrix} \cdot \begin{pmatrix} \cos\left(\frac{\delta}{2}\right) + \mathrm{i}\sin\left(\frac{\delta}{2}\right)\cos(2\beta) & \mathrm{i}\sin\left(\frac{\delta}{2}\right)\sin(2\beta) \\ \mathrm{i}\sin\left(\frac{\delta}{2}\right)\sin(2\beta) & \cos\left(\frac{\delta}{2}\right) - \mathrm{i}\sin\left(\frac{\delta}{2}\right)\cos(2\beta) \end{pmatrix} \\
&\quad \cdot \begin{pmatrix} \cos(\Gamma) & -\mathrm{i}\sin(\Gamma) \\ -\mathrm{i}\sin(\Gamma) & \cos(\Gamma) \end{pmatrix} \cdot \begin{pmatrix} E_x \\ 0 \end{pmatrix} \\
&= \begin{pmatrix} 0 & 0 \\ \underbrace{\mathrm{i}\sin\left(\frac{\delta}{2}\right)\sin(2\beta)}_{A} & \underbrace{\cos\left(\frac{\delta}{2}\right) - \mathrm{i}\sin\left(\frac{\delta}{2}\right)\cos(2\beta)}_{B} \end{pmatrix} \cdot \begin{pmatrix} \cos(\Gamma) & -\mathrm{i}\sin(\Gamma) \\ -\mathrm{i}\sin(\Gamma) & \cos(\Gamma) \end{pmatrix} \cdot \begin{pmatrix} E_x \\ 0 \end{pmatrix} \\
&= \begin{pmatrix} 0 & 0 \\ \cos(\Gamma) \cdot A - \mathrm{i}\sin(\Gamma) \cdot B & -\mathrm{i}\sin(\Gamma) \cdot A + \cos(\Gamma) \cdot B \end{pmatrix} \cdot \begin{pmatrix} E_x \\ 0 \end{pmatrix} \\
&= \Bigg[\mathrm{i}\cos(\Gamma)\sin\left(\frac{\delta}{2}\right)\sin(2\beta) - \mathrm{i}\sin(\Gamma)\cos\left(\frac{\delta}{2}\right) - \sin(\Gamma)\sin\left(\frac{\delta}{2}\right) \\
&\quad \cdot \cos(2\beta) \Bigg] E_x \vec{e}_y \\
&= \Bigg[\mathrm{i} \underbrace{\left(\cos(\Gamma)\sin\left(\frac{\delta}{2}\right)\sin(2\beta) - \sin(\Gamma)\cos\left(\frac{\delta}{2}\right) \right)}_{\mathrm{Im}} \\
&\quad \underbrace{- \sin(\Gamma)\sin\left(\frac{\delta}{2}\right)\cos(2\beta)}_{\mathrm{Re}} \Bigg] E_x \vec{e}_y. \qquad (8)
\end{aligned}
$$

The measured light intensity corresponds to the absolute square of the electric field vector ($I'_T \sim |\vec{E}'_T|^2$):

$$
\begin{aligned}
I'_T \sim & |\vec{E_T}'|^2 = \mathrm{Re}^2\left(\vec{E_T}'\right) + \mathrm{Im}^2\left(\vec{E_T}'\right) \\
& \Bigg(\cos^2(\Gamma)\sin^2\left(\frac{\delta}{2}\right)\sin^2(2\beta) + \sin^2(\Gamma)\cos^2\left(\frac{\delta}{2}\right) - 2\cos(\Gamma) \\
& \cdot \sin(\Gamma)\cos\left(\frac{\delta}{2}\right)\sin\left(\frac{\delta}{2}\right)\sin(2\beta) + \sin^2(\Gamma)\sin^2\left(\frac{\delta}{2}\right) \\
& \cdot \underbrace{\cos^2(2\beta)}_{=\sin^2(2\beta)+\cos(4\beta)} \Bigg) I'_{0T} \\
= & \Bigg[\cos^2(\Gamma)\sin^2\left(\frac{\delta}{2}\right)\sin^2(2\beta) + \sin^2(\Gamma)\cos^2\left(\frac{\delta}{2}\right) - \frac{1}{2}\sin(2\Gamma)\sin(\delta) \\
& \cdot \sin(2\beta) + \sin^2(\Gamma)\sin^2\left(\frac{\delta}{2}\right)\sin^2(2\beta) - \sin^2(\Gamma)\sin^2\left(\frac{\delta}{2}\right)\cos(4\beta)\Bigg] I_{0T} \\
= & \Bigg[\sin^2\left(\frac{\delta}{2}\right) \underbrace{\sin^2(2\beta)}_{=\frac{1}{2}(1-\cos(4\beta))} \underbrace{(\cos^2(\Gamma)+\sin^2(\Gamma))}_{=1} + \sin^2(\Gamma)\cos^2\left(\frac{\delta}{2}\right) \\
& - \frac{1}{2}\sin(2\Gamma)\sin(\delta)\sin(2\beta) + \sin^2(\Gamma)\sin^2\left(\frac{\delta}{2}\right)\cos(4\beta)\Bigg] I'_{0T} \\
= & \Bigg[\frac{1}{2}\sin^2\left(\frac{\delta}{2}\right)(1-\cos(4\beta)) + \sin^2(\Gamma)\cos^2\left(\frac{\delta}{2}\right) - \frac{1}{2}\sin(2\Gamma) \\
& \cdot \sin(\delta)\sin(2\beta) + \sin^2(\Gamma)\sin^2\left(\frac{\delta}{2}\right)\cos(4\beta)\Bigg] I'_{0T} \\
= & \Bigg[\frac{1}{2}\sin^2\left(\frac{\delta}{2}\right) - \frac{1}{2}\sin^2\left(\frac{\delta}{2}\right)\cos(4\beta) + \sin^2(\Gamma)\cos^2\left(\frac{\delta}{2}\right) \\
& - \frac{1}{2}\sin(2\Gamma)\sin(\delta)\sin(2\beta) + \sin^2(\Gamma)\sin^2\left(\frac{\delta}{2}\right)\cos(4\beta)\Bigg]' I_{0T} \qquad (9)
\end{aligned}
$$

with $\beta = \varphi - \rho$ being the difference between the rotation angle (ρ) and the in-plane direction of the nerve fibers (φ), Equation (9) results in:

$$
\begin{aligned}
I'_T = &\Bigg[\frac{1}{2}\sin^2\left(\frac{\delta}{2}\right) + \sin^2(\Gamma)\cos^2\left(\frac{\delta}{2}\right) - \frac{1}{2}\sin(2\Gamma)\sin(\delta) \\
&\cdot \left(\sin(2\varphi)\cos(2\rho) - \sin(2\rho)\cos(2\varphi)\right) \\
&- \frac{1}{2}\sin^2\left(\frac{\delta}{2}\right)\left(\cos(4\varphi)\cos(4\rho) + \sin(4\varphi)\sin(4\rho)\right) \\
&+ \sin^2(\Gamma)\sin^2\left(\frac{\delta}{2}\right)\left(\cos(4\varphi)\cos(4\rho) + \sin(4\varphi)\sin(4\rho)\right)\Bigg] I'_{0T} \\
= &\Bigg[\frac{1}{2}\sin^2\left(\frac{\delta}{2}\right) + \sin^2(\Gamma)\cos^2\left(\frac{\delta}{2}\right) \\
&- \frac{1}{2}\sin(2\Gamma)\sin(\delta)\sin(2\varphi)\cos(2\rho) \\
&+ \frac{1}{2}\sin(2\Gamma)\sin(\delta)\sin(2\rho)\cos(2\varphi) \\
&- \frac{1}{2}\sin^2\left(\frac{\delta}{2}\right)\cos(4\varphi)\cos(4\rho) \\
&- \frac{1}{2}\sin^2\left(\frac{\delta}{2}\right)\sin(4\varphi)\sin(4\rho) \\
&+ \sin^2(\Gamma)\sin^2\left(\frac{\delta}{2}\right)\cos(4\varphi)\cos(4\rho) \\
&+ \sin^2(\Gamma)\sin^2\left(\frac{\delta}{2}\right)\sin(4\varphi)\sin(4\rho)\Bigg] I'_{0T} \\
= &\Bigg[\frac{1}{2}\sin^2\left(\frac{\delta}{2}\right) + \sin^2(\Gamma)\cos^2\left(\frac{\delta}{2}\right) \\
&- \frac{1}{2}\sin(2\Gamma)\sin(\delta)\sin(2\varphi)\cos(2\rho) \\
&+ \frac{1}{2}\sin(2\Gamma)\sin(\delta)\sin(2\rho)\cos(2\varphi) \\
&- \frac{1}{2}\sin^2\left(\frac{\delta}{2}\right)\cos(4\varphi)\cos(4\rho)(1 - 2\sin^2(\Gamma)) \\
&- \frac{1}{2}\sin^2\left(\frac{\delta}{2}\right)\sin(4\varphi)\sin(4\rho)(1 - 2\sin^2(\Gamma))\Bigg] I'_{0T}
\end{aligned}
$$

$$
\begin{aligned}
=\Bigg[&\frac{1}{2}\sin^2\left(\frac{\delta}{2}\right)+\sin^2(\Gamma)\cos^2\left(\frac{\delta}{2}\right)\\
&+\frac{1}{2}\sin(2\Gamma)\sin(\delta)\sin(2\rho)\cos(2\varphi)\\
&-\frac{1}{2}\sin(2\Gamma)\sin(\delta)\sin(2\varphi)\cos(2\rho)\\
&-\frac{1}{2}\sin^2\left(\frac{\delta}{2}\right)\sin(4\varphi)\sin(4\rho)\cos(2\Gamma)\\
&-\frac{1}{2}\sin^2\left(\frac{\delta}{2}\right)\cos(4\varphi)\cos(4\rho)\cos(2\Gamma)\Bigg]I'_{0T}
\end{aligned}
\tag{10}
$$

A.4 Superposition of two sinusoidal waves

The investigated sinusoidal waves have the same frequency, but they differ in terms of amplitudes and phases:

$$\begin{aligned} f_1(t) &= A_1 \sin(\omega t), \\ f_2(t) &= A_2 \sin(\omega t + \phi_1). \end{aligned}$$

The superposition of these two sinusoidal waves can be described according to:

$$\begin{aligned} f_1(t) + f_2(t) =& A_1 \sin(\omega t) + A_2 \sin(\omega t + \phi_1) \\ =& A_1 \sin(\omega t) + A_2(\sin(\omega t)\cos(\phi_1) + \sin(\phi_1)\cos(\omega t)) \\ =& A_1 \sin(\omega t) + A_2 \sin(\omega t)\cos(\phi_1) + A_2 \sin(\phi_1)\cos(\omega t) \\ =& \sin(\omega t)(A_1 + A_2\cos(\phi_1)) + A_2 \sin(\phi_1)\cos(\omega t) \end{aligned} \tag{11}$$

If A is the amplitude of the resulting wave and ϕ is the phase angle, then:

$$\begin{aligned} f_1(t) + f_2(t) =& A \sin(\omega t + \phi) \\ =& A \sin(\omega t)\cos(\phi) + A \sin(\phi)\cos(\omega t). \end{aligned} \tag{12}$$

The comparison of Equations (11) and (12) yields:

$$\begin{aligned} A \sin(\omega t)\cos(\phi) =& (A_1 + A_2\cos(\phi_1))\sin(\omega t) \\ \Rightarrow A\cos(\phi) =& A_1 + A_2\cos(\phi_1) \end{aligned} \tag{13}$$

and

$$\begin{aligned} A \sin(\phi)\cos(\omega t) =& A_2 \sin(\phi_1)\cos(\omega t) \\ \Rightarrow A\sin(\phi) =& A_2 \sin(\phi_1). \end{aligned} \tag{14}$$

Equation (14) can be converted to:

$$A = \frac{A_2 \sin(\phi_1)}{\sin(\phi)}. \tag{15}$$

By inserting the resulting amplitude A into Equation (13), the resulting phase shift ϕ can be determined:

$$\begin{aligned}\frac{A_2 \sin(\phi_1)}{\sin(\phi)} \cos(\phi) =& A_1 + A_2 \cos(\phi_1) \\ \Rightarrow \tan(\phi) =& \frac{A_2 \sin(\phi_1)}{A_1 + A_2 \cos(\phi_1)}. \end{aligned} \tag{16}$$

Further, by squaring and adding the Equations 13 and 14, it is possible to determine the amplitude A of the resulting sinusoidal wave depending on the amplitudes A_1 and A_2 as well as on the phase shift ϕ_1:

$$\begin{aligned} A^2 \cos^2(\phi) + A^2 \sin^2(\phi) &= (A_1 + A_2 \cos(\phi_1))^2 + A_2^2 \sin^2(\phi_1) \\ \Leftrightarrow A^2 &= A_1^2 + 2A_1 A_2 \cos(\phi_1) + A_2^2 \cos^2(\phi_1) + A_2^2 \sin^2(\phi_1) \\ &= A_1^2 + A_2^2 + 2A_1 A_2 \cos(\phi_1) \qquad (17) \\ \Rightarrow |A| &= \sqrt{A_1^2 + A_2^2 + 2A_1 A_2 \cos(\phi_1)} \qquad (18) \end{aligned}$$

A.5 Parameters maps of LAP and PM

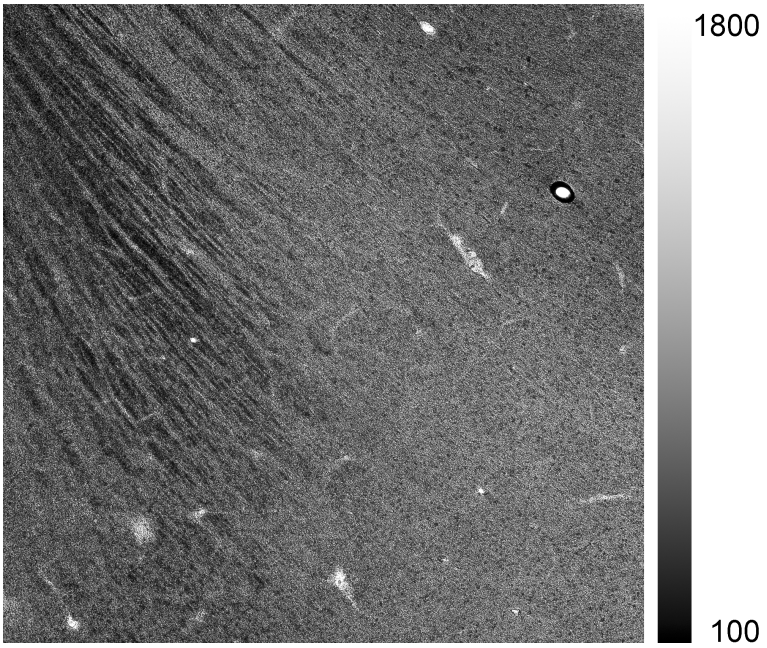

Figure 2: Transmittance image of tile containing fiber tracts of a coronar section obtained with the PM.

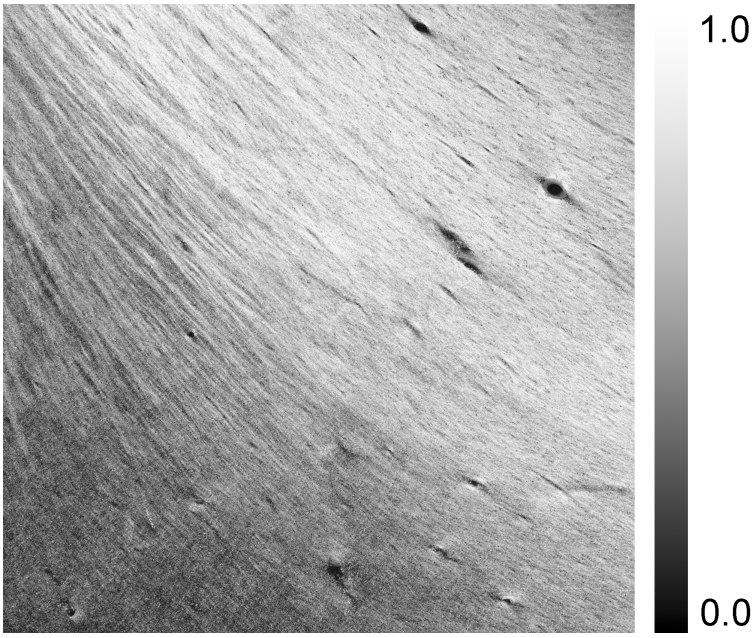

Figure 3: Retardation image of tile containing fiber tracts of a coronar section obtained with the PM.

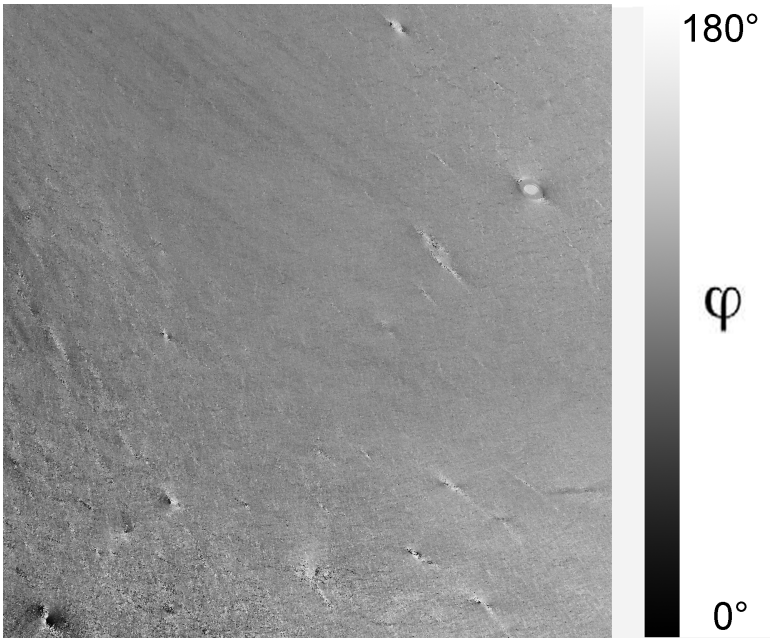

Figure 4: Direction image of tile containing fiber tracts of a coronar section obtained with the PM.

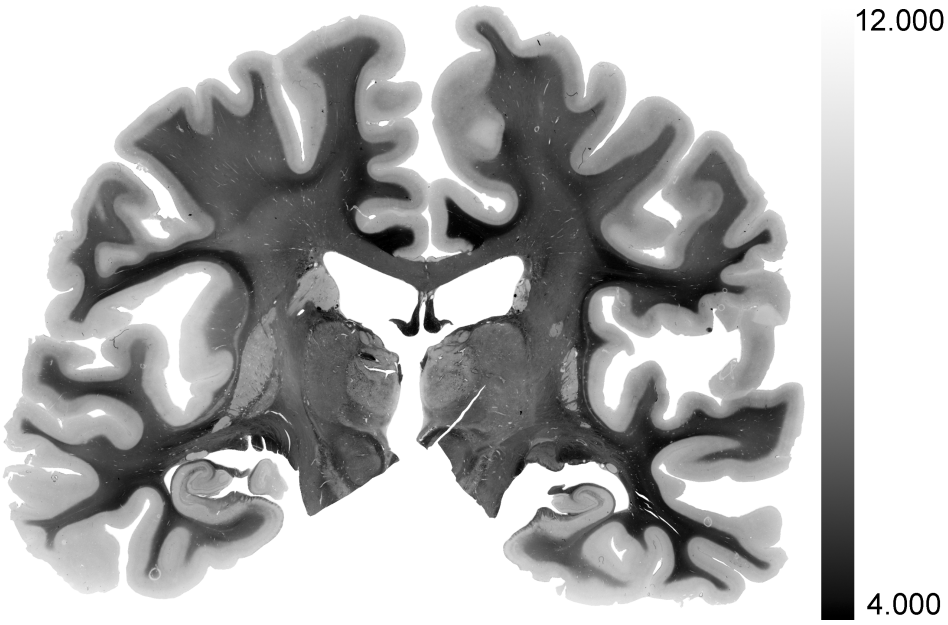

Figure 5: Transmittance image of coronar section obtained with the LAP

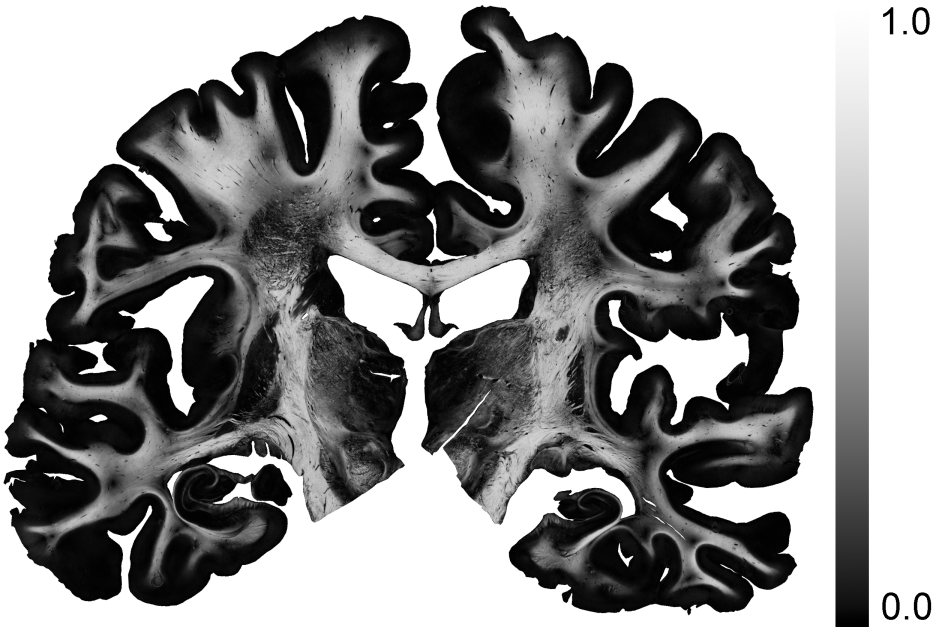

Figure 6: Retardation image of coronar section obtained with the LAP

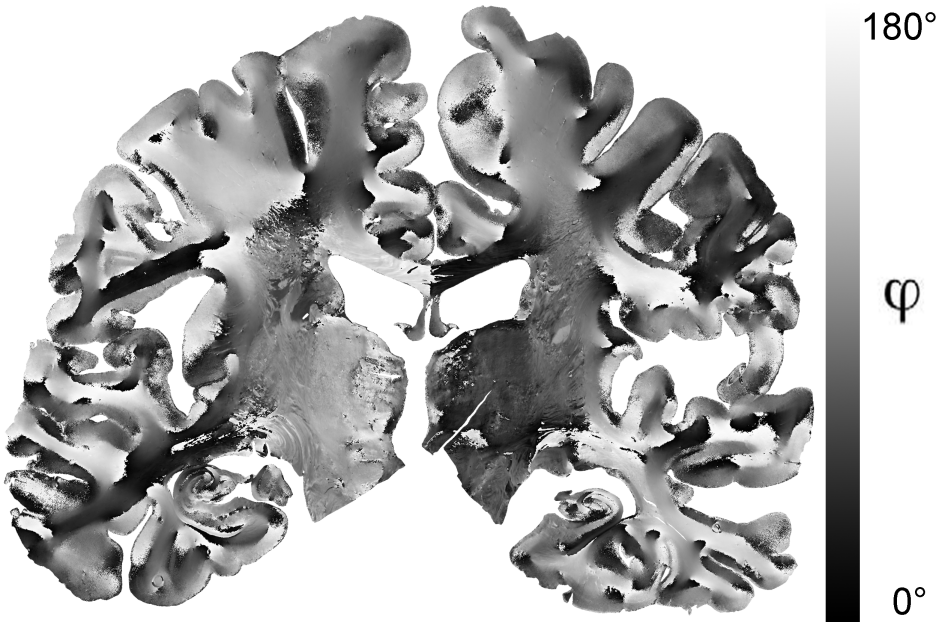

Figure 7: Direction image of coronar section obtained with the LAP

A.6 List of sections of the optic tract

inclination angle	section thickness	number of sections
0°	20 µm	4
0°	30 µm	4
0°	50 µm	4
0°	70 µm	4
0°	100 µm	4
30°	20 µm	4
30°	30 µm	4
30°	50 µm	4
30°	70 µm	2
30°	100 µm	3
60°	20 µm	3
60°	30 µm	2
60°	50 µm	4
60°	70 µm	4
60°	100 µm	4
90°	20 µm	4
90°	30 µm	3
90°	50 µm	3
90°	70 µm	4
90°	100 µm	4

Table 1: List of evaluated sections of the optic tract.

Danksagung

Ich möchte mich an dieser Stelle bei all jenen bedanken, die mich bei der Fertigstellung meiner Dissertation unterstützt haben.

Besonders möchte ich meinen lieben Kollegen bedanken, die mit mir unermüdlich diskutiert haben, mich aufgemuntert haben und meine Zeiten der überstrapazierten Nerven geduldet und überstanden haben. Sie gaben mir mit Ihrem fundierten Fachwissen viele Anregungen für meine wissenschaftliche Arbeit. Ohne Ihr Wissen, ohne Ihre Ideen und Ihre Kritik wäre mein Forschungsprojekt niemals soweit gekommen. Vielen Dank für die schönen Mittags-Kaffee-Pausen!

Bei meinem Gruppenleiter Markus Axer möchte ich mich dafür bedanken, dass er jederzeit für konstruktive Gesprche zur Verfügung gestanden hat. Mit seinen wertvollen Ratschlägen hat er zu dem Gelingen der Arbeit beigetragen.

Ein ganz besonderer Dank geht an meinen wundervollen Mann, der mich stets bestärkt hat, wenn ich an mir gezweifelt habe. Er hat mir die ganze Zeit den Rücken frei gehalten und daher widme ich ihm diese Arbeit.